THESIS

A COMPUTATIONAL EXAMINATION OF CONJUGATE HEAT TRANSFER DURING MICROCHANNEL FLOW BOILING USING FINITE ELEMENT ANALYSIS

Submitted by

Bryan E. Burk

Department of Mechanical Engineering

In partial fulfillment of the requirements

for the Degree of Master of Science

Colorado State University

Fort Collins, Colorado

Fall 2018

Master's Committee:

Advisor: Todd M. Bandhauer

Bret C. Windom
Charles S. Henry

ABSTRACT

A COMPUTATIONAL EXAMINATION OF CONJUGATE HEAT TRANSFER DURING MICROCHANNEL FLOW BOILING USING FINITE ELEMENT ANALYSIS

As technology advances, electronic components continue to produce more heat while at the same time growing smaller and being arranged in ever more compact packages. This has created the need for new thermal management systems able to both dissipate the large heat loads and meet the diminishing size requirements. Microchannel heat exchangers have become an integral part of such advanced cooling systems as they provide an exceedingly large surface area over which heat transfer can occur while maintaining a diminutive size. Current microchannel devices primarily use single-phase flow to dissipate the heat. As heat loads increase, so too must flow rates. Due to associated issues with extremely large pressure drops and high pumping power requirements, the practical capacity of single-phase microchannel coolers has largely been met. One particularly promising avenue forward is to utilize flow boiling with similar microchannel heat exchanger designs.

The very high latent heat of vaporization associated with phase change for many fluids allows for a large amount of heat to be dissipated in flow boiling using a relatively low flow rate as compared to single-phase systems, drastically reducing the issues related to pressure drop. Additionally, two-phase heat transfer is associated with much higher heat transfer coefficients, allowing for smaller heat transfer surface areas (and thus smaller overall devices) and lower driving temperature differences for the same heat removal rates. Microchannel flow boiling studies to date have assumed 1D heat conduction through the heat exchanger material and have developed

correlations to predict average heat transfer coefficients. Unfortunately, with the high heat fluxes expected in the near future, and with heat loads being applied at small, localized hotspots, the 1D assumption is no longer valid. Conjugate heat transfer must be considered, and local heat transfer coefficient correlations are necessary for the design of future thermal management systems.

This thesis describes a first of its kind computational model that uses finite element analysis to analyze the conjugate heat transfer problem, complete with local heat transfer coefficients. This work serves as both proof of concept and an evaluation of the predictive capabilities of five published heat transfer correlations when applied locally to a high heat flux microchannel heat exchanger that has been previously tested.

Modeling results show highly variable local heat flux profiles along the microchannel walls, confirming the need to consider conjugate heat transfer. Significant heat spreading resulted in peak local heat fluxes of roughly 0.5× that of the uniformly applied heat flux with 31.4% - 64.1% of total applied heat dissipated outside the region projected directly above the heater. As determined via local temperature comparisons, the correlation from Agostini and Bontemps provides the best overall agreement with average root mean square temperature differences of 2.6°C, though trends suggest that this difference may increase as heat flux increase further than those values tested here.

ACKNOWLEDGMENTS

Firstly, I would like thank you, the reader, for taking the time to read my thesis. If you continue to the end, you will become part of an exclusive club. Next, I must thank Dr. Todd Bandhauer for his guidance, patience and positive outlook over the last few years. He has helped me to learn not only valuable knowledge about engineering, but about myself as well. And, of course, none of this would have been possible without his vision and financial support. I would also like to thank Lawrence Livermore National Laboratory, the ITS Lab partner in this project, for providing the funding and equipment that made much of this work possible. Specifically, I give thanks to Dr. Jack Kotovsky, who worked tirelessly on our behalf to jump through bureaucratic hurdles and move this project along in a timely manner. His original ideas and the levity he brought to the table were equally as important as his organizational skills in making this project a success.

Thank you to all the members of the ITS Lab. Thank you to Taylor Bevis, Kevin Westhoff and Torben Grumstrup for showing me the ropes when I first arrived. Torben, I never could have done this without your hundreds of hours of sacrifice at the hands of the COMSOL demon. Thank you, Matthew Todd, Jensen Hoke, and David Hobby for helping me troubleshoot and figure out how to get things working in the lab. Your help and moral support throughout the years has been invaluable. Thank you to all the other members of the lab during my time here as well. I worked closer with some of you than others, but the human interactions with all of you were the only thing that kept me moving forward at times.

Lastly, I would like to thank my family. I most certainly could not have done this without their love and support. I love you and appreciate all that you have done, and all that you continue to do for me. And, perhaps somewhat childishly, I'm so very grateful for my dogs: Wilbur, Maria,

Zoe, Ziggy, Abby, Olivia, Leonard and Charlie. I've lost a few and gained during my time here, but they have been a constant source of happiness and positivity that makes everything a little easier.

TABLE OF CONTENTS

LIST OF TABLES

LIST OF FIGURES

LIST OF SYMBOLS

Symbol	Description	Units	Dimensionless Number Expression
A	Area	[m^2]	-
Bo	Bond number	-	$\frac{g(\rho_l - \rho_v)D_h^2}{\sigma}$
Bl	Boiling number	-	$\frac{q''}{Gh_{fg}}$
Co	Confinement number	-	$\frac{1}{D_h}\sqrt{\frac{\sigma}{g(\rho_l - \rho_v)}}$
C_p	Specific heat	[kJ kg^{-1}]	-
D	Diameter	[m]	-
D_h	Hydraulic Diameter	[m]	-
E	Power	[W]	-
f	Friction factor	-	-
F_S	Empirically obtained friction factor	-	-
G	Mass flux	[kg m^{-2} s^{-1}]	-
H	Height	[m]	-
h	Heat transfer coefficient	[W m^{-2} K^{-1}]	-
i	Enthalpy	[kJ kg^{-1}]	-
i_{fg}	Enthalpy of vaporization	[kJ kg^{-1}]	-
k	Thermal conductivity	[W m^{-1} K^{-1}]	-
K_{min}	Minor loss coefficient	-	-
L	Length	[m]	-
L_c	Characteristic length	[m]	-

$\dot{m}$	Mass flow rate	[kg s^{-1}]	-
M	Molecular mass of fluid	[kg $kmol^{-1}$]	-
Nu	Nusselt number	-	$\frac{hL}{k}$
P	Pressure	[kPa]	-
P_F	Wetted perimeter	[m]	-
P_H	Heated perimeter	[m]	-
P_R	Reduced pressure	-	-
Pr	Prandtl	-	-
$\dot{Q}$	Heat transfer rate	[W s^{-1}]	-
q''	Heat flux	[W m^{-2}]	-
R_P	Surface roughness parameter	[µm]	-
R	Thermal resistance	[K W^{-1}]	-
Re	Reynolds number	-	$\frac{\rho u D_h}{\mu}$
t	Thickness	[µm]	-
u	Velocity	[m s^{-1}]	-
W	Width	[m]	-
We	Weber number	-	$\frac{\rho u^2 L_c}{\sigma}$
x	Vapor quality	-	-
$X_{vv/tt}$	Lockhart and Martinelli parameter	-	
Greek Symbols			
α	Void fraction	-	-
α_o	Zivi void fraction	-	$\left[1+\left(\frac{1-x}{x}\right)\left(\frac{\rho_l}{\rho_v}\right)^{2/3}\right]$
β	Aspect Ratio	-	$\frac{W}{H}$

Δ	Difference	-	-
δ_c	Capillary constant	-	$\sqrt{\frac{2\sigma}{g(\rho_l - \rho_v)}}$
ε	Surface roughness	-	-
η	Efficiency	-	-
μ	Dynamic viscosity	[kg m^{-1} s^{-1}]	-
ρ	Density	[kg m^{-3}]	-
σ	Surface tension	[N m^{-1}]	-
Subscripts			
a	Accelerational	-	-
c	Characteristic	-	-
cb	Convective boiling	-	-
ch	Channel	-	-
conv	Convection	-	-
db	Dittus-Boelter	-	-
down	Downstream	-	-
f	Frictional	-	-
fd	Fully developed	-	-
g	Gravitational	-	-
i	Index number	-	-
in	Inlet	-	-
j	Index number	-	-
l	Liquid	-	-
min	Minor	-	-
nb	Nucleate boiling	-	-

ori	Orifice	-	-
RMS	Root mean square	-	-
sp	Single-phase	-	-
th	Thermal	-	-
tot	Total	-	-
tp	Two-phase	-	-
up	Upstream	-	-
v	Vapor	-	-

Chapter 1: Introduction

1.1 Background and Motivation

Recent decades have witnessed dramatic increases in the heat dissipation requirements of contemporary technologies. The miniaturization and simultaneous performance increases of electronic components have led to ever-growing volumetric heat dissipation requirements and thus the need for ever more compact and effective thermal management systems. Based on predictions from the International Technology Roadmap of Semiconductors in 2011, assuming today's average chip die sizes, we can predict average heat fluxes of up to 450 W cm^{-2} for microprocessor chips by the year 2026 and peak heat fluxes of up to 4.5 kW cm^{-2} [1]. Modern laser diodes can yield heat fluxes in excess of 1 kW cm^{-2} and more concentrated lasers are desirable for various applications, but the inability to dissipate the accompanying increased heat loads prevents the fabrication of densely packed arrays. In order for technological progress to continue in these areas, new thermal management strategies must be investigated.

Forced convection in microchannels has provided promising solutions to these increasing thermal demands since initial work began in the early 1980s. Tuckerman and Pease [2] first demonstrated single-phase microchannel cooling using water in 1981 and were able to dissipate heat fluxes up to 790 W cm^{-2}. Unfortunately, single-phase cooling requires very high flow rates and thus produces very high pressure drops, necessitating high pumping powers. This also necessitates large fluid inventories which do not lend themselves to compact thermal management systems. Despite this, work with single-phase forced convection continues. Recent research is focused on unique geometries and nanofluids [3], but it appears the practical limits of single-phase microchannel cooling have largely been met. For this reason, research on alternative cooling strategies has increased in the last decade.

Microchannel flow boiling, spray cooling and jet impingement have all received much attention in recent years. Bevis and Bandhauer [4] have demonstrated dissipation of heat fluxes up to 1.1 kW cm^{-2} with flow boiling in an array of parallel microchannels. Spray cooling and jet impingement have shown the ability to handle higher heat fluxes (1.2 kW cm^{-2} [5] and 1.8 kW cm^{-2} [6] respectively) but the complexities of creating robust and durable systems with large heat transfer areas are major obstacles to reliable implementation. Microchannel flow boiling heat exchangers, on the other hand, can be easily arrayed into robust compact systems. The additional benefits of relatively low pumping power and small fluid inventory requirements make microchannel flow boiling one of the most promising thermal management strategies going forward. Many studies of flow boiling have been performed and much has been learned, but it is necessary to begin applying the knowledge gained to real world situations.

The vast majority of flow boiling experiments have been performed with uniform applied heat flux along the length of the channel. This has allowed for the reasonable assumption of 1D heat conduction through the heat sink material during analysis of the results. This allows researchers to assume a channel wall heat flux equal to that of the applied flux and to calculate channel wall temperatures. Once these values are known the calculation of wall heat transfer coefficient is a somewhat trivial matter. To the author's knowledge, all published heat transfer coefficient correlations to date have employed this 1D conduction simplification. In real world applications, however, heat flux is rarely uniform. Local hot spots result in heat spreading so the 1D assumption is no longer valid and conjugate heat transfer (the combination of both conduction and convection) must be considered.

Computational modeling can be employed to analyze the conjugate heat problem, but it requires accurate local heat transfer coefficient correlations to do so. Unfortunately, very few local

heat transfer correlations exist for microchannels and currently none are designed for extreme heat fluxes. The current work examines five widely used heat transfer coefficient correlations in conjunction with finite element analysis (FEA) to determine their validity when applied to these extreme heat fluxes and the accompanying small channel geometries. COMSOL Multiphysics is paired with MATLAB to compare correlation predictions to results obtained from previous experiments.

1.2 Experimental and Computational Aims

Local heat transfer coefficients are necessary to successfully characterize and design future microchannel heat sinks that will be necessary to accommodate the ever-growing heat loads in electronics. Heat transfer coefficient correlations designed for this purpose do not exist. Though computational modeling can be used to solve the conjugate heat transfer problem and therefore evaluate the validity of current correlations when applied locally in high heat flux situations, very little work has been done on this front. The goal of the current work is to utilize FEA to evaluate five widely used heat transfer coefficient correlations to accomplish this task. This is accomplished by coupling COMSOL with MATLAB and iteratively solving the local conjugate heat transfer problem.

1.3 Thesis Organization

In the following chapters, the motivation, design and analysis of a comprehensive computational model utilizing FEA to evaluate performance predictions of various locally applied heat transfer coefficient correlations is discussed. Several heat transfer correlations are examined and results are compared with experimental data collected previously [4,7]. The current effort is the first of its kind to utilize FEA to analyze conjugate heat transfer behavior in microchannel flow

boiling at a completely local level, and as such, provides a powerful tool to guide future design of microchannel heat sinks.

Chapter Two presents a literature review of experimental and computational efforts aimed at understanding and characterizing microchannel flow boiling. First, the basics of microchannel forced convection, including micro/macro transition criteria, flow patterns and heat transfer behavior are discussed. Then, relevant studies regarding local hotspots and the need for consideration of conjugate heat transfer are considered, followed by a review of computational research of flow boiling behavior. Chapter Three describes the experimental setup and testing procedure leading to the collection of the data used here for comparison. This includes a detailed description of the test facility and brief synopsis of the experimental results. Chapter Four describes the design and solution method of the computational model. The correlations examined, and all assumptions made will be described therein. Chapter Five discusses the computational results for each heat transfer coefficient correlation and compares these to the experimental data. Chapter Six concludes this thesis by summarizing the conclusions drawn from current work and briefly discussing recommendations for future work.

Chapter 2: Literature Review

The pioneering work with forced convection in microchannels was performed in the early 1980s by Tuckerman and Pease [2]. Though these early results showed promise, little research was done on the subject during the ensuing decade. Beginning in the early 1990s, spurred on by the rapid development of electronics and their incorporation into all aspects of society, research began moving forward at a steady pace until interest in single-phase microchannel cooling exploded in the early 2000s (Figure 2-1a). According to Kandlikar [3], much of the early research was based on validating the continuum theory for incompressible flow in microchannels. Around the time that interest in the field increased (~2003), the focus shifted to gaining a fundamental understanding of flow and heat transfer phenomena present in microchannel liquid flow and then eventually shifted again towards practical applications and heat transfer enhancement. Today, research continues to focus on heat transfer enhancements using unique channel geometries and custom designed fluids.

As electronics packaging has progressed, making components ever more powerful and compact, associated heat duties have also risen and the development of effective thermal management strategies is paramount. For example, modern laser diode arrays can produce heat fluxes in excess of 1 kW/cm^2 and higher density arrays, which would produce greater brightness and therefore higher heat fluxes, are desirable for various medical and defense applications. Likewise, peak microprocessor heat fluxes are expected to reach up to 4.5 kW/cm^2 by the year 2026 [1]. Single-phase forced convection has been shown by Skidmore et al. [8] to be capable of removing up to 1.49 kW/cm^2. A key shortcoming, however, is that it relies on the temperature rise of the working fluid (sensible heat) to remove heat from an object. This limits its usefulness for modern commercial applications.

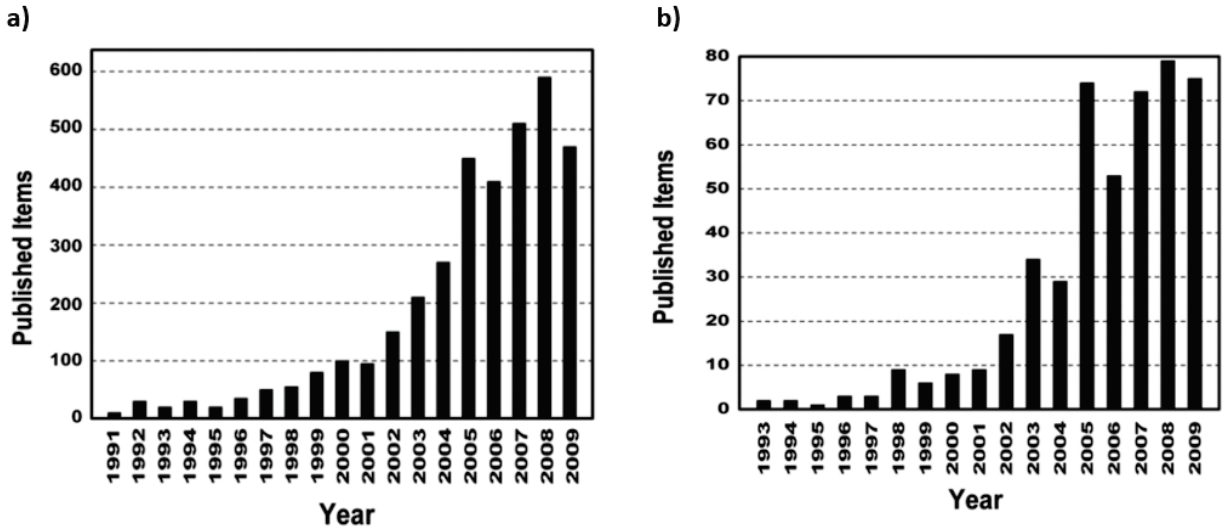

Figure 2-1: Number of publications annually on (a) single-phase microchannel and (b) two-phase microchannel studies between 1991 and 2009 [3].

Many electronic components must be kept below a specific temperature to operate efficiently and prevent damage, which limits the allowable amount of temperature rise that can occur. For example, the typical temperature limit for a microprocessor chip is 85°C [1,9]. A single-phase fluid entering a heat exchanger at 20°C will therefore have a maximum potential temperature rise of 65°C. Furthermore, as the fluid temperature rises along the length of the flow path, the driving temperature difference between the fluid and component junction decreases, resulting in a dramatic decrease in heat transfer rate. As a result, the practical fluid temperature rise limit is lowered. Additionally, large temperature rises can lead to undesirable thermal gradients within the component being cooled. In laser diode arrays, this can change the wavelength of emitted light from each individual diode. The only way to mitigate this temperature rise for a given fluid is to increase the mass flow rate. Large flow rates combined with small hydraulic diameters (D_h < 3.0 mm) result in large pressure losses and requirements for high pumping powers [2]. Though single-phase research continues around the use of nanofluids and the design of complex channel geometries, the practical limits of single-phase forced convection have largely been met [4]. For these reasons, recent research has focused on two-phase cooling and microchannel flow boiling.

The following sections provide an overview of microchannel flow boiling research and of the aims of the current work. First, a review of microchannel flow boiling basics, including flow dynamics and heat transfer, is presented. This is followed by a review of relevant computational studies which model various aspects of two-phase microchannel behavior, and finally by a brief summary and an examination of the objectives of current work.

2.1 Microchannel Flow Boiling

Few studies on microchannel flow boiling were carried out in the 1990s. Beginning in the early 2000s, however, the number of studies published annually began to rise dramatically (Figure 2-1b) [3]. A major advantage of flow boiling over single-phase convection is that flow boiling does not rely on a temperature rise to reject heat. Because two-phase heat transfer utilizes the latent heat of vaporization of the working fluid, heat exchangers can operate with lower flow rates and decreased pumping powers compared to single-phase forced convection. For example, R134a has a nominal latent heat of vaporization of 182 kJ kg^{-1} and a nominal liquid specific heat of 0.99 kJ kg^{-1} K^{-1}. If the temperature rise is limited to 25°C, a single-phase liquid system would require a flow rate of approximately 7× that of a two-phase system to reject the same amount of heat. Admittedly this is a very simplified analysis, but similar results have been documented thoroughly in literature [9–12]. Lower flow rates also result in a smaller necessary fluid inventory, which allows for smaller overall smaller thermal management systems [13–15]. Additionally, since two-phase cooling systems experience no theoretical temperature rise, large (undesirable) temperature gradients do not exist within the electronic component (in actuality a few degrees of subcooling is frequently present to ensure a single-phase fluid entering the channels but thermal gradients are still minimal) [9,12–16]. The dramatically lower flow rates associated with two-phase cooling also result in much lower pumping power requirements, which from an energy standpoint is desirable.

Data centers use roughly 1.3% of the total electricity consumed globally and the average data center expends approximately 33% of its total electricity usage on thermal management [17,18]. This results in enormous financial and environmental costs. It is estimated that by the year 2020 data centers in the US alone will have electricity costs that rise to $13 billion per year and will result in roughly 150 million metric tons of carbon [19]. The ability to decrease this power consumption is a very attractive factor when considering microchannel flow boiling. An additional benefit of two-phase microchannel cooling is that heat transfer coefficients are much greater than those for single-phase [20–22]. This results in smaller necessary driving temperature differences which, in turn, allow for higher working fluid temperatures. As heat removal becomes easier at higher temperatures, this could result in greater energy savings from secondary coolant systems designed to remove heat from the primary working fluid.

The rest of this section is organized according to different aspects of microchannel flow boiling. It begins with an examination of the criteria defining the micro-regime and continues to discuss flow patterns, heat transfer, pressure drop, issues, and critical needs for further research. After these are discussed, a summary of computational studies is then given.

2.1.1 Micro to Conventional Scale Transition Criteria

Two-phase heat transfer and flow dynamics in microchannels behave differently than in their macro sized counter parts. In general, flow regime maps, pressure drop and heat transfer correlations designed for conventionally sized channels do not accurately predict behavior in the micro regime [23]. These differences arise for several reasons, but one of the most important is that as channel dimensions—and thus cross-sectional area of the fluid flow path—become smaller, the relative importance of the fundamental forces (surface tension, gravity, viscosity and inertia) change [22]. Surface tension, which can largely be ignored in conventional channels, becomes a

driving force, while gravity becomes less important, in smaller channels. This effect can be understood by envisioning a capillary tube. At some small tube diameter, surface tension and adhesive forces between the fluid and tube wall overcome gravitational force and lift fluid molecules to some height. Mishima and Hibiki [24] examined air/water flow through vertically oriented capillary tubes (1.05 mm < D_h < 4.08 mm) that were joined into closed loops and found that these same capillary forces affected the bubble dynamics and the flow regime of the air/water mixture. Triplett et al. [25] examined air/water flow through horizontally oriented, circular and triangular microchannels (1.09 mm < D_h < 1.49 mm) and also found that capillary forces had a large effect on bubble shape. The effects of viscous and inertial forces will be discussed in the next section on flow patterns. A second important reason that microchannels differ from conventional channels is related to evaporation [22]. At some point, channels are small enough that the vapor bubbles formed during boiling are constrained in size and shape, which affects flow dynamics, heat transfer and pressure drop characteristics.

Although it is well known that microchannels behave differently than conventional channels, there is little agreement on where the macro scale ends and the micro scale begins. Kew and Cornwell [26] found that conventional correlations worked well for tubes with diameters of 2.89 mm and 3.39 mm but that predictive accuracy began to suffer for smaller channels. It can be safely surmised that microscale behavior does not begin immediately at one particular threshold size. Kandlikar and Grande [27] have proposed three size ranges based on hydraulic diameter with conventional channels having diameters larger than 3.0 mm, micro channels having diameters smaller than 0.2 mm and the intermediate range of diameters constituting minichannels. Mehendale et al. [28] take classification a step further and distinguish between macro, compact, meso and micro scales. Macro scale consists of hydraulic diameters larger than 6.0 mm, compact

scale of hydraulic diameters between 1 mm and 6 mm, meso scale of hydraulic diameters between 100 μm and 1 mm and micro scale of everything below 100 μm.

Some researchers have proposed criteria related to various dimensionless parameters. Because both the relative interaction of forces and bubble confinement, which depends on size, play a determining factor in microchannel behavior, Kew and Cornwell [26] introduced the confinement number (*Co*), relating surface tension (σ), gravity (*g*) and hydraulic diameter (D_h):

$$Co = \frac{1}{D_h}\sqrt{\frac{\sigma}{g\left(\rho_l - \rho_v\right)}} \tag{2.1}$$

Based on an analysis of data from various sources [14,29–32], they suggest that the micro regime begins when the confinement number is larger than 0.5. Kuznetsov and Shamirzaev [33] suggest a similar criteria in which the micro regime begins when the width of the channel shrinks below the capillary constant (δ_c):

$$\delta_c = \sqrt{\frac{2\sigma}{g\left(\rho_l - \rho_v\right)}} \tag{2.2}$$

Cheng et al. [34] base the three regimes of micro, mini and macro on the Bond number (*Bo*), which also relates surface tension, gravity and hydraulic diameter:

$$Bo = \frac{g\left(\rho_l - \rho_v\right)D_h^2}{\sigma} \tag{2.3}$$

They proposed that microchannels have Bond numbers less than 0.05 and that gravitational effects can be ignored in this region. Minichannels have Bond numbers between 0.05 and 3.0 and constitute a region in which surface tension is dominant and gravitational effects are still present, but small. Macrochannels have Bond numbers greater than 3.0 and constitute a region in which gravity is much more important than surface tension.

Garimella and Harirchian [35–37] found that flow confinement is dependent on both channel size and mass flux. Their results are shown in Figure 2-2a. They proposed the convective

confinement number, a combination of the Bond number and the Reynolds number, and found this to be an accurate method for defining flow confinement. This parameter is defined as

$$Bo^{0.5} \times Re = \frac{1}{\mu_l}\left(\frac{g\left(\rho_l - \rho_v\right)}{\sigma}\right)^{0.5} GL_c^{\ 2} \tag{2.4}$$

where μ is the viscosity, G is the mass flux and L_c, the characteristic length, is the square root of the cross-sectional area of the channel as opposed to the usual hydraulic diameter. They found that vapor confinement is present when the convective confinement number is less than 160 and absent when larger than 160. Since confinement is a hallmark of microchannel flow, this can be considered the determining criteria between micro and macro. The authors compared this transition criteria with experimental data from many other studies using different fluids and found it to predict confinement well (see Figure 2-2b). The authors stress that it is the cross-sectional area, rather than the hydraulic diameter or aspect ratio, that is important in this determination. Though there exists no clear consensus on what divides a microchannel from a conventional channel, it is clear that significant differences exist between the two sizes. The current work lies firmly within

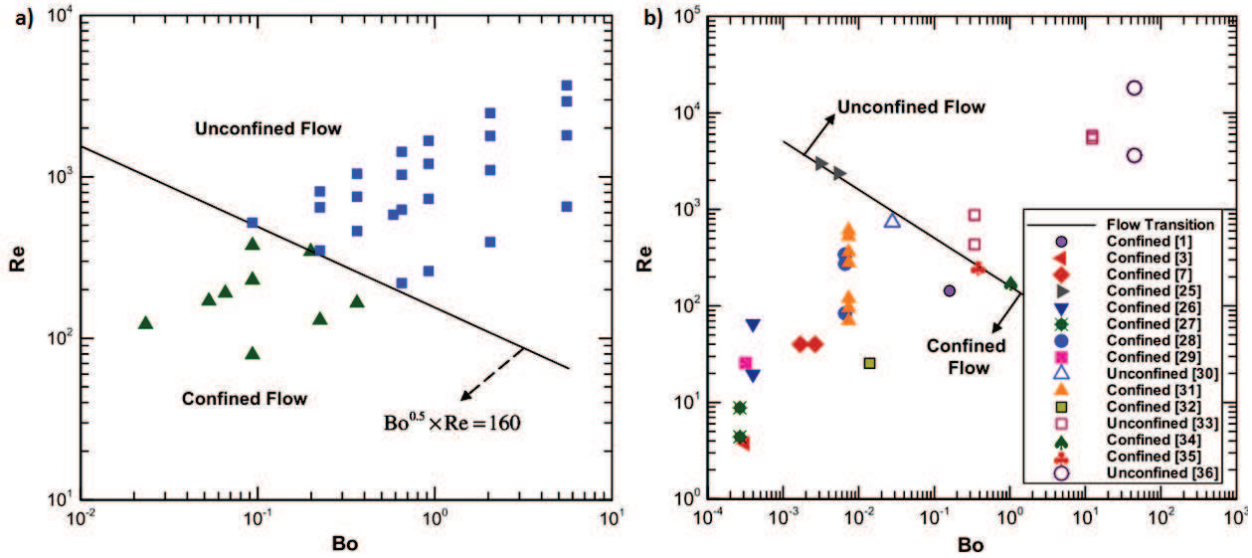

Figure 2-2: Transition from confined to unconfined flow from (a) Garimella and Harirchian and (b) various other studies [35]. A convection confinement number value of 160 divides the two regions.

the micro-regime according to all of the above criteria, so I will set aside the issue of exact classification in the next section and discuss the flow patterns associated with microchannel flow boiling.

2.1.2 Flow Patterns

The flow regimes seen in microchannels are, for the most part, the same as those seen in macrochannels. The major exception is the absence of stratified flow due to the negligible impact of gravity at the microscale. Flow regime has significant effects on pressure drop and heat transfer characteristics, so accurately identifying flow regime is of critical importance. Correlations based on macroscale flow pattern maps offer decent predictions in some microchannel conditions but are inaccurate in others, with the greatest errors tending to be near regions of flow regime transitions. This suggests that macroscale flow maps do not accurately predict microscale flow transitions. For this reason, several investigators have begun designing flow regime maps specific to microchannels [38]. The main flow regimes in microchannels are shown in .

Typically, fluid enters the heated channel as a slightly subcooled liquid. As heat is absorbed from the surrounding channel walls, the fluid temperature rises until the saturation point is reached and tiny vapor bubbles begin nucleating along the channel wall. This signals the onset of nucleate boiling (ONB). The bubbles continue to grow until they become large enough to be detached from

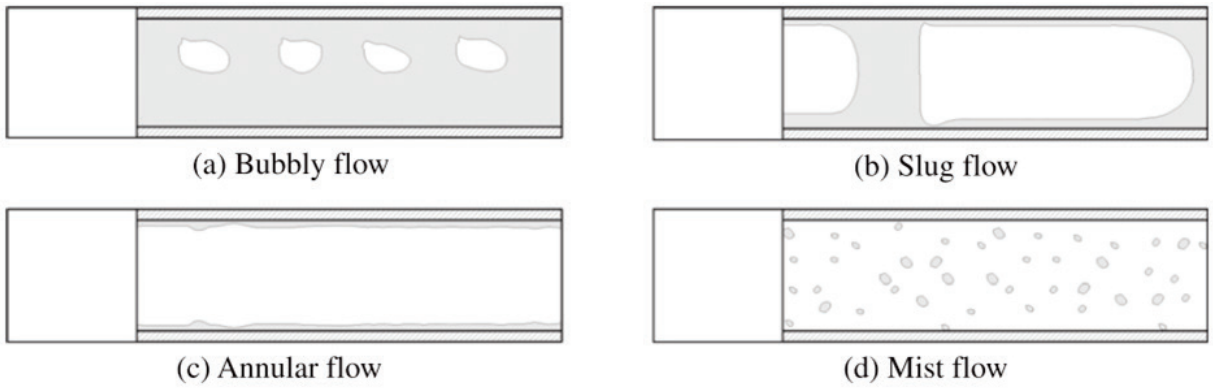

Figure 2-3: Flow regimes present in microchannels: (a) bubbly flow, (b) slug flow, (c) annular flow, (d) mist flow [38].

the channel wall by viscous forces and are swept along with the fluid as a train of discrete vapor bubbles. This constitutes bubbly flow. With continued heat addition, the number and size of vapor bubbles present in the bulk fluid flow increases and individual bubbles begin to coalesce to form larger bubbles. The diameter of these bubbles is eventually constrained by the size of the channel and oblong vapor pockets form, constituting slug or intermittent flow. These vapor pockets continue to grow due to evaporation at the liquid/vapor interface. Annular flow is achieved when these pockets eventually merge together to create a continuous vapor core surrounded by a thin film of liquid. During annular flow, the liquid film grows thinner as continuing evaporation causes the vapor core to grow. If sufficient heat is absorbed, the film can grow thin enough that interfacial shear forces between the vapor core and liquid film begin to dislodge small liquid droplets from the film which then become trapped in the vapor core and are carried downstream in mist flow. If the liquid film completely disappears and vapor blankets the wall of the channel, dryout occurs. Dryout may be considered a fifth flow regime if so desired, but mist flow will continue through this region. Several other transition regions—such as churn flow, a semi-annular and highly chaotic flow—and sub regimes—such as wavy annular and smooth annular—exist, but a comprehensive knowledge of these regions is not necessary to gain a basic understanding of flow boiling characteristics.

Several researchers have attempted to create new flow regime maps [25,39–42]. One particularly promising effort from Harirchian and Garimella [35,43] attempts to create a comprehensive map that takes into account all relevant fluid and channel properties. The map was designed based on 390 data points using FC-77 as the working fluid and having channel cross-sectional area, mass flux and heat flux ranges of 0.009 mm^2 to 2.201 mm^2, 225 kg m^2 s^{-1} to 1420 kg m^2 s^{-1} and 25 kW m^{-2} to 380 kW m^{-2}, respectively. This map, shown in Figure 2-4a, neatly

divides the different flow regimes for both conventional and microscale channels using the confinement number, defined earlier in Equation (2.4), which takes into account channel cross-sectional area as well as several fluid properties, along with the boiling number (*Bl*), which takes into account heat flux (q''), mass flux and the fluid enthalpy of vaporization (i_{fg}):

$$Bl = \frac{q''}{Gi_{fg}} \tag{2.5}$$

The first major division occurs at a confinement number value of 160, as discussed in the previous section, which separates confined and unconfined flow. The second is a line defined by $Bl = 0.017(Bo^{0.4} \times Re^{-0.3})$ when the term $Bo \times Re$ is plotted against the confinement number. These flow transition predictions also agree well with data from various other studies in literature that use water and other fluorocarbon fluids (see Figure 2-4b). While these results are promising, the authors are careful to point out that limited flow visualization data is available and therefore there is limited data to compare the criteria against. More research is needed before a truly comprehensive map can be validated.

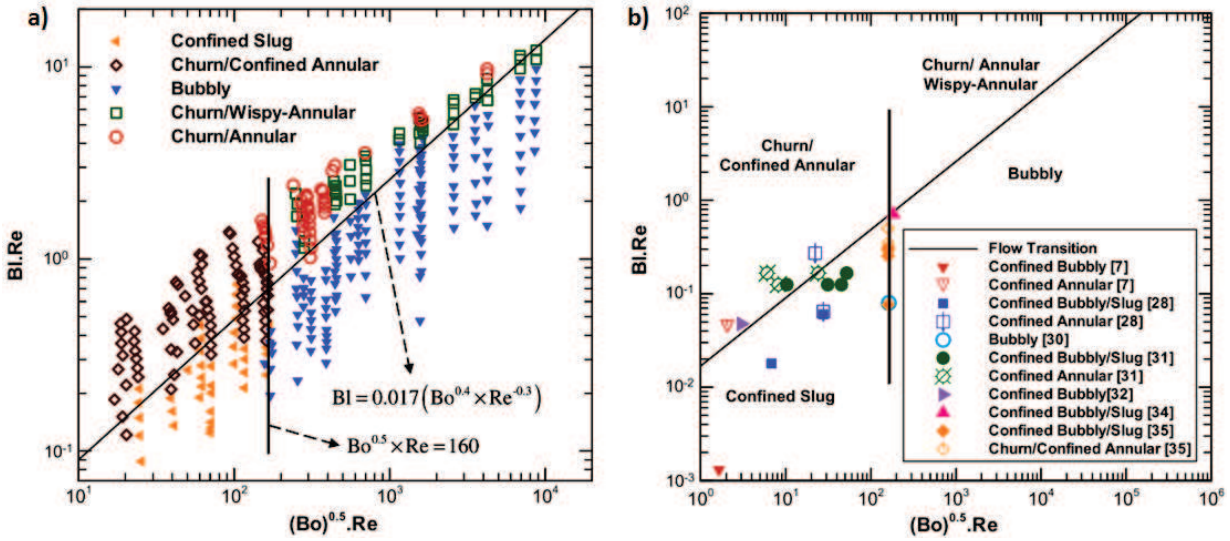

Figure 2-4: Comprehensive flow regime map from Harichian and Garimella [43] compared to data from (a) their own studies and (b) several other studies.

2.1.3 Heat Transfer

The two main heat transfer mechanisms in flow boiling are nucleate boiling and convective boiling. Nucleate boiling is the formation and growth of vapor bubbles attached to the superheated channel wall, while convective boiling occurs as heat is transferred through the liquid to the liquid/vapor interface where evaporation takes place. In general, nucleate boiling is characterized by heat transfer coefficients that are strongly dependent on heat flux and relatively independent of mass flux and vapor quality. Nucleate boiling dominates heat transfer in the bubbly to slug flow regimes. Convective boiling has the opposite heat transfer coefficient dependencies and tends to occur in the slug-mist flow regimes.

Numerous studies have found micro channel flow boiling to be dominated by nucleate boiling [46,47,56–59,48–55], convective boiling [60–63] or some combination of the two [64–71]. Kim and Mudawar [44,45] provide the schematic shown in Figure 2-5 depicting the typical flow regimes and length scales associated with both nucleate and convective boiling dominated

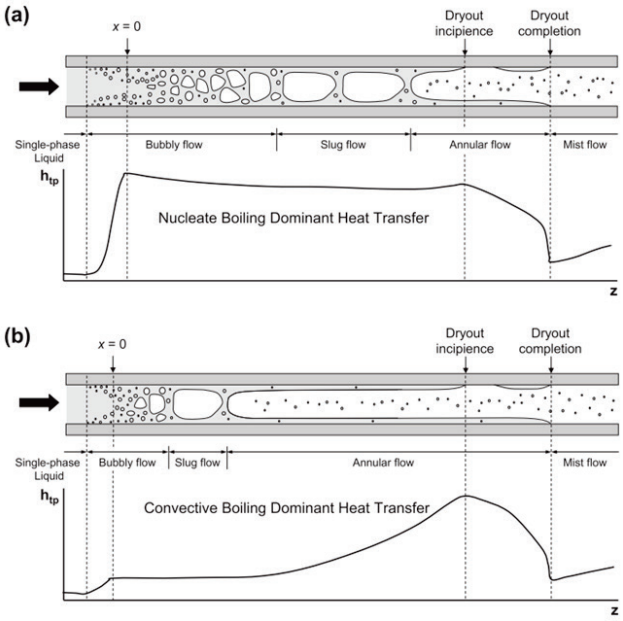

Figure 2-5: Relative two-phase heat transfer coefficient and flow regime schematic for (a) nucleate boiling and (b) convective boiling dominated flows [44,45].

uniformly heated microchannels. The two-phase heat transfer coefficient associated with nucleate boiling decreases slightly along the length of the channel as bubbly flow gives way to slug flow and eventually to annular flow. When convective boiling dominates, the heat transfer coefficient begins to increase as annular flow begins and the liquid film along the channel wall thins. As is expected, nucleate boiling dominated flows consist of extended regions of bubbly and slug flow and convective boiling dominated flows consist of extended regions of annular flow. One additional trait to note from the figure is that the heat transfer coefficient plummets once dryout begins (dryout incipience) for both nucleate and convective boiling heat transfer. It is clear from these data that the relative importance of both heat transfer mechanisms depends on flow regime, but as described in the previous section there is no clear comprehensive flow regime map for microchannel flow boiling.

The development of heat transfer coefficient correlations to predict heat transfer behavior has been a topic of much research [14,22,29,62,72–75], but most efforts to date have been met with limited success. Published data characterizing microchannel flow boiling heat transfer are often contradictory. For example, in experiments with R113 in 3.15 mm diameter stainless steel tubes, Lazarek and Black [29] found that heat transfer coefficient was dependent on heat flux and independent of mass flux and vapor quality. Owhaib et al. [76] found the same thing in experiments with R134a in stainless steel tubes with diameters ranging from 0.826 mm to 1.7 mm. On the other hand, Kuznetsov and Shamirzaev [33] used both R134a and R21 in stainless steel microchannels (D_h = 0.975 mm) and found that heat transfer coefficient was relatively independent of heat flux, and Sumith et al. [60] determined that heat transfer coefficient for water in 1.45 mm diameter stainless steel tubes was dependent on both mass flux and vapor quality. Many other authors have found similar conflicting patterns in various experiments, as well as other dependencies on

different fluid properties and different aspects of channel geometry. Much of the discrepancy can be attributed to the fact that most microchannel flow boiling experiments are performed using small sample sizes and, as discussed in section 2.1.1, a lack of consensus on what constitutes the micro regime. As a result, most conclusions prove valid only over a narrow range of parameters. Several recent attempts have been made to create more comprehensive correlations valid over larger ranges [21,45], but even these have been developed based on the unrealistic assumption of uniform heat flux and thus predict only average heat transfer coefficients. Furthermore, two-phase heat transfer is critically dependent on the saturation temperature of the coolant which itself is directly related to the fluid saturation pressure. As discussed in the next section, determination of the local fluid pressure is non-trivial.

2.1.4 Pressure Drop

Much like heat transfer, pressure drop in microchannel flow boiling is complex and poorly understood. Total two-phase pressure drop (ΔP_{tp}) consists of three major components: frictional losses (ΔP_f), accelerational losses (ΔP_a) and gravitational losses (ΔP_g) [77]:

$$\Delta P_{tp} = \Delta P_f + \Delta P_a + \Delta P_g \tag{2.6}$$

Due to the decreased importance of gravity in microscale flows, the gravitational component is typically very small. In horizontally oriented channels this component is absent and so will be ignored here. The accelerational pressure gradient can be given as

$$\left(\frac{dP}{dz}\right)_a = G^2 \frac{d}{dx}\left[\frac{x^2}{\alpha\rho_v} + \frac{(1-x)^2}{(1-\alpha)\rho_l}\right] \tag{2.7}$$

where α is the void fraction of the two-phase mixture, x is the vapor quality and the positive z-axis is the flow direction. The accelerational pressure drop is then obtained through integration of the gradient term. The void fraction can be determined in several ways, two of which are given in

Equation (2.8), Zivi's relation [78], and Equation (2.9), which is based on the Homogeneous Equilibrium model (HEM) [79–83].

$$\alpha = \left[1 + \left(\frac{1-x}{x}\right)\left(\frac{\rho_v}{\rho_l}\right)^{2/3}\right]^{-1} \tag{2.8}$$

$$\alpha = \left[1 + \left(\frac{1-x}{x}\right)\left(\frac{\rho_v}{\rho_l}\right)\right]^{-1} \tag{2.9}$$

The frictional pressure drop component can likewise be obtained from the HEM or from other published semi-empirical correlations [22,24,64,73,84–87], the majority of which are based on the separated flow model of Lockhart and Martinelli [88]. As with heat transfer correlations, flow boiling pressure drop correlations are only valid over a narrow range of conditions. This is because most correlations have been developed based on a small subset of data. Attempts have recently been made to create more comprehensive pressure drop correlations based on large consolidated databases [89], however more experimental data is necessary to cover future operational size and mass flux ranges.

2.1.5 Issues: Flow Instabilities and Critical Heat Flux

Microchannel flow boiling heat exchanger design is faced with a number challenges relating to the removal of high heat fluxes. Flow instabilities are common in two-phase systems [90–92] and these problems are exacerbated in microchannels. As fluid in the liquid phase is converted to the vapor phase, fluid properties can change dramatically and result in several types of flow instabilities due to compressibility and flashing [93,94]. The most critical type of flow instability is flow and pressure drop oscillation. A second type that has been found in arrays of parallel microchannels, aptly termed the parallel channel instability, is much less severe. These flow instabilities can be closely related to another issue facing microchannel flow boiling, namely critical heat flux (CHF) and premature dryout.

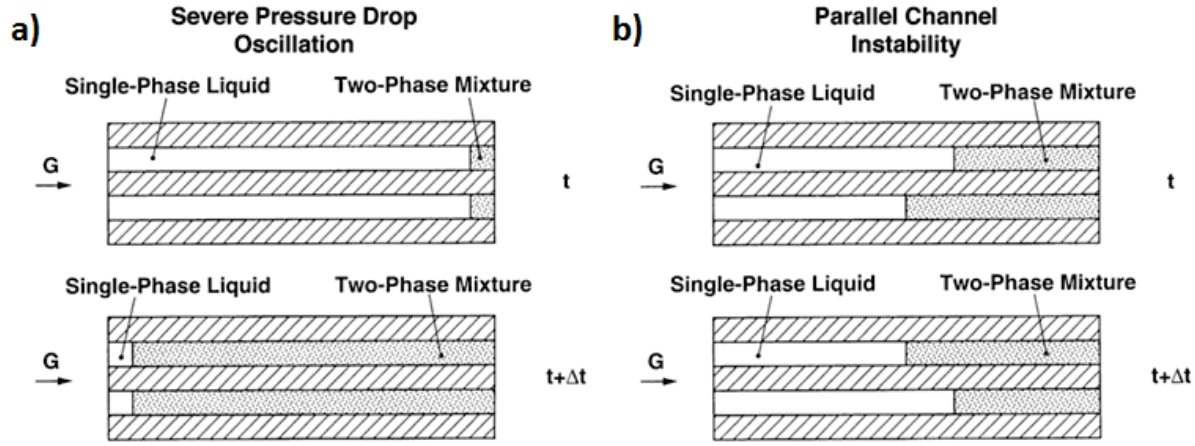

Figure 2-6: Common flow instabilities in microchannel flow boiling: (a) severe pressure drop and flow oscillation due to compressibility and explosive boiling and (b) mild parallel channel instability due to density waves in adjacent channels.

Pressure oscillation has been linked to the phenomenon of explosive boiling in microchannels [93–96]. A significant amount of wall superheat can be required to initiate bubble nucleation in microchannels resulting in rapid bubble growth once nucleation occurs. Because bubble diameter is constrained in microchannels, bubbles will expand both upstream and downstream, pushing liquid along with them. The upstream expansion can cause a temporary flow reversal in the channel, reducing the flow rate of cooling fluid through the channel and leading to increased vapor generation. Flow direction is then restored once the upstream pressure increases sufficiently to force the vapor bubble downstream [23,94], but repeated and periodic reversal due to the nucleation and growth of additional bubbles can result in significant flow rate and pressure drop oscillations. This in turn cause oscillations in the transition location from single-phase to two-phase fluid and has a substantial effect on heat transfer characteristics (Figure 2-6a). This can cause premature dryout.

The second type of instability, parallel channel instability, is due to density wave oscillations within individual channels and the communication of adjacent channels with one another. This results in small, random fluctuations in the spatial location of transition from single-

phase to two-phase fluid within each channel (Figure 2-6b). Due to the small nature of these fluctuations there is typically no noticeable effect on overall heat transfer performance [93].

CHF is a term borrowed from nucleate pool boiling to denote the point at which the two-phase heat transfer coefficient drops dramatically due to the liquid along the hot surface being replaced by a thin film of vapor [97]. During normal nucleate boiling, vapor bubbles detach from the heated wall and are replaced by liquid. New bubbles begin to form at the now open nucleation sites and the process repeats. As heat flux increases, a vapor film can form along the heated surface without fresh liquid moving in to displace it. This causes the heat transfer mechanism at this point to shift from two-phase boiling and evaporation to, essentially, a single-phase heating of the vapor layer. Because the thermal conductivity of the vapor phase is so low, the thermal resistance between the heated wall and the remaining liquid increases dramatically when the vapor layer forms. This is characterized by a dramatic increase in channel wall temperatures—and thus device temperatures—so that the same amount of heat may be dissipated by a much lower heat transfer coefficient. These high temperatures can easily damage electronic components. CHF typically occurs at a relatively high critical value of vapor quality [23,44,98], but premature dryout caused by pressure oscillations can produce similar effects [94,99,100], limiting the heat transfer capability of the heat exchanger. Fortunately, the placement of a flow restriction at the inlet of the microchannel has been shown to dramatically reduce and even eliminate these major oscillations [100–102]. Prediction of CHF is important in microchannel design going forward and is therefore a major focus of research.

2.1.6 Critical Needs

As has been mentioned, most available correlations predicting microchannel flow boiling heat transfer coefficients are only valid over relatively narrow ranges of parameters. These

parameters include channel size (hydraulic diameter or cross-sectional area), heat flux and mass flux among others. Bevis et al. [4] have demonstrated flow boiling heat flux removal of up to 1.1 kW cm^{-2} using R134a in parallel microchannels with hydraulic diameter of 73.4 μm, but both the high heat flux and size lie well outside of the ranges of validity for current correlations. Furthermore, due to heat transfer coefficient dependence on fluid properties, data collected on one fluid may be different than data from a second fluid under identical conditions. In addition to the obvious importance of accurate heat transfer coefficient correlations for predicting heat transfer behavior, accurate pressure drop correlations are also critical. Costa-Patry et al. [103] found that a 15% difference in calculated heat transfer coefficient can exist for the same dataset based solely on the pressure drop model employed.

A second, and perhaps more important issue, is that current heat transfer correlations assume 1D conduction of heat through the heat sink and so assume uniform heat flux. These conditions are unlikely to appear in real world applications as heat production is frequently focused in small hotspots. Hamann et al. [104] and Mahajan et al. [105] found hotspots that occupy between 5% and 25% of the total chip area and to produce heat fluxes roughly 10× greater than those in the rest of the chip. It has also been shown that heat transfer coefficient can vary based on the relative location of hotspots and microchannels [106]. With extreme heat fluxes located in isolated hotspots, significant heat spreading can occur and conjugate heat transfer must be considered. Local heat transfer coefficient correlations must be developed to guide future heat sink development. Hot spot research has begun to collect data useful for development of such correlations, but, given the current state of technology, it is very difficult to collect the robust data necessary. Limited real estate at the microscale creates great difficulty in placing sensors to gather local temperature and pressure data. Even if complex fabrication techniques are employed to

precisely place sensors, Szczukiewicz et al. [107] have pointed out that the time scales involved in microchannel flow boiling are frequently much smaller than the response time of thermocouples. Flow visualization is critical for the development of accurate flow regime maps but the small hydraulic diameters, high aspect ratios, and high flow velocities present in microchannel flow boiling make visualization exceedingly difficult. Fortunately, computational modeling provides an alternative route to exploring the fundamental principles of two-phase microchannel heat transfer. It also provides a method to test the validity of existing correlations when applied to conditions outside of those for which they are prescribed. A brief review of some of the recent computational work published in literature is presented next in Section 2.2 followed by the objectives of the current work in Section 2.3.

2.2 Computational Studies

Computational modeling affords a unique opportunity to investigate aspects of microchannel flow boiling that are difficult to study in the physical experiments. Although modeling is necessarily limited by the accuracy of assumptions built into the model, it is valuable in furthering our understanding of relevant phenomena. Models can be used to explore theories and assumptions based on experimental results and the findings can then be used to guide further experimental research. Likewise, the latest experimental results can be used to adjust and update the model assumptions. Used in tandem, computational modeling and experimental studies can be a powerful tool for gaining greater insight into two-phase microchannel flow dynamics and heat transfer.

Most computational studies have used computational fluid dynamics (CFD) modeling employing either level-set (LS) or volume of fluid (VOF) techniques. Detailed explanations of these techniques can be found elsewhere [108,109]. Creating evolving liquid/vapor interface

regions that simultaneously flow down the length of a channel is non-trivial. Due to this complexity, most CFD studies have examined single bubbles and single nucleation sites to learn about bubble evolution, two-phase flow dynamics and heat transfer. Li and Dhir [110] used a LS method to look at bubble growth in fluid flow along a flat wall and were able to obtain reasonable agreements with experimental data regarding bubble growth rates and departure diameters. Mukherjee et al. [111] used an LS method for a single bubble in a square microchannel and were able to capture the behavior of a bubble growing quickly upon nucleation and then subsequently elongating due to bubble constriction. Once elongation begins, the growth rate increases due to large evaporation rates along the increasing liquid/vapor interfacial area. Zhuan et al. [112] used a VOF method to examine bubble growth in a microtube and were able to determine the effects of heat flux, mass flux and saturation temperature on nucleation frequency, bubble growth rates and departure diameters. Magnini et al. [113] used a VOF method and a computationally intensive phase change model with several different cooling fluids to examine heat transfer characteristics of a single bubble traveling down a channel. They found that hydrodynamic disturbances caused the heat transfer coefficient in the liquid flow immediately trailing the bubble to be greater than that for purely single-phase liquid convection. Heat transfer coefficients in the liquid regions surrounding the bubble were greater still, with values in this region increasing as liquid film thickness decreased. Assuming 1D conduction of heat through the liquid layer resulted in an over-prediction of heat transfer coefficients. Though many of these studies obtain reasonable agreement with experimental findings and shed some light on flow and heat transfer behaviors, they are limited to modeling very simple situations. Computational models become increasingly complex when multiple nucleation sites and/or multiple bubble cycles are considered.

Magnini et al. [114] studied the formation and growth of multiple bubbles from a single nucleation site in a square microchannel using a VOF method. They found that the individual bubble size and the thickness of the surrounding liquid film were both affected by the presence of sequential bubbles. Additionally, they found that time averaged heat transfer coefficients were roughly 60% greater for the trailing bubble cycle than for the leading bubble cycle. Zhang et al. [115] used a combined level-set and volume of fluid (CLSVOF) method to examine both single and multiple bubble cycles from a single nucleation site. Single bubble cycles agreed with simulated results from Mukherjee et al. [116]. An investigation of bubble growth rates for multiple bubble cycles showed that even though departure frequencies and radial sizes matched experimental data, discrepancies existed in axial length due to differences in coalescence. They further attempted to model two nucleation sites and found that modeled heat flux needed to be increased ~25% for bubble growth rates to match data from Tibiriçá and Ribatski [117]. They concluded that "thermo-fluidic phenomena of flow boiling with two nucleation sites are more complex than those for a single nucleation site…" If this is the case, it can safely be assumed that adding even more nucleation sites and more bubble cycles will continue to increase the complexity. While CFD work shows promise, it is limited by its extreme computational demands.

Pan et al. [12] point out that while there is usually a tradeoff between accuracy and computational cost, many investigators continue to refine simplifications to alleviate this tradeoff [114,118–124]. Pan et al. found good agreement with previous experimental studies by employing a novel technique using a VOF method with a moving reference frame and a 2D heated microchannel. This work shows great potential, but more comparison and research must be done. Some authors have utilized other computational/numerical techniques in addition to CFD. Knupp et al. [125,126] have used the General Integral Transform Technique (GITT) in a hybrid analytical-

numerical technique to solve the problem of conjugate heat transfer in channel flow. This method also has demonstrated potential, but again, more robust testing is needed. Great strides have certainly been made with computational simulations, but it appears that accurate system level modeling of complex 3D flow boiling situations is still a way off. While research continues on developing appropriate model simplifications, the limiting issue of computational cost can only be alleviated with advancements in hardware technology. Until then, accurate correlations are crucial to predict microchannel heat sink performance. This work shows how computational modeling can also be used as an excellent tool for evaluating and developing heat transfer correlations.

As has been discussed, most flow boiling correlations assume 1D conduction and uniform heat flux. Experiments can be designed such that these assumptions are accurate but in many real-world applications this is not the case. Extremely high heat fluxes centered at localized hotspots lead to heat spreading and very non-uniform heat flux profiles along the channel walls. To analyze these situations, conjugate heat transfer must be considered. It has even been shown that conjugate heat should be considered for some cases of uniformly applied heat fluxes [127,128]. The assumption of 1D conduction becomes ever more inadequate as devices continue to grow smaller and produce ever greater heat loads. To predict heat transfer behavior and design satisfactory thermal management systems requires the development of accurate local heat transfer coefficient correlations. Finite element analysis (FEA) simulations afford a unique opportunity to aid in this development.

One intriguing possibility, and the purpose of this work, is to utilize FEA to test the validity of current average heat transfer coefficients when applied locally to situations with parameter ranges (size, heat flux, mass flux, etc.) for which they were not specifically designed. Though the capability to do this exists, very little work has been done to harness this ability. Indeed, only one

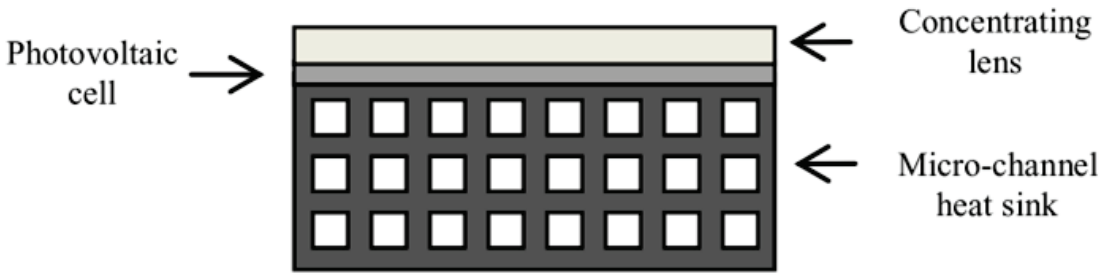

Figure 2-7: Potential photovoltaic cell microchannel heat sink analyzed in Pellicone et al [129]**.**

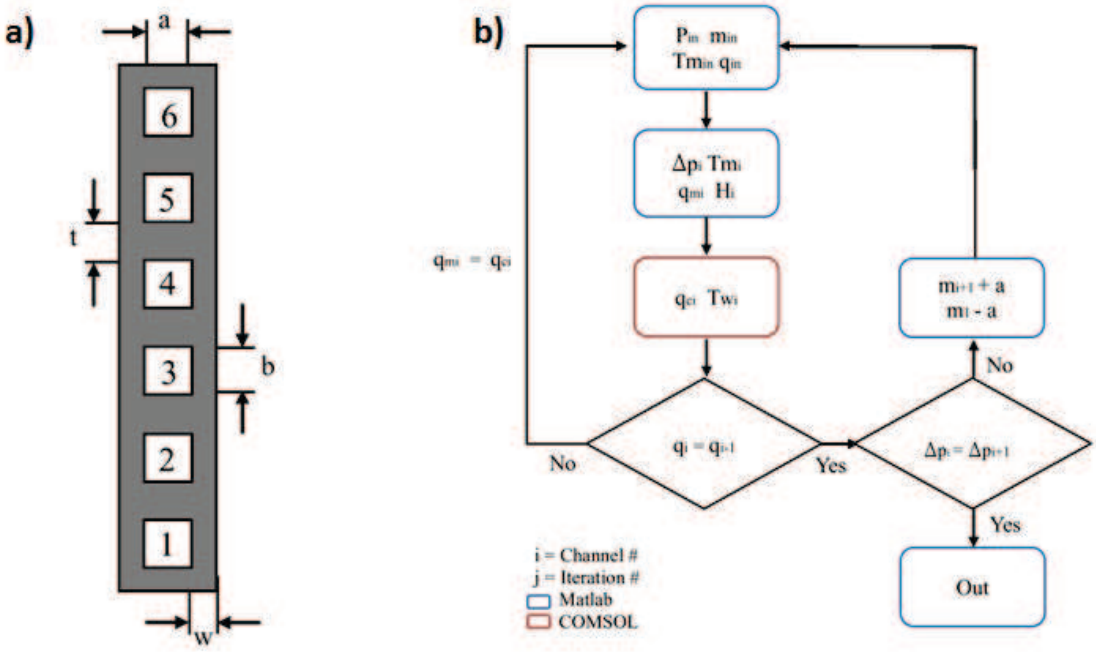

Figure 2-8: (a) Geometry examined and (b) the solution schematic employed by the computational model of Pellicone et al [129]**.**

published paper identified has attempted to do this. Pellicone et al. [129] combined COMSOL Multiphysics, an FEA platform, and MATLAB to examine heat spreading and efficiency in an array of stacked two-phase microchannels similar to those used to cool concentrated photovoltaic cells (see Figure 2-7). They created a single six channel stack geometry (see Figure 2-8a) in COMSOL and utilized a convective boundary condition to apply the prescribed heat transfer coefficient. They used MATLAB to perform heat transfer coefficient and pressure drop calculations using correlations from Yu et al. [73] and Mishima and Hibiki [24] for heat transfer coefficient and pressure drop, respectively.

Once initial fluid conditions are specified, an initial guess at the average heat flux and the pressure drop for each channel is made. MATLAB is then used to iterate until heat transfer coefficient and fluid temperature distributions are converged upon. These distributions are then used as inputs for the COMSOL model which solves the heat transfer equations and exports the average heat flux for each channel back to MATLAB. This process continues until the convergence criteria is met, at which point the pressure is examined. Mass flow rates are adjusted to match channel pressure drops with one another and the process begins again until both heat flux and pressure drop have converged. The solution algorithm is shown in Figure 2-8b. Once a solution is arrived at, information such as the pressure profile and heat flux for each channel can be extracted as well as additional information, such as three-dimensional temperature distribution, throughout the heatsink (Figure 2-9).

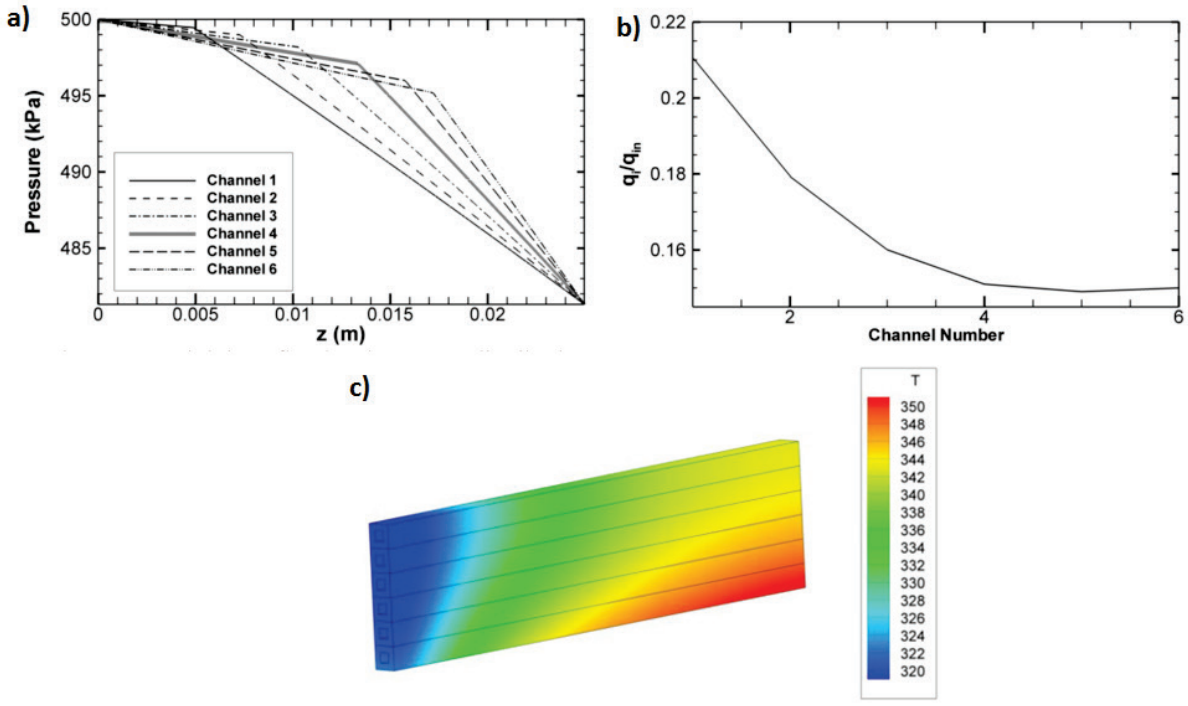

Figure 2-9: Results from Pellicone et al for (a) pressure distribution for each channel, (b) heat load for each channel and (c) three dimensional temperature distribution of the heat sink [129] **.**

This model demonstrates the ability of FEA to aid in heatsink design but fails to employ a strictly local heat transfer coefficient. The heat transfer coefficient varies between channels, but it is based on the average heat flux for any given channel. Nucleate boiling heat transfer coefficients are highly dependent on heat flux. Therefore, the assumption of average heat flux to determine the heat transfer coefficient is unacceptable for local hotspot cooling. The current work uses the same basic method demonstrated by Pellicone et al. but is designed to solve the conjugate heat transfer problem in a truly local manner.

2.3 Summary and Objectives of Current Work

To summarize the above discussion, flow boiling in microchannels, though poorly understood, is a very promising means for developing compact thermal management systems for the expected high heat load requirements of electronics. Efforts to gain greater understanding have taken both experimental and computational routes. Most experiments have been performed on small sample sizes and have often revealed contradictory heat transfer behaviors. Furthermore, most flow boiling studies in literature have examined moderate heat loads and operate on the assumptions of uniform heat flux and 1D heat conduction through the solid. Most real-world devices produce localized hot spots with very high heat fluxes, leading to heat spreading and yielding the fundamental assumptions of previous studies invalid. Published heat transfer correlations based on previous experiments do not predict average heat transfer coefficients adequately for these realistic situations. Correlations designed for predicting thermal management system performance in the future will need to address conjugate heat spreading and extreme heat fluxes. Therefore, local heat transfer coefficient correlations are needed. Unfortunately, the limitations of current measuring and fabrication techniques make gathering the necessary data

from experiments difficult and impractical. Computational and numerical modeling provide an alternative means to further our understanding of microchannel flow boiling.

The majority of computational work has utilized CFD along with current theories of microchannel heat transfer and flow dynamics to understand the underlying physics of flow boiling phenomena. These studies have revealed interesting insights, but they are currently limited to modeling extremely simple situations (single nucleation sites, single bubbles, etc.) because of the intensive computational demands of CFD. Comprehensive, three-dimensional system modeling will require significant hardware advancements which will not be available for some time. Another method for analyzing and predicting microchannel heat transfer is to ignore fluid flow behavior and use finite element methods (FEMs), combined with appropriate correlations, to solve the conjugate heat transfer problem. This method allows for fully customizable design and testing of potential heat sinks but relies on local heat transfer coefficient correlations, which may be inaccurate. The objective of the current work is to demonstrate just such a model and to use it to evaluate the validity of several representative heat transfer coefficient correlations when applied locally. This model provides an invaluable tool for the development of future thermal management systems.

The specific objectives of the current investigations are as follow:

- Develop an FEA model of a representative half-channel for a microchannel heat sink used to cool laser diode bars. A convective heat transfer boundary condition, utilizing an appropriate heat transfer coefficient correlation, will be used in lieu of attempting any complex fluid modeling. The model will also incorporate pressure drop via appropriate correlations.

- Validate the above-mentioned model in the case of uniform heat flux by comparison with analytical solutions.
- Evaluate the validity of five published heat transfer coefficient correlations when applied locally by comparison to previously obtained data from Bevis et al. [4,7].

Chapter 3: Experimental Setup and Procedures

In the present study, a silicon heat exchanger with parallel microchannels adjacent to a confined heat source is modeled and compared to data previously collected by Bevis [7]. This chapter gives brief descriptions of the test section and test facility designs, test matrix, testing procedure and test condition establishment from that study. It concludes with a short section detailing the experimental results to which the computational model is compared.

The motivation for the experimental work was to design a microchannel flow boiling heat exchanger for laser diode arrays. As laser diode wavelength and efficiency are both functions of diode temperature, thermal management of diode systems is of great importance in achieving optimal performance. This work was specifically aimed at maximizing diode power output while maintaining a device temperature of $\leq 60°C$. A joule heater with the dimensions of a typical laser diode bar was used as a surrogate heater in place of an actual laser diode.

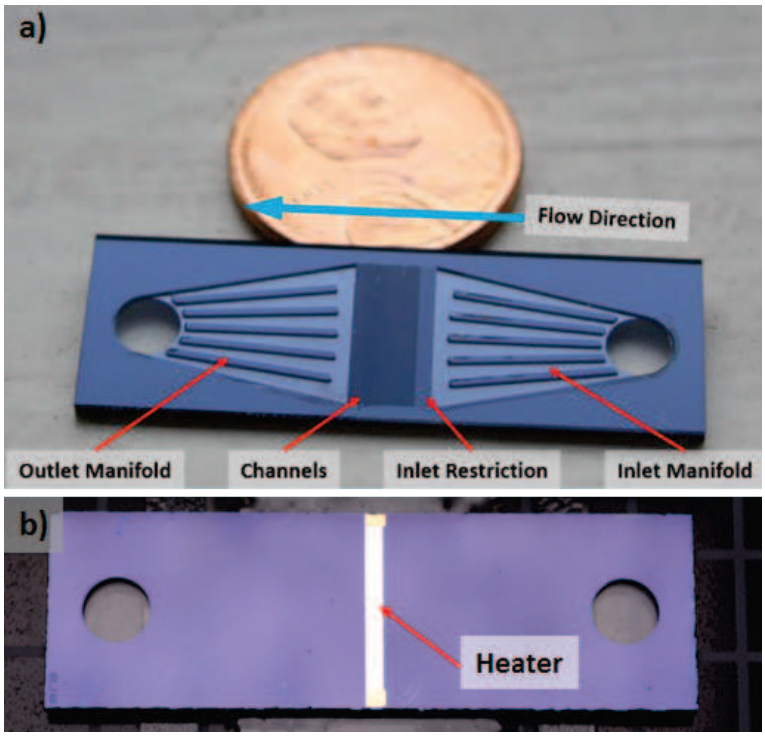

Figure 3-1: Test section (a) topside (penny shown for scale) [7] and (b) backside.

3.1 Test Section Description

The test section is a 12 mm × 38 mm silicon chip that has been etched and capped with a borosilicate glass cover to create fluid passages. The etch pattern consists of a number of features (Figure 3-1a) that directs the fluid through the test section. Single-phase fluid enters the test section through an inlet port and flows and into an inlet manifold. The inlet manifold distributes the fluid to an array of 125 parallel orifices, each of which feeds a single microchannel. The orifices are 10 µm in width, 132 µm in depth and 50 µm in length. The microchannels are 45 µm in width, 230 µm in height and 4950 µm in length so that, in total, an orifice and microchannel have a combined length of 5 mm. Fins separating the channels have a width of 35 µm. A cutaway view of this section is shown in Figure 3-2. A platinum strip heater with the same footprint as that of a typical laser diode (1 mm × 10 mm) is deposited on the backside of the chip, perpendicular to the fluid flow so as to apply heat in the middle of each channel (Figure 3-1b). As fluid flows through the channels and absorbs heat it is converted into a two-phase mixture. Upon exiting the channels, this mixture is collected through the outlet manifold and leaves the test section through the outlet port.

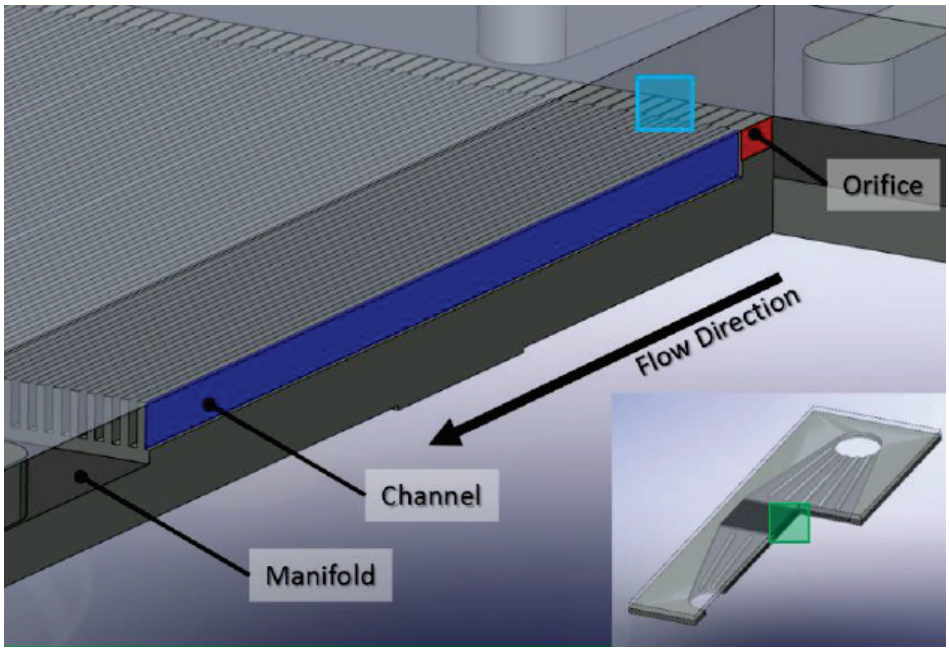

Figure 3-2: Cutaway view showing test section channel and orifice [7].

The ribs visible in the manifolds of Figure 3-1a are present for structural integrity and are not designed to play a role in fluid distribution. Measured dimensions for the test piece modeled in this study are given in Table 3-1.

Multiple test sections are fabricated on a single 500 µm thick silicon wafer measuring 4 in in diameter before being separated by dicing with a diamond saw. The first step in fabrication is the etching process. This is performed at Lawrence Livermore National Laboratory (LLNL) and utilizes a deep reactive-ion etching (DRIE) Bosch process, the details of which can be found in Bevis [7]. This is a standard microelectromechanical systems (MEMS) process, capable of

Table 3-1: Average dimensions of test section features as measured with destructive testing via SEM after experimentation. Each test section contained 125 parallel channel/fin units.

Feature	Dimension Type	Dimension (µm)
Manifold	Width	4000 - 10000
	Depth	200
Inlet/Outlet Port	Diameter	4000
Orifice	Width	10
	Depth	132
	Length	50
Channel	Width	45
	Depth	230
	Length	4950
Fin	Width	35

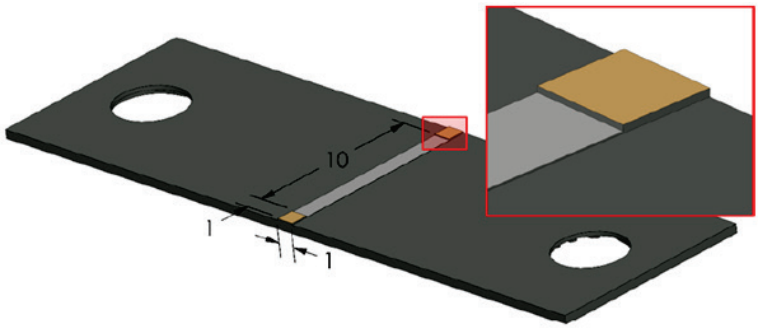

Figure 3-3: Deposited heater and contact pads on the test piece backside. Dimensions are given in mm [7].

producing high aspect ratio features. Once the wafer is etched and cleaned, a thin oxide layer (~1 nm) is formed on the back surface by exposure to oxygen (O_2) at high temperatures (~1100°C). This oxide layer electrically insulates the test piece from the thin film heater. A 500 μm sheet of borosilicate glass is then anodically bonded to the topside of the wafer to seal the fluid passages while still allowing for flow visualization. The last step is metal deposition through a stainless steel direct contact mask to add a thin platinum strip heater.

The heater assembly consists of several different layers of deposited metals. Since platinum does not adhere directly to silicon oxide (SiO_2), a thin rectangular layer of titanium (10 nm)—which bonds to both silicon and platinum—is first deposited with dimensions 1 mm × 12 mm along the midline of the backside of the channels. Next, a 200 μm layer of platinum is deposited. 1 mm × 1 mm contact pads are then added at either end of this platinum strip with addition of several more layers: 10 nm of titanium for adhesion, 500 nm of nickel for the electrical contact, and 100 nm of gold to prevent oxidation of the contact pads. A solid model depicts both the platinum heater and the contact pads in Figure 3-3 [7]. The electrical resistance of the contact pads is significantly lower than that of the connecting platinum strip, ensuring that heat dissipation in this area is negligible compared to the 10 mm heater length located between the pads and directly underneath the microchannel array.

3.2 Test Facility Description

A custom test facility (Figure 3-4) was designed and constructed by Bevis to incorporate the test section into a closed fluidic loop allowing for heat transfer characterization [4,7]. The main functions of the test facility are as follows: interface with test section, precisely and accurately measure and control inlet/outlet fluid temperature, pressure and flow rate, control and measure power supplied to the heater, measure test piece backside temperature, and visualize flow during

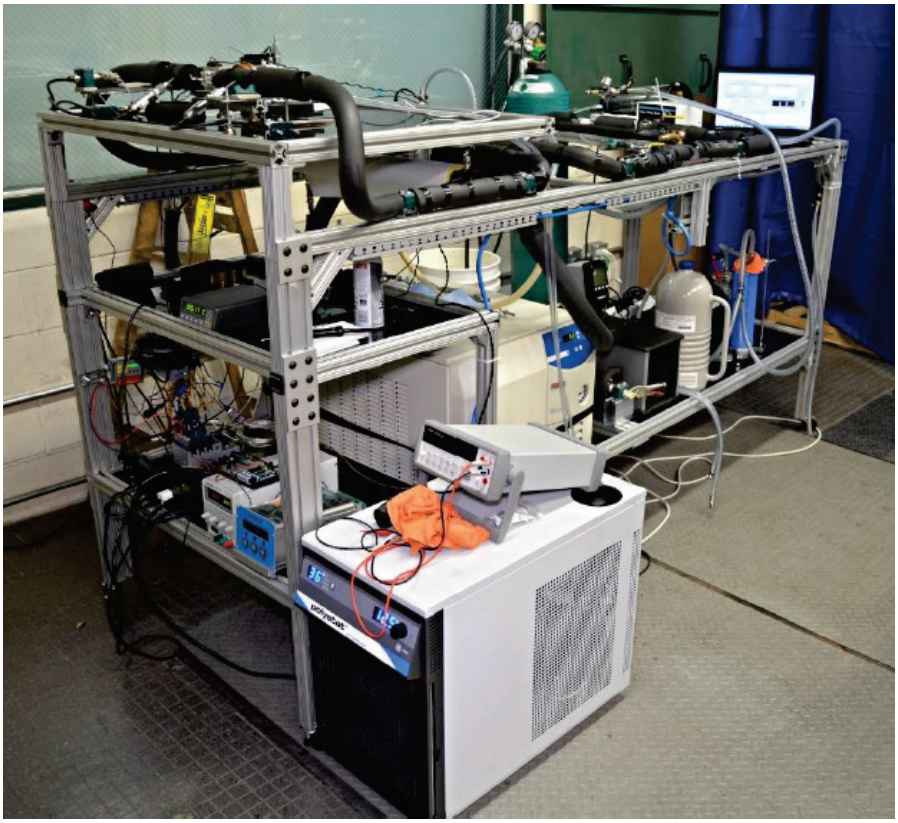

Figure 3-4: Test facility overview [7].

testing. Each of these functions will now be described in turn. A process diagram of the facility is shown in Figure 3-5 for reference.

3.2.1 Test Section Interface

The test section interface must accomplish two jobs. The first is to connect the test section to the fluidic loop and the second is to electrically connect the heater to the power supply. The fluidic interface is established when the test piece is press fit into a block of polyether ether ketone (PEEK) that has been machined to accommodate fluid paths. The PEEK block has ¼" NPT fittings that connect to the rest of the facility as well as two 4 mm ports that align with the 4 mm inlet and outlet ports of the test section. A Gore gasket is placed between the silicon and the PEEK and a clamping mechanism is used to press the two together. The purpose of the clamping mechanism is simply to provide even pressure across the silicon to establish the fluidic seal without fracturing the test piece.

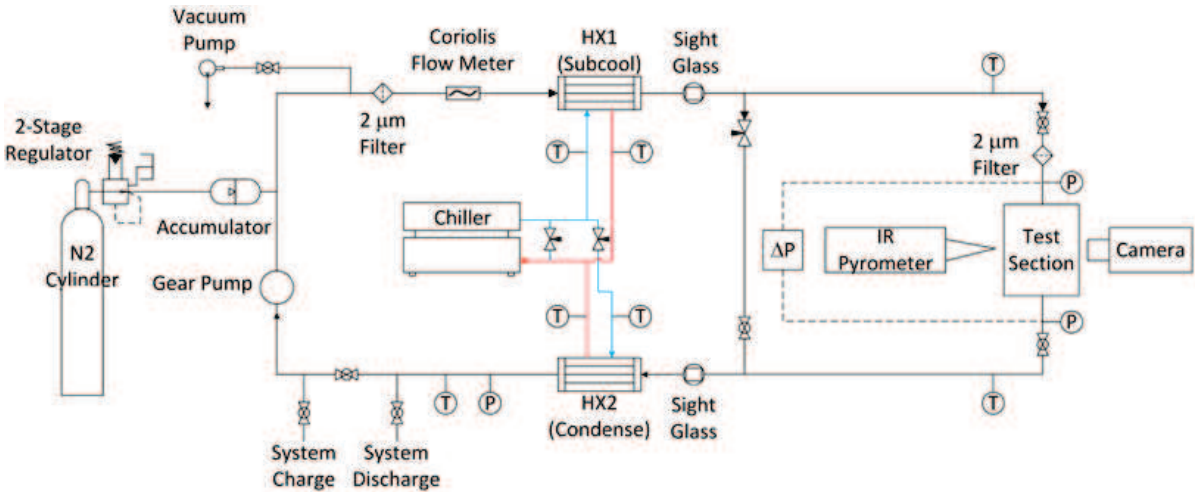

Figure 3-5: Process diagram of test facility [7].

The electrical connection is established via a custom wiring harness created to fit the central section of the test piece (Figure 3-6). The harness is a multi-part ceramic structure that clamps onto the test piece and forces the heads of two copper pins to press into the contact pads on either side of the test section heater. Electrical leads, soldered to the pins, then connect to an electrical terminal mounted on the PEEK block which is also connected to a 60V/6A power supply (Instek SPS-606).

The wiring harness was designed such that it would not interfere with the fluidic clamp. Separate mechanisms were necessary to allow individual pressure control for both interfaces. Both structures were designed to keep the channels and heater exposed to allow for flow visualization and heater temperature sweeps as will be discussed later. The amount of power delivered to the heater is determined from measurement of the power supply output current with a high accuracy shunt resistor (Ohm Labs, CS10) and measurement of the voltage drop across the heater. The entire interface structure is shown in Figure 3-7.

3.2.2 Fluid State Measurement and Control

Proper heat transfer characterization requires an accurate knowledge of fluid states immediately prior to and after exiting the test section. Temperature and pressure measurements in both locations are made with K-type thermocouples (Omega, TC-K-NPT-UG-72) and high

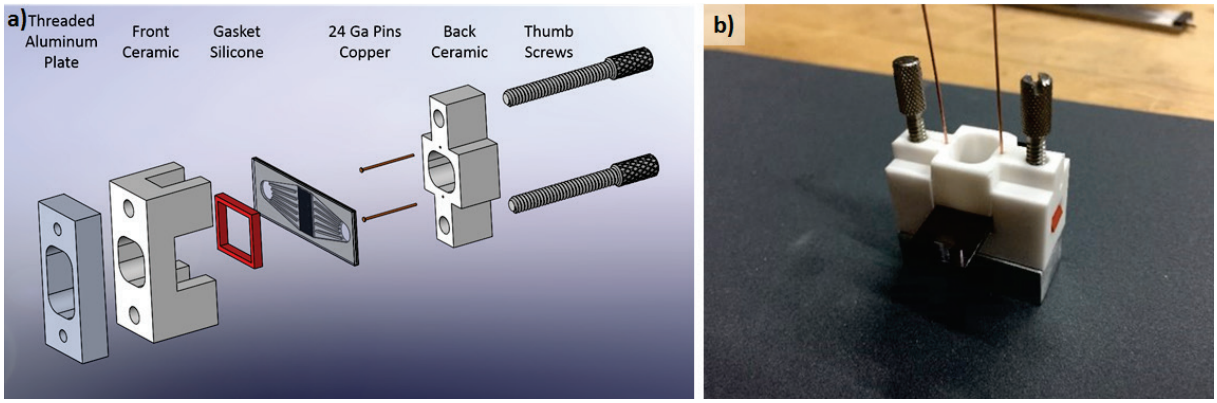

Figure 3-6: Electrical harness for test section. (a) Exploded model view and (b) assembled view.

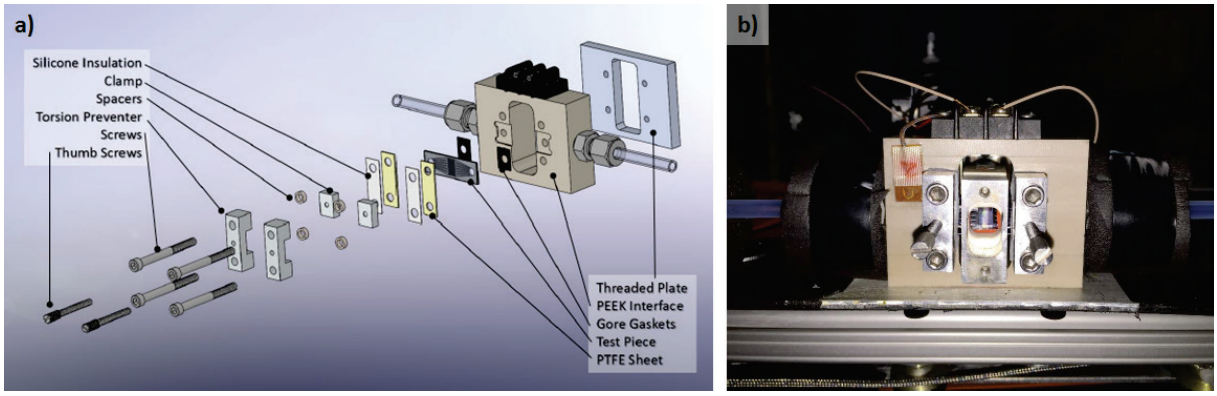

Figure 3-7: Test section interface (a) exploded and (b) installed views. Gore gaskets provide the fluidic seal while the other hardware is designed to place even pressure on the test section to create the seal and avoid fracturing [7].

accuracy absolute pressure transducers (Omega, PX409-005A1/MMA100C1P3C0T4A6). A differential pressure transducer (Omega, PX409-100DWUI) across the section is also used for greater accuracy. It is desired that the fluid be slightly subcooled entering the channels. To ensure this, sight tubes connect to the inlet and outlet of the PEEK block to allow for visualization.

Mass flow rate through the system is controlled with a positive displacement gear pump (Micropump, GA-T32/wu-75211-10) and measured with a Coriolis flow meter (Rheonik, RHM015). The flow meter is placed between the gear pump and the test section. The speed of the pump is manually controlled to maintain the desired flow rate. Temperature is controlled via two heat exchangers in contact with a secondary fluid loop that connects to a stand-alone 3.5 kW chiller (Merlin M150LR-CP55). One heat exchanger is located downstream of the test section to cool the

two-phase fluid down to a single-phase liquid before entering the gear pump and the second is located just upstream of the test section in order to control the degree of subcooling. Working fluid temperatures are adjusted manually as desired by adjustment of both the secondary cooling loop supply temperature and the proportion of flow directed to each heat exchanger via a system of valves and a bypass loop. Pressure is controlled with the addition of an accumulator into the system between the gear pump and the flow meter. One side of the accumulator is connected to the fluid loop and the other to a source of dry air or N_2 gas. A bladder inside the accumulator separates the fluid side from the air side. Adjustment of the air side pressure similarly adjusts the fluid side pressure. Various other temperature sensors located throughout the system are present for ease of control.

3.2.3 Heater Temperature Measurement and Flow Visualization

The temperature of the platinum heater is of great interest in characterizing heat transfer. The use of thermocouples proved impractical due to the exceedingly small size of the heater and the difficulty in accessing it once incorporated into the system. Instead, temperature was measured optically utilizing an infrared pyrometer. The pyrometer (MicroEpsilon, CTL-CF1-C8) measures an average temperature over a circular spot size that is 0.9 mm in diameter. Prior to incorporation into the system, the pyrometer went through extensive in-house sensitivity testing and calibration. Nominally the pyrometer has a working distance of 70 mm and should be oriented directly perpendicular to the surface being measured. These parameters were adhered to as closely as possible, but testing determined that temperature measurements were insensitive ($< 0.2^{\circ}$C change) to deviations of $\pm 20^{o}$ in incidence angle and ±12.7 mm in working distance. Temperature measurements were also found to be insensitive to ambient light level. The pyrometer was determined to be sensitive to the temperature of the pyrometer body, so a custom copper coiled

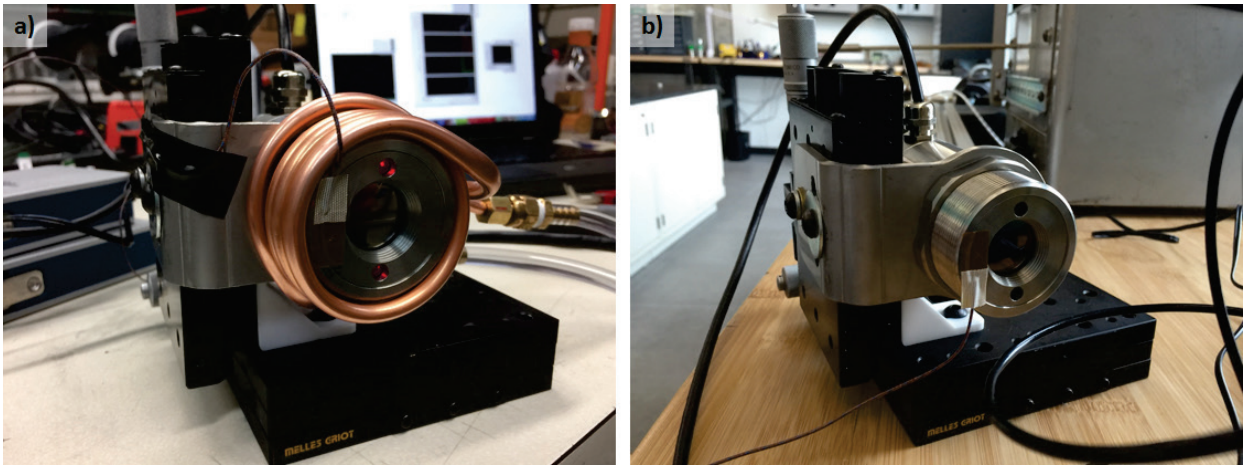

Figure 3-8: Infrared pyrometer (a) with and (b) without copper cooling mechanism. The assembly is mounted on a two-axis stage.

heat exchanger was designed to maintain the pyrometer at a temperature of 20.0 ± 0.5°C. The pyrometer and attached cooling mechanism are shown in (Figure 3-8). To ensure accurate optical readings, test piece backsides were coated with a thin, uniform layer of high temperature, high emissivity black paint (Rutland, 81). The pyrometer is mounted on a two-axis stage to allow precise control over measurement spot location.

A window machined into the electrical harness on the test piece backside allows for optical temperature sweeps horizontally along the entire length of the channels and vertically along a 3 mm portion of the heater. A similar window on the topside of the test piece provides optical access to the channels for flow visualization (see Figure 3-7b). A digital camera with an attached microscope objective lens allows for visual confirmation that flow is distributed equally to all channels and for visual observation of the transition location from single-phase to two-phase flow. This transition location is determined in post-processing using images taken from recorded video and is assumed to be the average over ten channels at three separate time steps. Figure 3-9 shows an example of an image used in post-processing.

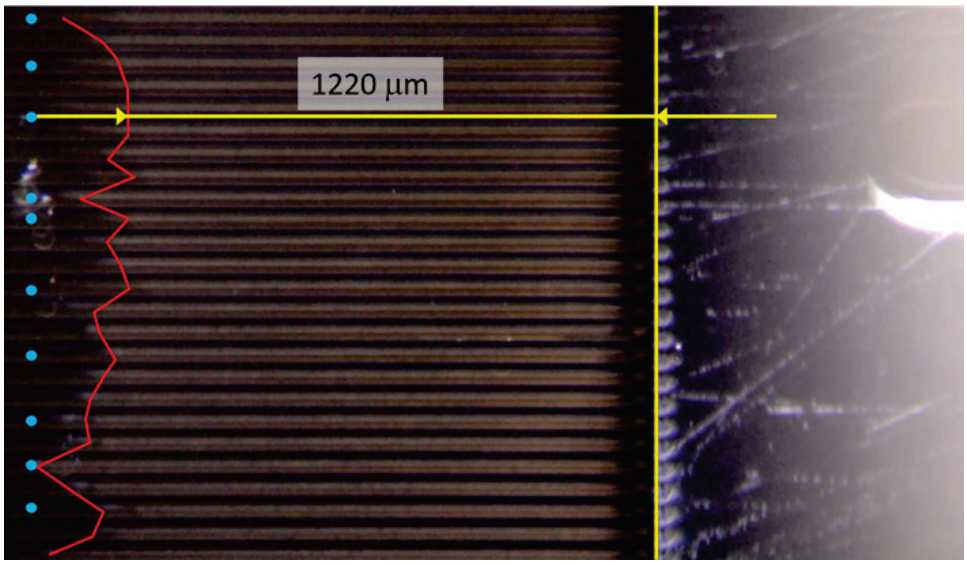

Figure 3-9: Sample image used for transition location determination. The red line indicates the transition location for individual channels and the blue dots indicate which channels were sampled to calculate the average [7].

3.3 Testing Procedure and Results

Tests were performed to determine how much heat each test section could dissipate while maintaining specific nominal target heater temperatures of 40°C, 50°C and 60°C at different sets of operating conditions. For the current work, the target mass flow rate was 100 g min^{-1}—giving a target mass flux of 1481 kg m^{-2} s^{-1}—and the target transition saturation temperature was 20°C, corresponding to a pressure of 83 psi (572 kPa) for the working fluid of R134a. The target inlet temperature was 15°C to ensure a moderate degree of subcooling. Due to highly restrictive inlet orifices, there is significant pressure drop between the upstream pressure sensor and the microchannels. The necessary inlet fluid pressure was thus estimated from single-phase, incompressible (liquid) tests run at identical operating conditions. For estimation purposes, the total single-phase pressure drop across the test section ($\Delta P_{sp,tot}$) was assumed to come entirely upstream of the channels (mainly from the orifices) and could thus be used to determine the target inlet pressure ($P_{in,target}$) from the target saturation pressure ($P_{sat,target}$) as follows:

$$P_{\text{in,target}} = P_{\text{sat,target}} + \Delta P_{\text{sp,tot}} \tag{3.1}$$

For the current case, the single-phase pressure drop measured roughly 7.4 psi (51 kPa). The target inlet pressure is then determined by adding this value to the target saturation pressure of 83 psi to yield a pressure of 90.4 psi (623 kPa). This target inlet pressure was used for all tests at these operating conditions. Actual inlet temperature and pressure varied slightly from the target values.

Once the desired operating conditions are reached and steady state is achieved, power is delivered to the test section heater. Heater temperature is carefully monitored via the pyrometer and power is slowly increased until the desired heater temperature is reached. Flow rate, temperature and pressure are closely monitored and, if necessary, adjusted via the means described in Section 3.2 to maintain the target inlet conditions throughout testing. When steady state is again achieved, data is recorded. All measurements in the system are collected through a data acquisition (DAQ) system from National Instruments consisting of three separate temperature, current and voltage modules (National Instruments, NI 9214, NI 9207, NI 9221). The data is then consolidated and recorded using a custom designed LabVIEW data collection program. The relevant recorded data consists of mass flow rate, inlet and outlet fluid temperatures, inlet and outlet fluid pressures and the results of heater temperature sweeps—described shortly—performed with the pyrometer. A short video clip of the flow in the channels is recorded during testing.

Vertical temperature sweeps of the heater showed little temperature variation ($< \pm 1°C$). Combined with visual observation that flow was evenly distributed throughout the channels, it was determined that taking one horizontal temperature sweep over one set of channels was adequate to characterize the temperature profile of all channels. Horizontal temperature sweeps begin with the pyrometer centered on the heater. The measurement location is moved downstream to the channel exits—a distance of 2.5 mm—in 0.5 mm increments. Once the channel exits are reached, the pyrometer is moved to the channel inlets and stepped back toward the heater in 0.5 mm increments.

Multiple measurements from the recording LabVIEW program spanning a period of at least 5 seconds are collected at each location. The central heater temperature is measured first and last in addition to a measurement taken when the pyrometer is moved from the channel exits to the channel inlets to ensure steady state is maintained. As mentioned earlier, the pyrometer measures and average temperature over a 0.9 mm spot size. This results in measurement overlap during the 0.5 mm steps to achieve greater temperature profile fidelity.

Upon completion of the temperature sweep, the power is then slowly increased to the next target heater temperature. The process repeats until all target temperatures have been tested. The data collected from this testing procedure is then used in the current work to validate the computational modeling. A summary of experimental results obtained from three different tests used for comparison in this work is shown in Table 3-2. If desired, a more comprehensive description of the testing procedure, as well as the results of additional testing, has been given by Bevis [7].

Table 3-2: Summary of experimental results.

Property	Units	Nominal Heater Temperature		
		40 °C	50 °C	60 °C
Actual Heater Temp	[°C]	39.9	51.2	61.6
Mass Flow Rate	[g min^{-1}]	100.8	99.8	99.7
Inlet Pressure	[kPa]	621.3	623.1	633.4
Inlet Temp	[°C]	14.5	14.5	11.5
Total Heat Dissipated	[W]	36.4	69.8	99.3
Applied Heat Flux	[kW m^{-2}]	3643	6981	9934

Chapter 4: Computational Model

Most published heat transfer coefficient correlations for microchannel flow boiling assume a uniformly applied heat flux and consider only 1D conduction of heat through the solid. This allows for the heat flux at the channel/fluid interface to be known. Extremely high heat fluxes centered at localized hotspots create thermal management situations in which these assumptions are inadequate. Conjugate heat transfer must be considered, and local heat transfer coefficient correlations are necessary in order to do this. Though collecting the desired data from experiments to develop such correlations is currently impractical, if not impossible, finite element method (FEM) modeling—also referred to as finite element analysis (FEA)—presents a way to move forward with both correlation development and, given appropriate correlations, heat exchanger design. The present work utilizes FEA to examine the potential validity of five published microchannel flow boiling heat transfer coefficient correlations when used to determine local heat transfer coefficients. The model results are then compared with previously acquired experimental data.

This work uses COMSOL Multiphysics 4.4 to perform the FEA simulations. FEA consists of breaking down a large and/or complex domain into a finite number of smaller, simpler elements. Though the necessary equations may be analytically unsolvable when applied to the original problem, they may be solvable, at least approximately, for each of the smaller elements. These solutions can be stitched together with appropriate boundary conditions and then be used to create an approximate solution for the original problem. This approximate solution can be made close enough to the actual solution that there is no practical difference between the two. FEA thus provides an excellent tool to examine the complicated nature of conjugate heat transfer in microchannels.

For the present model, COMSOL has been integrated with MATLAB using LiveLink for MATLAB, a software package available from COMSOL, which allows MATLAB scripts to access all information present in a given COMSOL model. MATLAB can then manipulate the data as needed and update the COMSOL model, if desired. COMSOL is used to solve the heat transfer equations while MATLAB is used to solve for pressure drop through the channel.

The following sections give a detailed description of the model. Section 4.1 describes how the model is set up in COMSOL. This begins with details on the basic method of setting up a model and continues with specifics relating to the current model, including the manner in which the various heat transfer coefficient correlations are implemented. Section 4.2 then presents each of the five correlations herein tested. Section 4.3 explains the method for determining the local fluid state throughout the model channel. Sections 4.4 - 4.7 then describe the mesh and solution method, and provide validation for the model.

4.1 COMSOL Multiphysics Organization

COMSOL Multiphysics is an FEA tool with the built-in structure to solve many engineering problems. Model creation begins with the specification of spatial dimension and the particular physics modules to be incorporated. Individual physics modules contain the equations necessary to solve a certain set of problems and can either be used individually or incorporated one with another. The current model has three-dimensional spatial geometry and utilizes only the *Heat Transfer in Solids* module. This module can solve the coupled heat conduction and convection equations for each finite element. The model must also be assigned one of various *Study* types, such as *Time-Dependent* or *Stationary*. The current model examines a steady-state situation and thus employs a *Stationary Study*. Once these specifications are made, the model is created.

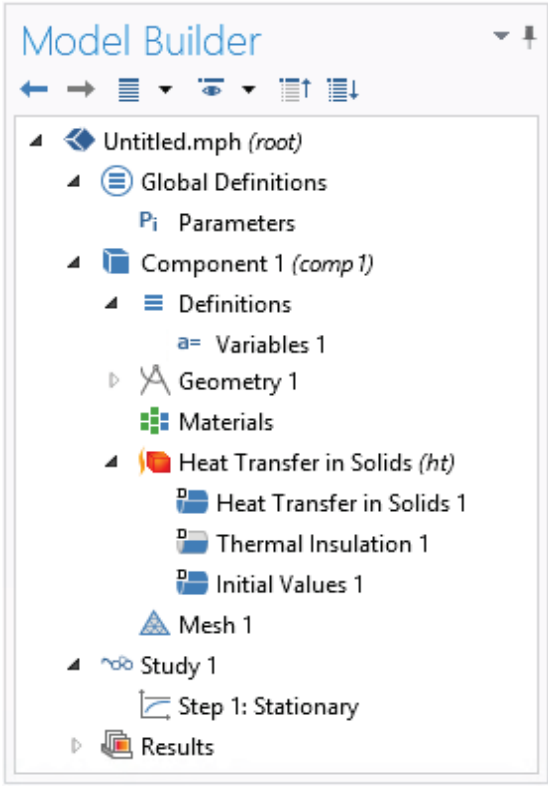

Figure 4-1: Default COMSOL *Model Builder Tree.*

Models are organized in a *Model Builder* window which contains a *Model Tree.* Each of the various model components are defined by branches, or *Nodes* in that tree. The default Model Tree is shown in Figure 4-1. The basic method for solving a custom problem is as follows: create the geometry, assign materials, apply boundary conditions to external surfaces, create a mesh that defines element shape and size and then let the software iteratively solve until convergence is achieved. These tasks are accomplished by editing the appropriate node. To add further functionality, additional nodes can be added to the tree. Three key additional nodes are *Parameters*, *Variables* and *Functions*, which all allow for the definition of user customized values and equations. Settings for any selected node—including the node name—are editable in a separate window. A basic introduction of parameters, variables and functions is given here.

Parameters

Name	Expression	Value	Description
W_ch	45 [um]	4.5000E-5 m	Channel Width
W_fin	35 [um]	3.5000E-5 m	Fin Width
H_ch	200 [um]	2.0000E-4 m	Fin/Channel Height
H_floor	300 [um]	3.0000E-4 m	Floor Thickness
H_cell	H_ch + H_floor	5.0000E-4 m	Wafer Thickness
L_ch	5 [mm]	0.0050000 m	Channel Length
W_unit	W_ch + W_fin	8.0000E-5 m	Unit Cell Width
W_hcell	W_unit/2	4.0000E-5 m	Half Cell Width
A_ch	W_ch * H_ch	9.0000E-9 m^2	Channel Cross Section Area
D_h	4*A_ch/(2*(H_ch+W_ch))	7.3469E-5 m	Hydraulic Diameter
beta	W_ch/H_ch	0.22500	Aspect Ratio
T_in	284.65 [K]	284.65 K	Inlet Fluid Temperature
m_dot	(.0997 / (N_ch*60)) [kg/s]	1.3293E-5 kg/s	Mass Flow Rate for Channel
N_ch	125	125.00	Number of Channels
m_flux	m_dot/A_ch	1477.0 kg/(m^2·s)	Mass Flux for Channel
g	9.81 [m/s^2]	9.8100 m/s^2	Gravitational Constant
P_in	595.1 [kPa]	5.9510E5 Pa	Inlet Pressure

Figure 4-2: Model parameters.

Variables

Name	Expression	Unit	Description
htc_sp	Nu_sp_km*k_l/D_h	W/(m^2·K)	
htc_tp	28*(q_flux*1[m^2/W])^(2/3)*(m_flux*1[m^2*s/kg])^(-0.26)*x_q^(-0.1)*1[W/(m^2*K)]	W/(m^2·K)	

Figure 4-3: Example heat transfer coefficient inserted as a *variable*.

4.1.1 Parameters, Variables and Functions

Parameters are typically user inputs to the model and are globally available for use in all nodes. The parameters of the current model are shown in Figure 4-2. These include values used to define geometric dimensions, definitions of global constants such as gravitational constant and channel cross-sectional area that can be used in calculations performed elsewhere. Other model inputs such as mass flow rate, and inlet fluid temperature and pressure, are also defined here.

Variables are defined in a similar manner to parameters. While a COMSOL variable can be a constant, it need not be. It can also be used to define a simple mathematical formula or even a complex relation such as the heat transfer coefficient correlations found in Section 4.2. An example is shown in Figure 4-3. In this way, COMSOL variables can actually be used to define custom multi-variable functions. COMSOL also contains several built-in *functions*. These are

functions of one variable only, but many of them are functions that cannot be easily defined in the COMSOL variable section, such as interpolation and step functions. Built-in functions are used in the current model to gather fluid property information from external files, switch between single- and two-phase equations, find maximum values and perform integrations among other things. All parameters, variables and functions are described in Appendix B.1.

4.1.2 Geometry

The computational domain consists of a half channel unit identical to those in the experimental test section. Only the solid channel wall and floor are modeled. Visualization of channels during testing revealed no signs of flow maldistribution, and temperature sweeps taken with the pyrometer along the heater (perpendicular to the flow direction) showed only minimal variations ($< \pm 1°C$). These observations justify the consideration of one half channel as a representative unit for modeling.

The geometry was produced in COMSOL by first creating the cross-sectional profile of a half channel unit and then extruding it to create to the full unit. All dimensions were defined in the *Parameters* node and are set to match actual test section geometry. To begin, two overlapping rectangles were created in the XZ plane to form the basis of the design (Figure 4-4a). For convenience, the positive/negative Z-directions and the positive/negative X-directions will be referred to as up/down and left/right, respectively. The first rectangle, rectangle A, represents the solid silicon and has a height equal to the thickness of a silicon wafer (500 μm) and width equal to that of one half of the combined width of a channel (45 μm) and a fin (35 μm). For reference, the lower left corner of rectangle A is located at the origin. The second rectangle, rectangle B, represents the area removed from the silicon wafer during the etching process. This will form the

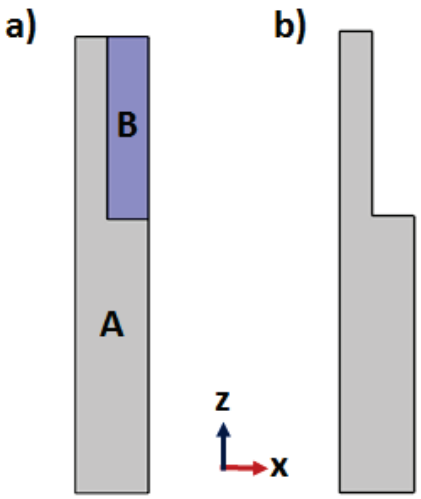

Figure 4-4: Half channel cross-sectional profile construction: (a) a small rectangle is subtracted from a larger rectangle to create (b) the channel profile.

actual channel in the model and so has the height of a channel (200 μm) and the width of one half of a channel (22.5 μm). Rectangle A and rectangle B share the same upper-right corner locations. A Boolean→ Subtract operation is used to remove the area occupied by rectangle B from the area occupied by rectangle A, leaving the cross-sectional profile that is desired (Figure 4-4b). This half channel profile is extruded in the positive Y-direction to create the three-dimensional half channel geometry.

At this point, the geometry is a single domain with each external face treated by COMSOL as a single, unique boundary. The geometry must be subdivided in order to define a distinct heater region. This is accomplished by slicing the geometry with two XZ planes, located at either end of the heater. Further subdivisions are added to aid in the meshing process. These divisions are shown in Figure 4-5 and specific dimensions of the geometry and slice planes are shown in Table 4-1 .

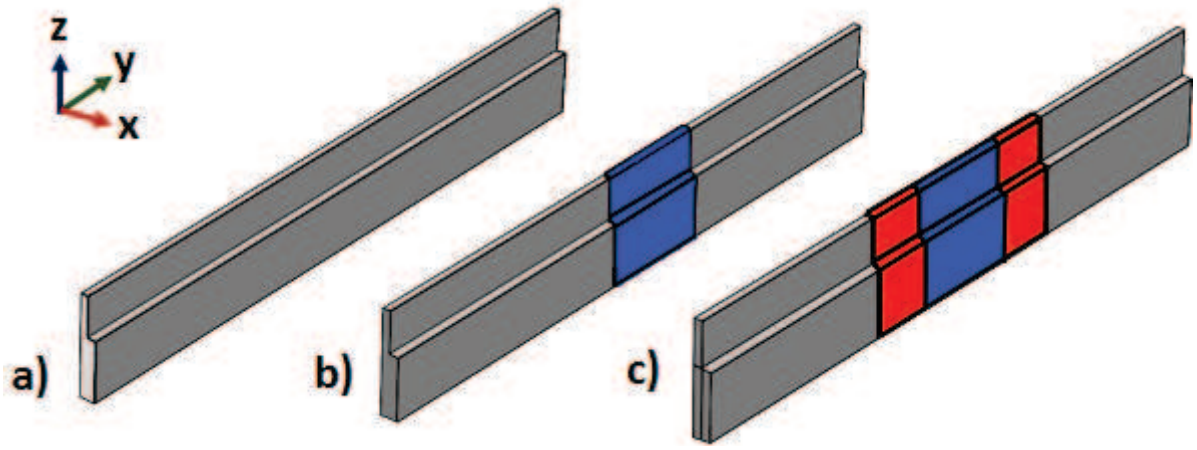

Figure 4-5: Model half channel geometry as (a) a single domain, (b) with heater subdivisions (blue) and (c)with remaining subdivisions (red) to aid in meshing. Models are not to scale in order to emphasize certain geometric features.

Table 4-1: Locations of key geometric features. Channel length is 5 mm.

Feature		Location (x,y,z) (μm)
Channel Profile	Lower Left Corner	(0, 0, 0)
	Lower Right Corner	(40, 0, 0)
	Upper Left Corner	(0, 0, 500)
Heater Slice Planes	XZ Plane	(…, 2000, …)
	XZ Plane	(…, 3000, …)
Other Slice Planes	XZ	(…, 2500, …)
	XZ	(…, 3500, …)
	XY	(…, …, 300)
	YZ	(35, …, …)

4.1.3 Materials

Since only the solid channel/fin is modeled, the only material needed is silicon, which comes pre-installed in the COMSOL material library. However, the relevant property for the current model, thermal conductivity, is given as an average value over common temperature ranges. Significant temperature gradients exist within the half channel unit, so a temperature dependent thermal conductivity is desired. Because COMSOL has the capability of accepting user defined functions to define material properties, a piecewise linear fit to silicon thermal

conductivity values over the temperature range of 0°C - 100°C was used in place of the default value. Thermal conductivity values were determined using the Engineering Equation Solver (EES) built-in database [130]. Following is the curve-fit used:

$$k = \begin{cases} 171.94 - 0.8603 \cdot T \quad [W/mK] & 0\ ^{\circ}\mathrm{C} \le \mathrm{T} \le 27\ ^{\circ}\mathrm{C} \\ 161.28 - 0.4918 \cdot T \quad [W/mK] & 27\ ^{\circ}\mathrm{C} \le \mathrm{T} \le 100\ ^{\circ}\mathrm{C} \end{cases} \tag{4.1}$$

4.1.4 Boundary Conditions

Boundary conditions are applied under the *Heat Transfer in Solids* node. All external model faces must be assigned boundary conditions. Figure 4-6 gives the terminology that will be used to describe these boundary conditions and to refer to specific model features. The channel front, back, top, ends and base (excluding the heater) are all assigned adiabatic boundary conditions. Symmetry was established from test section backside temperature measurements and flow visualization as described in Section 4.1.2. This justifies the assignation of an insulative, adiabatic boundary condition to the front and back. The top surface is bonded to a layer of borosilicate glass which presents a high thermal resistance compared to conduction through the

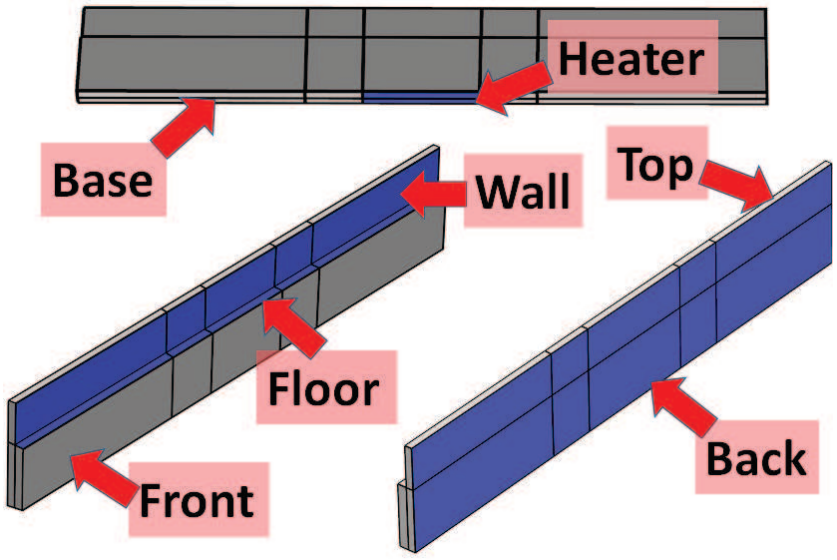

Figure 4-6: Terminology used to describe half channel unit.

silicon. A more comprehensive energy balance is given in Appendix A, but a brief calculation here should convince the reader.

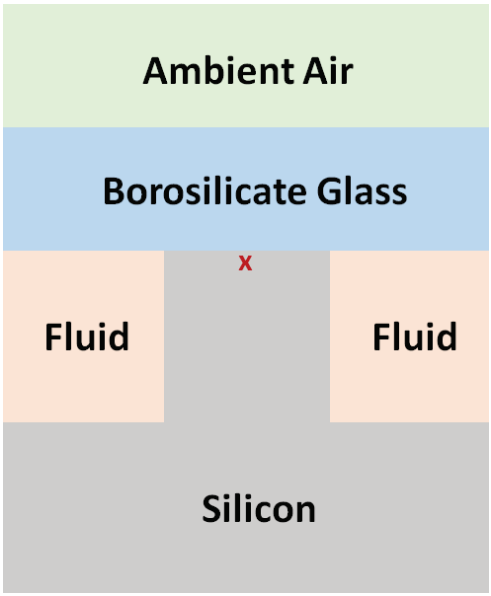

Figure 4-7: Schematic of heat transfer origination location. Not to scale.

Consider heat transfer originating at the tip of a fin, along the midline of that fin, as depicted by the red 'x' in Figure 4-7. The typical thermal conductivity of borosilicate glass is ~1.14 W m^{-1} K^{-1} and the thickness (t) of the glass is 500 µm. I calculate the thermal resistance (R) for conduction through the glass as follows:

$$R_{\text{glass}} = \frac{t}{k} = \frac{5\times10^{-4}\ \text{m}}{1.14 W\ \text{m}^{-1}\ \text{K}^{-1}} = 4.39\times10^{-4}\ \text{m}^2\text{K W}^{-1} \tag{4.2}$$

Assuming a fairly generous natural convection heat transfer coefficient between the glass and ambient air of 15 W m^{-2} K^{-1}, the thermal resistance for convection to the air is found as follows:

$$R_{\text{ambient}} = \frac{1}{h} = \frac{1}{15 W\ \text{m}^{-2}\ \text{K}^{-1}} = 6.67\times10^{-2}\ \text{m}^2\text{K W}^{-1} \tag{4.3}$$

The total thermal resistance for this glass pathway is then the sum of R_{glass} and $R_{,\text{ambient}}$:

$$R_{\text{tot,glass}} = R_{\text{glass}} + R_{\text{ambient}} = 6.71\times10^{-2}\ \text{m}^2\text{K W}^{-1} \tag{4.4}$$

The thermal resistance of the pathway through the silicon fin and into the fluid can likewise be considered. The thermal conductivity for silicon at room temperature is ~140 W m^{-1} K^{-1}. Considering heat originating at the middle of the fin (the back surface of the model)—the furthest distance possible from the fluid interface— there is a silicon thickness of 17.5 μm. I calculate the thermal resistance of this:

$$R_{\text{silicon}} = \frac{t}{k} = \frac{1.75\times10^{-5}\ \text{m}}{140 W\ \text{m}^{-1}\ \text{K}^{-1}} = 1.25\times10^{-7}\ \text{m}^2\text{K W}^{-1} \tag{4.5}$$

Assuming a very conservative heat transfer coefficient of 2000 W m^{-2} K^{-1}, I find

$$R_{\text{fluid}} = \frac{1}{h} = \frac{1}{2000 W\ \text{m}^{-2}\ \text{K}^{-1}} = 5.00\times10^{-4}\ \text{m}^2\text{K W}^{-1} \tag{4.6}$$

The total thermal resistance of the silicon pathway is then

$$R_{\text{tot,silicon}} = R_{\text{silicon}} + R_{\text{fluid}} = 5.00\times10^{-4}\,\text{m}^2\text{K W}^{-1} \tag{4.7}$$

Comparing the two values one can see that the thermal resistance of the glass pathway is two orders of magnitude greater than that of the silicon pathway. Combined with the small temperature difference between the fin top and the ambient air, heat transfer through the glass can be considered to be negligible.

A similar argument supports use of the adiabatic boundary condition on the base (excluding the heater). Heat can either be transferred to the fluid through the silicon or it can be convected to the ambient air. Thermal resistance through the 300 μm silicon floor is

$$R_{\text{floor}} = \frac{t}{k} = \frac{3.00\times10^{-4}\ \text{m}}{140 W\ \text{m}^{-1}\ \text{K}^{-1}} = 2.14\times10^{-6}\ \text{m}^2\text{K W}^{-1} \tag{4.8}$$

Convective resistance between the channel floor and the fluid is the same as before (R_{fluid}, 5.00×10^{-4} W m^2 K^{-1}), so the total thermal resistance of this pathway is

$$R_{\text{tot,floor}} = R_{\text{floor}} + R_{\text{fluid}} = 5.02\times10^{-4}\,\text{m}^2\text{K W}^{-1} \tag{4.9}$$

The alternate pathway resistance is simply R_{ambient} from before (6.67×10^{-2} W m^2 K^{-1}). Again, the resistance for the ambient air pathway is two orders of magnitude greater than that for the silicon

pathway. I thus assume that heat transfer through the alternative pathway is negligible. In reality, single-phase and two-phase heat transfer coefficients can be, respectively, 3-4× and ≥ 10× that of our assumed value of 2000 W m^{-2} K^{-1}, further reducing the actual thermal resistance to the fluid.

The heater is assigned a total inward heat flux boundary condition that is set in magnitude by a user specified value. The actual test sections contain 125 channels, or 250 half channels, so this value is simply $1/250^{th}$ of the total heater power input for the case being modeled. The corresponding heat fluxes for the nominal 40°C, 50°C and 60°C experimental cases are 3650 kW m^{-2}, 6975 kW m^{-2} and 9950 kW m^{-2}, respectively. All heat is assumed to go into the silicon with a negligible amount being lost to the environment as per the energy balance described above.

Finally, backside temperature measurements taken with the pyrometer show the temperature at the channel inlet and exit to be identical to the temperatures immediately upstream and downstream of those locations, respectively. This reaffirms the lack of any heat transfer occurring in these regions and justifies the use of adiabatic boundary conditions on the model edges. The remaining faces—the floor and wall—are in contact with the fluid and so are assigned convective boundary conditions. This requires a user specified heat transfer coefficient and a user specified external temperature (fluid temperature). Heat transfer coefficient are defined by various

Table 4-2: Applied boundary conditions.

Geometry	Boundary Condition
Wall & Floor	Convection Correlations Two-phase: Equations 1-11 Single-Phase: Equations 12-13
Base	Heat Input 40°C: 3650 kW m^{-2} 50°C: 6975 kW m^{-2} 60°C: 9950 kW m^{-2}
Remaining	Adiabatic

correlations—the testing of which is the purpose of this work—and fluid temperature is determined via an energy balance. Table 4-2 provides a summary of the boundary conditions used in this work. The following sections present further details for the calculation of both inputs.

4.2 Heat Transfer Coefficient Correlations

The current experimental work has a channel hydraulic diameter of 73.4 μm, a mass flux of 1478 kg m^{-2} s^{-1}, and an applied heat flux of ~10^4 kW m^{-2}. As stated earlier, no published heat transfer coefficient correlations are designed to cover these experimental parameter ranges. However, five well accepted correlations are examined here to determine their ability to predict heat transfer behavior in the current work. These five correlations were chosen from based on an extensive literature search and superior performance (as compared to other gathered correlations) in simplified preliminary modeling efforts that neglected pressure drop. Correlations from Bertsch et al. [21] and Kim and Mudawar [20] were chosen because they were developed using fairly large databases. Correlations from Agostini and Bontemps [72], Lazarek and Black [29] and Warrier et al. [75] were chosen for the relatively high heat flux, relatively high mass flow rate, and use of R134a in rectangular channels, respectively. Each of these correlations will be described in greater

Table 4-3: Summary of modeled correlations.

Source	Parameter Ranges			Number of Consolidated Studies	Fluid Used
	D_h [mm]	G [kg m^{-2} s^{-1}]	q'' [kW m^{-2}]		
Current Work	0.074	1478	3650 - 9950	1	R134a
Agostini and Bontemps [72]	2.01	90 - 295	6 – 31.6	1	R134a
Bertsch et al. [21]	0.16 – 3.63	20 - 3000	4 - 1150	14	Various
Kim and Mudawar [20]	0.349 – 6.0	33 - 1608	Not Given	37	Various
Lazarek and Black [29]	3.15	125 - 750	14 - 380	1	R113
Warrier et al. [75]	0.75	557 – 1600	0 – 59.9	1	FC84

detail in the following subsections, but a brief summary is shown in Table 4-3. Sample calculations for each correlation are detailed in Appendix B.3.

4.2.1 Agostini and Bontemps

Agostini and Bontemps developed a correlation based on experiments performed with vertical flow of R134a in parallel rectangular channels. Mass fluxes ranged from 90 kg m^{-2} s^{-1} to 295 kg m^{-2} s^{-1}, heat fluxes ranged from 6 kW m^{-2} to 31.6 kW m^{-2} and the hydraulic diameter of the channels was 2.01 mm. The authors found dryout incipience to occur at a vapor quality of 43% and accordingly created separate correlations for the pre- and post-dryout incipience regions. These correlations are given in equations (4.20) and (4.21).

$$h = 28q''^{2/3}G^{-0.26}x^{-0.1} \qquad \text{for x < 0.43} \qquad (4.10)$$

$$h = 28q''^{2/3}G^{-0.64}x^{-2.08} \qquad \text{for x > 0.43} \qquad (4.11)$$

4.2.2 Bertsch et al.

The correlation presented by Bertsch et al. [21] was developed from the consolidated data from fourteen separate studies. These studies ranged over twelve fluids and various heat sink materials, geometries and orientations. Details on the individual studies are given in Table 4-4. Hydraulic diameters for the database ranged from 0.16 mm to 3.63 mm, mass fluxes ranged from 20 kg m^{-2} s^{-1} to 3000 kg m^{-2} s^{-1} and heat fluxes ranged from 4 kW m^{-2} to 1150 kW m^{-2}. The correlation is based on the Chen [131] formulation, which consists of both nucleate and convective boiling terms. As quality increases, the contribution of nucleate boiling decreases as the contribution of convective boiling increases. The composite correlation, shown in equations (4.10) through (4.13), is specified to work for saturated flow boiling at all vapor qualities.

$$h = (1-x)h_{nb} + [1 + 80(x^2 - x^6)e^{(-0.6 \cdot Co)}]h_{cb} \qquad (4.12)$$

$$h_{nb} = 55P_R^{(0.12 - log_{10}(R_P))}\left(-log_{10}P_R\right)^{-0.55} M^{-0.5} q''^{0.67} \qquad (4.13)$$

$$h_{cb} = (1-x)h_{conv,l} + xh_{conv,v} \tag{4.14}$$

$$h_{conv,i} = \left(3.66 + \frac{0.0668 \frac{D_h}{L_{ch}} \mathrm{Re}_i \, \mathrm{Pr}_i}{1 + 0.04 \left(\frac{D_h}{L_{ch}} \mathrm{Re}_i \, \mathrm{Pr} \right)^{2/3}} \right) \frac{k_i}{D_h} \tag{4.15}$$

Though originally developed for pool boiling, the Cooper [30] correlation has shown good agreement with pure nucleate boiling in microchannels and so was used as the nucleate boiling term here (equation (4.11)). The Hausen [132] correlation, equation (4.13), created for developing

Table 4-4: Studies used for Bertsch et al. consolidated database [21].

Reference	Notes Fluids, Parallel/Single, Orientation, Geometry, Material	Parameter Ranges			Number of Data Points
		D_h [mm]	G [kg m^{-2} s^{-1}]	q'' [kW m^{-2}]	
Agostini et al. [133]	R134a, parallel, vertical, rectangular, aluminum	0.77 2.01	83 - 467	4.4 – 15	207
Agostini et al. [58,134]	R236fa, R245fa, parallel, horizontal, rectangular	0.34	281 - 1501	7- 420	1392
Bao et al. [48]	R11, R123, single, horizontal, circular, copper	1.95	50 - 1800	5- 200	166
Bertsch et al. [49,135]	R134a, R245fa, parallel, horizontal, rectangular, copper	1.09	20 – 350	50 – 220	332
Chen and Garimella [136]	FC-77, parallel, horizontal, rectangular, copper, silicon	0.39 0.84	63.5 – 440	20 – 800	115
Harirchian and Garimella [137]	FC-77, parallel, horizontal, rectangular, silicon	0.16 - 0.57	250 – 1600	0 – 300	327
Lee and Lee [138]	R113, single, horizontal, rectangular, stainless steel	0.78 – 3.63	50 – 200	0 – 15	553
Lin et al. [139]	H_2O, R141b, single, vertical, circular	1	300 – 2000	10 – 1150	133
Qi et al. [140]	N_2, single, vertical, circular, stainless steel	0.53 – 1.93	440 – 3000	50 – 210	181
Saitoh et al. [66]	R134a, single, horizontal, circular,	0.51 - 3.1	150 – 450	5 – 39	164
Tran et al. [141]	R12, single, horizontal, circular, brass	2.46	89 – 300	7 – 59	62
Wambsganss et al. [46]	R113, single, horizontal, circular, copper	2.92	50 – 300	9 - 91	92
Yan and Lin [64]	R134a, parallel, horizontal, circular, copper	2.0	50 – 200	5 – 20	133
Yun et al. [142]	R410A, parallel, horizontal, rectangular, aluminum	1.36 1.44	200 – 400	10 – 20	101
Total	Various	0.16 – 3.63	20 – 3000	4 - 1150	3899

laminar flows, was chosen to determine the convective heat transfer coefficients for both liquid and vapor phases. The overall convective boiling term was then taken as the weighted average of the individual liquid and vapor values as signified by the vapor quality. Appropriate suppression and enhancement factors—for the nucleate and convective terms, respectively—were determined by fitting the correlation to the database to capture the evolving relative contributions of both heat transfer mechanisms. A surface roughness of one should be assumed if the true value is unknown. The correlation fits their consolidated database with an MAE of 28%.

4.2.3 Kim and Mudawar

Kim and Mudawar [20] developed a correlation based on a very large database of 10,805 data points encompassing thirty-seven different studies with a wide range of fluids and both single and multichannel configurations in various orientations. Hydraulic diameters for the database ranged from 0.349 mm to 6.0 mm and mass fluxes ranged from 33 kg m^{-2} s^{-1} to 1608 kg m^{-2} s^{-1}. Heat fluxes for the studies were not given. Table 4-5 shows the contributions of individual studies used. As with the Bertsch et al. [21] correlation, the two-phase heat transfer coefficient (h_{tp}) consists of both nucleate and convective boiling terms, and can be used for saturated flow boiling at all vapor qualities. The individual terms for this correlation are based on a form suggested by Schrock and Grossman [143]. The correlation is given in Equations (4.14) through (4.16) and fits the consolidated database with an MAE of 20.3%.

$$h_{tp} = (h_{nb}^{\ 2} + h_{cb}^{\ 2})^{1/2} \tag{4.16}$$

$$h_{nb} = \left[2345 \left(Bl P_H / P_F \right)^{0.70} P_R^{\ 0.38} (1-x)^{-0.51} \right] h_{db} \tag{4.17}$$

$$h_{cb} = \left[5.2 \left(Bl P_H / P_F \right)^{0.08} We_l^{-0.54} + 3.5 \left(\frac{1}{X_{tt}} \right)^{0.94} \left(\frac{\rho_v}{\rho_l} \right)^{0.25} \right] h_{db} \tag{4.18}$$

$$h_{db} = \left(0.023\,\mathrm{Re}_{sp}^{4/5}\,\mathrm{Pr}_l^{0.4}\right)\frac{k_l}{D_h} \tag{4.19}$$

$$\mathrm{Re}_{sp} = \frac{G(1-x)}{D_h} \tag{4.20}$$

In the above equations, P_H is the heated perimeter, P_F is the wetted perimeter and X_{tt} is the Martinelli parameter. Note that h_{db} is the Dittus-Boelter heat transfer coefficient utilizing a Reynolds number weighted according to vapor quality.

4.2.4 Lazarek and Black

Lazarek and Black [29] developed a correlation based on vertical flow boiling (both upward and downward flows) experimentation with R113 in circular, stainless steel tubes having a diameter of 3.15 mm. Mass fluxes ranged from 125 kg m^{-2} s^{-1} to 750 kg m^{-2} s^{-1}, heat fluxes ranged from 14 kW m^{-2} to 380 kW m^{-2} and qualities ranged up to those values when critical heat flux was experienced. The correlation was determined using a least-squares fit technique to match the collected data. The majority of the authors' 728 data points fall within ±15% (with and RMS error of 9%) of the correlation prediction.

$$Nu = 30\,\mathrm{Re}_l^{0.857}\,Bl^{0.714} \tag{4.21}$$

4.2.5 Warrier et al.

The Warrier et al. [75] correlation is based on data from flow boiling of FC-84 in parallel, horizontal, rectangular channels with a hydraulic diameter of 0.75 mm. Mass fluxes ranged from 557 kg m^{-2} s^{-1} to 1600 kg m^{-2} s^{-1} and heat fluxes ranged from 0 kW m^{-2} up to 59.9 kW m^{-2} and vapor qualities ranged from 0.03 to 0.55. The correlation, shown below in equations (4.18) and (4.19), predicted all the data within ±28%, however the authors caution that it is valid only over the specified narrow parameter ranges.

$$\frac{h_{tp}}{h_{sp,fd}} = 1 + 6.0Bl^{1/16} - 5.3\left(1 - 855Bl\right)x^{0.65} \tag{4.22}$$

$$h_{sp,fd} = .00805\,\mathrm{Re}^{0.8}\,\mathrm{Pr}^{0.4} \tag{4.23}$$

Table 4-5: Individual studies compiled for the Kim and Mudawar [20] consolidated database.

Reference	Notes (Fluids, Parallel/Single, Geometry, Material)	D_h [mm]	G [kg m^{-2} s^{-1}]	# of Data Points
Wambsganss et al. [46]	R113a, single, circular, stainless steel	2.92	50 – 300	76
Tran [47]	R134a, single, circular, brass	2.46	33 – 502	302
Wang et al. [67]	R22, single, circular, copper	6.5	100 – 400	61
Yan and Lin [144]	R134a, parallel, circular, copper	2.0	50 – 200	116
Bao et al. [48]	R11, R123, single, circular, copper	1.95	167 – 560	143
Qu and Mudawar [61]	Water, parallel, rectangular, copper	0.349	135 – 402	335
Sumith et al. [60]	Water, single, circular, stainless steel	1.45	23 – 153	85
Yun et al. [56]	R134a, CO_2, single, circular, stainless steel	6.0	170 – 340	169
Huo et al. [55]	R134a, single, circular, stainless steel	2.01, 4.26	100 – 500	323
Lee and Mudawar [65]	R134a, parallel, rectangular, copper	0.349	61 – 657	63
Saitoh et al. [66]	R134a, single, circular, stainless steel	0.51, 1.12, 3.1	150 – 300	259
Yun et al. [57]	CO_2, parallel, rectangular, stainless steel	1.14, 1.53, 1.54	200 – 400	43
Muwanga and Hassan [145]	FC72, single, circular, stainless steel	1.067	770 – 1040	327
Zhao and Bansal [146]	CO_2, single, circular, stainless steel	4.57	140 – 231	19
Agostini et al. [134]	R236fa, parallel, rectangular, silicon	0.336	281 – 1370	458
Consolini [147]	R134a, R236fa, R245fa, single, circular, stainless steel	0.51, 0.79	274 – 1435	585
Greco [68]	R134a, R22, R404A, R407C, R410A, R417A, single, circular, stainless steel	6.0	199 – 1100	491
Bertsch et al. [49]	R134a, R245fa, parallel, rectangular, copper	0.544, 1.089	19 – 336	214
In and Jeong [69]	R123, R134a, single, circular, stainless steel	0.19	314 – 470	1159
Mastrullo et al. [59]	CO_2, single, circular, stainless steel	6.0	200 – 349	135
Ohta et al. [148]	FC72, single, circular, stainless steel	0.51	107 - 215	13
Wang et al. [50]	R134a, single, circular, stainless steel	1.3	321 – 836	322
Ducoulombier [149]	CO_2, single, circular, stainless steel	0.529	200 - 1400	1080
Hamdar et al. [51]	R152a, single, rectangular, aluminum	1.0	210 – 580	45
Martín-Callizo [150]	R134a, R22, single, circular, stainless steel	0.64	185 – 535	335
Ong [151]	R134a, R236fa, R245fa, single, circular, stainless steel	1.03, 2.2, 3.04	199 - 1608	2247
Tibiriçá and Ribatski [152]	R134a, R245fa, single, circular, stainless steel	2.32	50 – 700	96
Ali et al. [54]	R134a, single, circular, stainless steel	1.7	75 – 600	136
Bang et al. [63]	Water, single, circular, stainless steel	1.73	100	65
Copetti et al. [153]	R134a, single, circular, stainless steel	2.62	240 – 932	845
Mahmoud et al. [52]	R134a, single, circular, stainless steel	1.1	128 – 549	134
Oh and Son [62]	R134a, R22, single, circular, copper	1.77, 3.36, 5.35	200 – 500	131
Oh and Son [154]	CO_2, single, circular, stainless steel	4.57	400 – 900	62
Wu et al. [70]	CO_2, single, circular, stainless steel	1.42	300 – 600	297
Karayiannis et al. [53]	R134a, single, circular, stainless steel	1.1	215 – 550	489
Li et al. [155]	R1234yf, R32, single, circular, stainless steel	2.0	100 – 400	134
Tibiriçá et al. [71]	R1234ze, single, circular, stainless steel	1.0, 2.2	300 – 600	11
Total	Various	0.349 – 6.0	33 - 1608	10,805

4.2.6 Kim and Mudawar Single-phase

Fluid enters the channels as a subcooled liquid, creating a region of single-phase heat transfer before saturation conditions are met. The single-phase relation suggested by Kim and Mudawar [156] for thermally developed laminar flow is used for all models. This correlation is a relation from Copeland [157] that has been fit to data from Shah and London [158].

$$Nu = \left\{ \left[1.54 \left(\frac{L_{sp}}{\mathrm{Re_l}\,\mathrm{Pr_l}\,D_h} \right)^{-0.33} \right]^4 + Nu_3^{\,4} \right\}^{1/4} \tag{4.24}$$

$$Nu_3 = 8.235\left(1 - 1.833\beta + 3.767\beta^2 - 5.814\beta^3 + 5.361\beta^4 - 2.0\beta^5\right) \tag{4.25}$$

This correlation was chosen for the current study, although the choice of which correlation to use is a relatively minor one as the two-phase heat transfer coefficients are roughly an order of magnitude greater than the single-phase heat transfer coefficients.

4.3 Local Fluid State

The thermodynamic state of a fluid is specified by determination of two independent properties. For a single-phase fluid two such properties are temperature and pressure and these properties are used in the current work. In a two-phase fluid these two properties are no longer independent. Thus, a third property, vapor quality, is used. Though these properties are intricately related, for ease of explanation and calculation, they are determined separately, and so will be discussed separately. Subsection 4.3.1 will describe how the fluid temperature and quality are calculated and assumes that the local fluid pressure is already known. Similarly, Subsection 4.3.2 assumes that the local fluid temperature and local quality are known and describes the calculation of the fluid pressure. This approach is made possible through the use of an iterative solution method which is described in detail in Section 4.5.

4.3.1 Temperature Calculation

All temperature and heat transfer calculations are performed in COMSOL, which automatically calculates all relevant heat transfer variables for the modeled solid geometry. These include temperature and directional heat flux for every element in the model. However, as the fluid is not modeled in the current work, the fluid temperature must be calculated via user defined equations. Mean fluid temperature calculations are performed in the *Fluid Properties* and *Temperature Calculations* variable nodes. The basic method will be outlined here while the details may be found in Appendix B.2.

Fluid temperature is calculated as a function of location in the flow direction (y-direction). Fluid enters the channels as a slightly subcooled liquid (at y = 0 mm) and begins to absorb heat from the channel walls and floor through convection. In this single-phase region the heat raises the temperature of the fluid (T_{fluid}) in accordance with the following equation:

$$T_{\text{fluid}}(y) = T_{\text{in}} + \frac{\dot{Q}(y)}{\dot{m}C_{\text{p}}} \tag{4.26}$$

where $\dot{Q}$ represents the total heat transfer rate up to the given y-location. The total heat transfer rate is calculated by integrating the total heat flux along the channel wall and floor up to the location in question. As an example, I examine the 60°C model employing the Kim and Mudawar two-phase heat transfer correlation. Input parameters for this model are shown in Table 4-6. For this model, the amount of heat absorbed by the fluid at a location 1 mm downstream of the channel inlet is 0.023 W. For the inlet temperature of 11.5°C, the mass flow rate of 6.67×10^{-6} kg s^{-1} and an average specific heat of 1395 J kg^{-1} K^{-1} I find the fluid temperature at this location as follows:

$$T_{\text{fluid}}(1\text{ mm}) = 11.5\ ^{\circ}\text{C} + \frac{0.023\ \text{W}}{\left(6.67\times10-6\ \frac{\text{kg}}{\text{s}}\right)\left(1395\ \frac{\text{J}}{\text{kg}\cdot\text{K}}\right)} = 14.0\ ^{\circ}\text{C} \tag{4.27}$$

Table 4-6: Inputs for Kim and Mudawar 60°C model.

	Units	Value
Inlet Fluid Temperature	[°C]	11.5
Inlet Fluid Pressure	[kPa]	595.1
Mass Flow Rate	[g s^{-1}]	6.67×10^{-6}
Total Applied Power	[W]	0.397

As the liquid temperature continues to rise, so does the associated saturation pressure. Meanwhile, the actual fluid pressure is decreasing due to frictional and accelerational losses. Once the actual pressure and the saturation pressure match, additional heat begins to transform liquid into vapor. At this point, the fluid temperature need no longer be calculated as it will always be equal to the saturation temperature corresponding to the pre-defined pressure distribution. Instead, vapor quality must be tracked.

Vapor quality increases both due to continued heat absorption and the dropping fluid pressure. It is calculated by keeping track of enthalpies and performing an energy balance. The enthalpy of the coolant (i_{fluid}) increases as heat is absorbed and can be calculated according to the following equation:

$$i_{\text{fluid}}(y) = i_{\text{in}} + \frac{\dot{Q}(y)}{\dot{m}} \tag{4.28}$$

As with temperature, enthalpy is calculated as function of y-location and is a mean value. Vapor quality is related to this mean enthalpy according to Equation (4.27). Since all properties are functions of y-location, for clarity's sake this dependence will no longer be explicitly shown.

$$i_{\text{fluid}} = (1-x)i_{\text{l}} + xi_{\text{v}} \tag{4.29}$$

It should be noted that because fluid temperature is a function of y-location, so too are the liquid and vapor enthalpies. With both the fluid enthalpy and the individual phase enthalpies known, Equation (4.27) can be rearranged to solve for vapor quality as shown in Equation (4.28).

$$x = \frac{i_{\text{fluid}} - i_{\text{l}}}{i_{\text{v}} - i_{\text{l}}} \tag{4.30}$$

Returning to our example case, I can calculate the exit vapor quality. For a temperature of 11.5°C and a pressure of 595.9 kPa, the inlet fluid enthalpy is 67.5 kJ kg^{-1}. Using Equation (4.26) , I find that the fluid enthalpy at the channel exit is as follows:

$$i_{\text{fluid}}\left(5\text{ mm}\right) = 67.5\ \frac{\text{kJ}}{\text{kg}} + \frac{0.397\text{ W}}{6.67\times10^{-6}\ \text{kg/s}} = 127.0\ \frac{\text{kJ}}{\text{kg}} \tag{4.31}$$

The exit pressure for this case was 530.7 kPa, corresponding to a fluid temperature of 17.6°C. At this temperature, the values of liquid and vapor enthalpies are 76.0 kJ kg^{-1} and 260.3 kJ kg^{-1}, respectively. I can now find vapor quality using Equation (4.28) as follows:

$$x\left(5\text{ mm}\right) = \frac{127.0\ \text{kJ/kg} - 76.0\ \text{kJ/kg}}{260.3\ \text{kJ/kg} - 76.0\ \text{kJ/kg}} = 0.277 \tag{4.32}$$

4.3.2 Pressure Calculation

All pressure drop calculations were performed in MATLAB. This was necessary due to issues with circularity preventing implementation in COMSOL. The MATLAB calculations begin once the COMSOL model has solved. Utilizing COMSOL LiveLink for MATLAB, a custom designed MATLAB script was written to extract necessary information from COMSOL and to then perform the requisite pressure drop calculations to obtain a pressure distribution for the model. Pressure drop is calculated differently in the single-phase and two-phase regions. Similar to heat transfer correlations, no pressure drop correlations have been designed to cover the very small channel sizes (D_{h}=73.4 μm) involved in this study. Instead, two well-accepted correlations

presented by Lee and Garimella [159] that were developed with hydraulic diameters as small as 159.7 μm were used. The single-phase correlation is shown in Equation (4.31).

$$\Delta P_{sp} = \frac{1}{2} G^2 v_l f_{sp} L_{sp} \tag{4.33}$$

where L_{sp} is the length of the single-phase region, and the single-phase friction factor (f_{sp}) is calculated as suggested by Shah and London [160]:

$$f_{sp} = \frac{96}{\mathrm{Re}_l}\left(1 - 1.3553\beta + 1.9467\beta^2 - 1.7012\beta^3 + 0.9564\beta^4 - 0.2537\beta^5\right) \tag{4.34}$$

The two-phase correlation is shown in Equations (4.33)-(4.37):

$$\Delta P_{tp} = \Delta P_{tp,f} + \Delta P_{tp,a} \tag{4.35}$$

$$\frac{\Delta P_{tp,f}}{L_{sp}} = \frac{1}{x}\int_0^x 2\phi^2 f G^2 \frac{(1-x)^2}{\rho_l D_h} dx \tag{4.36}$$

$$\phi = \sqrt{1 + \frac{C}{X_{vv}} + \frac{1}{X_{vv}^2}} \tag{4.37}$$

$$C = 2566 \cdot G^{0.5466} D_h^{0.8819} \left(1 - e^{-319 D_h}\right) \tag{4.38}$$

$$\Delta P_{tp,a} = \frac{G^2}{\rho_l}\left[\frac{x^2}{\alpha_o\left(\rho_l / \rho_v\right)} + \frac{(1-x)^2}{1-\alpha_o} - 1\right] \tag{4.39}$$

where X_{vv} is the laminar liquid-laminar vapor Lockhart-Martinelli parameter as given by Equation (4.38) and α_o is the Zivi [78] void fraction as given by Equation (4.39).

$$X_{vv} = \left(\frac{\mu_l}{\mu_v}\right)^{1/2}\left(\frac{1-x}{x}\right)^{1/2}\left(\frac{\rho_v}{\rho_l}\right)^{1/2} \tag{4.40}$$

$$\alpha_o = \left[1 + \left(\frac{1-x}{x}\right)\left(\frac{\rho_l}{\rho_v}\right)^{2/3}\right] \tag{4.41}$$

To determine the local pressure distribution, the channel was divided into 100 equal length segments and the pressure drop across each one was calculated. With the channel inlet pressure

(P_{in}) known (this will be discussed momentarily), the pressure at any given segment endpoint '*i*' within the single-phase region is then

$$P_i = P_{in} - \sum_0^i \Delta P_i \tag{4.42}$$

The Lee and Garimella [159] pressure drop correlations have been developed to calculate the overall pressure drop through the entire channel, so several modifications are necessary in order to calculate individual segment pressure drops. For the single-phase region, Equation (4.31) was used with L_{sp} replaced by the length of a segment (50 μm). Viscosity and Reynolds number values are taken to be averages across each individual segment. As described in Section 2.1.4, two-phase pressure drop is a combination of frictional and accelerational components. The accelerational component given in Equation (4.37) can be calculated for each segment as given, but the frictional component in Equation (4.34) must be adjusted. The two-phase frictional pressure for any segment '*j*' is calculated as follows:

$$\Delta P_{tp,f,j} = 2\phi_j^2 f_j G^2 \frac{(1-x_j)^2}{\rho_{l,j} D_{h,j}} L_{segment} \tag{4.43}$$

Combining this with Equation (4.40), the pressure at the end of any given segment '*j*' within the two-phase region can be calculated as follows:

$$P_j = P_{in} + \sum_0^i \Delta P_i + \sum_i^j \Delta P_j \tag{4.44}$$

This results in 101 locations of known pressure along the 5 mm channel length. This pressure distribution is saved to a file read by COMSOL. Values in between the locations of known pressure are determined in COMSOL using a linear interpolation. Use of Equation (4.42) requires a knowledge of the inlet pressure. It was assumed above that this value is known, but in reality, it must be determined. The method for determination of this channel inlet pressure is described in the following subsection.

4.3.3 Channel Inlet Pressure

As with temperature, the inlet fluid pressure measurement made during experimentation occurs upstream of the test section. While temperature change between the measurement location and the channel inlet is negligible, a significant amount of pressure drop occurs in this region. This is due to the complex geometry of the test section as well as the orifice inlet restriction. At first glance this would seem to be an excellent problem for CFD simulations; however, due to the manufacturing method of the test sections, this proved untenable.

As discussed in Section 3.1, the Bosch etching process used to fabricate the test section results in different etch rates for features with different widths. Wider features etch faster than narrower features due to greater accessibility to the reactive ions. While etch depth is very uniform in the interior of a feature, the depth profile in regions of transition between features of different widths—such as between the inlet manifold and orifice, and between the orifice and the channel inlet—is not well defined. Visual measurements of this depth profile could be made via destructive measurement techniques, but cost and difficulty rendered impractical the collection of a sufficient number of measurements to arrive with any confidence at an accepted profile. Initial CFD work based on estimated depth profiles for the orifice region resulted in pressure drops ranging from ~45 kPa to ~140 kPa for a given mass flow rate of 100 g min^{-1}. As total pressure drops during testing ranged from 86 kPa to 201 kPa, this degree of uncertainty was unacceptable. Ultimately, it was decided that a correlational method would be used instead.

During experimentation, single-phase data was collected for the same nominal inlet conditions present during two-phase testing. A slight amount of heat was added through the heater to bring the fluid just up to the saturation point at the test section exit. Since more experimental data was collected than is modeled here, three single-phase datasets were examined with mass

flow rates between 99.3 g min^{-1} and 100.5 g min^{-1}, inlet temperatures between 11.1°C and 19.3°C and outlet temperatures between 13.0°C and 19.7°C. These data provided the total single-phase pressure drop across the test section for the given inlet conditions. Appropriate correlations were then used to model the pressure drop through all regions of known geometry—everything except the orifice.

For convenience, the orifice will be considered the dividing feature with all calculated pressure drops occurring either upstream or downstream of this feature. The total pressure drop is then the sum of the individual drops upstream (ΔP_{up}), downstream (ΔP_{down}) and through the orifice (ΔP_{ori}). The pressure drop through the orifice can be obtained by subtracting the amount of upstream and downstream pressure losses from the total pressure drop (ΔP_{tot}):

$$\Delta P_{tot} = \Delta P_{up} + \Delta P_{ori} + \Delta P_{down} \tag{4.45}$$

$$\Delta P_{ori} = \Delta P_{tot} - \Delta P_{up} - \Delta P_{down} \tag{4.46}$$

Each of the steps involved in the upstream and downstream loss calculation will be examined in detail.

Figure 4-8 shows the fluid path between the upstream and downstream pressure sensors and labels different locations referenced in the following description of pressure drop calculations. An uncertainty of ±50% was assumed for all correlational calculations. Necessary fluid properties were taken to be at average fluid temperature and pressure for the dataset being modeled, an assumption which introduces an error of less than 0.5%, a negligible amount compared to the uncertainty.

The total single-phase pressure drop consists of both frictional and minor losses, as shown below:

$$\Delta P_{tot} = \sum \Delta P_{f,i} + \sum \Delta P_{min,i} \tag{4.47}$$

Frictional pressure loss for a given segment '*i*' is calculated as follows:

$$\Delta P_{f,i} = \frac{1}{2}\rho u_i^2 f_i \frac{L_i}{D_{h,i}} \tag{4.48}$$

The majority of the fluid flow through the system is in the transitional and turbulent regimes, so the Churchill [161] friction factor, which covers all flow regimes, is used:

$$f_i = \left[\left(\frac{8}{\mathrm{Re}_i}\right)^{12} + \frac{1}{(A_i + B_i)^{3/2}}\right]^{1/12} \tag{4.49}$$

$$A_i = \left[2.457 \ln\left(\frac{1}{\left(\left(7/\mathrm{Re}_i\right)^{0.9} + 0.27\,\varepsilon_i/D_{h,i}\right)}\right)\right]^{16} \tag{4.50}$$

$$B_i = \left(\frac{37530}{\mathrm{Re}_i}\right)^{16} \tag{4.51}$$

The surface roughness (ε) in Equation (4.48) is assumed to be zero if the actual value is unknown. The Shah and London friction factor, given in Equation (4.32), was designed specifically for laminar flow in rectangular ducts and is used for the pressure drop through the channels in place of the Churchill friction factor. Minor losses were calculated as shown in

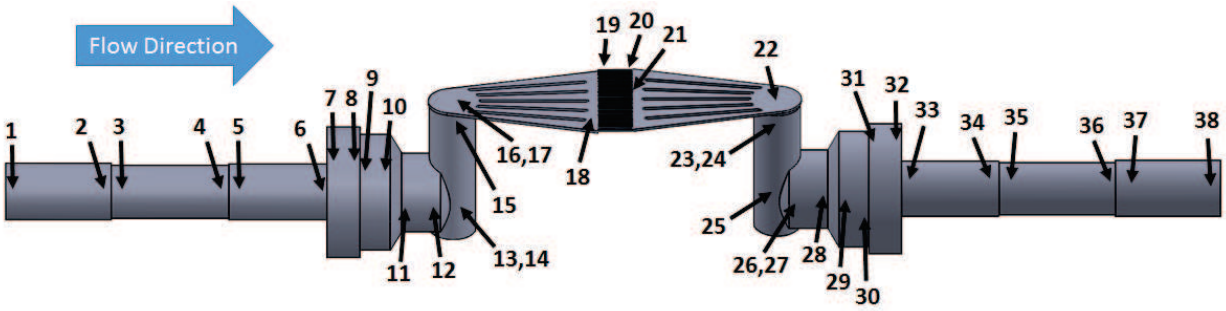

Figure 4-8: Test facility fluid flow path with locations of pressure drop calculations marked.

Table 4-7: Equations for minor loss coefficients.

Minor Loss		Coefficient Equation
Contraction* [162]	Gradual (≤45°)	$0.8\sin\frac{\theta}{2}\left(1-\frac{d_1^2}{d_2^2}\right)$
	Sudden	$0.5\left(1-\frac{d_1^2}{d_2^2}\right)$
Expansion* [162]	Gradual	$2.6\sin\frac{\theta}{2}\left(1-\frac{d_1^2}{d_2^2}\right)^2$
	Sudden	$\left(1-\frac{d_1^2}{d_2^2}\right)^2$
90° Bend** [163]		$60F_s$
* $d_1 < d_2$ **F_S = empirically obtained friction factor		

Equation (4.50) with minor loss coefficients (K_{min}) calculated in EES using the equations given in Table 4-7.

$$\Delta P_{\text{min,i}} = \frac{1}{2}\rho u_{\text{i}}^2 K_{\text{min,i}} \tag{4.52}$$

Note that, given two options, the maximum velocity should always be used in the above equation.

For this analysis, the fittings were modeled as a cylindrical pipe and associated frictional losses were calculated. Transitions where tubing joined a fitting were modeled as sudden expansions and contractions. Frictional losses were also calculated through all straight sections of tubing. Geometries become more complicated inside the PEEK interface block and test section. Several assumptions were necessary in order to model these regions, but essentially pressure loss through the PEEK and test section are modeled as a series of frictional losses and minor losses due to contractions, expansions and 90° bends.

The vast majority of the single-phase pressure drop occurs within the test section itself. In fact, the total pressure drop through the tubing leading up to, and away from the test section, locations 1-15 and 24-38 respectively, accounts for less than 0.05% of the total pressure drop for

Table 4-8: Fluid conditions for sample calculations.

		Units	Value
Fluid Temperature	Inlet/Outlet	[°C]	14.5/15.7
	Average	[°C]	15.1
Fluid Pressure	Inlet/Outlet	[kPa]	623.1/571.0
	Average	[kPa]	597.1
Density		[kg m^{-3}]	1244
Viscosity		[kg m^{-1} s^{-1}]	2.20×10^{-4}
Mass Flow Rate		[kg s^{-1}]	1.68×10^{-3}

the flow rates examined in this work. Though the assumptions made in calculating pressure drop through these regions is therefore relatively insignificant, in the interest of being thorough, the entire process will now be described starting at the pressure tap at location 1.

As an example of the of the method, I examine a sample case with the flow parameters shown in Table 4-8. Diameter values are taken from a combination of product specification sheets and actual measurements. The tube between locations 1 and 2 has an inner diameter of 4.75 mm and a length of 11.68 mm. The fluid velocity and Reynolds number are calculated as follows:

$$u_{1\to 2} = \frac{\dot{m}}{\rho A} = \frac{4\dot{m}}{\pi\rho D^2} = \frac{4\left(1.675\times10^{-3}\,\frac{\text{kg}}{\text{s}}\right)}{\pi\left(1244\,\frac{\text{kg}}{\text{m}^3}\right)\left(4.75\times10^{-3}\,\text{m}\right)^2} = 7.60\times10^{-2}\,\frac{\text{m}}{\text{s}} \tag{4.53}$$

$$\text{Re}_{1\to 2} = \frac{\rho u_{1\to 2} D_{1\to 2}}{\mu} = \frac{\left(1244\,\frac{\text{kg}}{\text{m}^3}\right)\left(7.60\times10^{-2}\,\frac{\text{m}}{\text{s}}\right)\left(4.75\times10^{-3}\,\text{m}\right)}{2.20\times10^{-4}\,\frac{\text{kg}}{\text{m}\cdot\text{s}}} \approx 2040 \tag{4.54}$$

Calculating the Churchill friction factor in Equations (4.47)-(4.49) (assuming ε=0) gives

$$A_{1\to 2} = \left[2.457\ln\left(\frac{1}{\left(\left(7/2040\right)^{0.9}\right)}\right)\right]^{16} = 3.781\times10^{17} \tag{4.55}$$

$$B_{1\to 2} = \left(\frac{37530}{2154}\right)^{16} = 1.722\times 10^{20} \tag{4.56}$$

$$f_{1\to 2} = \left[\left(\frac{8}{2040}\right)^{12} + \frac{1}{\left(3.781\times 10^{17} + 1.722\times 10^{20}\right)^{3/2}}\right]^{1/12} = .00393 \tag{4.57}$$

The frictional pressure drop through this region is then

$$\Delta P_{f,1\to 2} = \frac{1}{2}\left(1244\frac{\text{kg}}{\text{m}^3}\right)\left(7.60\times 10^{-2}\,\frac{\text{m}}{\text{s}}\right)^2 (.00393)\left(\frac{1.168\times 10^{-2}\,\text{m}}{4.75\times 10^{-3}\,\text{m}}\right) = 0.035\ \text{Pa} \tag{4.58}$$

The sudden contraction between locations 2 and 3 is a minor loss calculated according to Equation (4.50). The diameter decreases from 4.75 mm to 4.50 mm, giving a minor loss coefficient of 0.052 as calculated per Table 4-7. The maximum fluid velocity is:

$$u_{2\to 3} = \frac{4\dot{m}}{\pi\rho D^2} = \frac{4\left(1.675\times 10^{-3}\,\frac{\text{kg}}{\text{s}}\right)}{\pi\left(1244\frac{\text{kg}}{\text{m}^3}\right)\left(4.50\times 10^{-3}\,\text{m}\right)^2} = 8.47\times 10^{-2}\,\frac{\text{m}}{\text{s}} \tag{4.59}$$

and the minor pressure loss is then:

$$\Delta P_{2\to 3} = \frac{1}{2}\left(1244\frac{\text{kg}}{\text{m}^3}\right)\left(8.47\times 10^{-2}\,\frac{\text{m}}{\text{s}}\right)^2 (0.052) = 0.229\ \text{Pa} \tag{4.60}$$

Pressures losses are calculated in the same manner as above between subsequent locations as follows: frictional, 3-4; sudden expansion, 4-5, frictional, 5-6; sudden expansion, 6-7; frictional 7-8; sudden contraction, 8-9; frictional, 9-10; gradual contraction, 10-11; and frictional, 11-12. The complicated geometry between locations 12 and 14 requires special consideration as the fluid undergoes a simultaneous sudden contraction and 90° bend. I superimpose these two minor losses to determine the total loss, however, the order of superposition is important. The velocity changes during the contraction, and because the 90° bend minor loss depends heavily on velocity, the calculated value for this loss will depend on whether it is considered as coming before or after the contraction. This is shown in the following:

90° bend prior to contraction (D=6.76 mm, K=1.285)

$$u = \frac{4\dot{m}}{\pi\rho D^2} = \frac{4\left(1.675\times10^{-3}\,\frac{\text{kg}}{\text{s}}\right)}{\pi\left(1244\,\frac{\text{kg}}{\text{m}^3}\right)\left(6.76\times10^{-3}\,\text{m}\right)^2} = 3.76\times10^{-2}\,\frac{\text{m}}{\text{s}} \tag{4.61}$$

$$\Delta P_{\min} = \frac{1}{2}\left(1244\,\frac{\text{kg}}{\text{m}^3}\right)\left(3.76\times10^{-2}\,\frac{\text{m}}{\text{s}}\right)^2\left(1.285\right) = 1.13\text{ Pa} \tag{4.62}$$

90° bend after contraction (D=4.00 mm, K=1.285)

$$u = \frac{4\dot{m}}{\pi\rho D^2} = \frac{4\left(1.675\times10^{-3}\,\frac{\text{kg}}{\text{s}}\right)}{\pi\left(1244\,\frac{\text{kg}}{\text{m}^3}\right)\left(4.00\times10^{-3}\,\text{m}\right)^2} = 1.07\times10^{-1}\,\frac{\text{m}}{\text{s}} \tag{4.63}$$

$$\Delta P_{\min} = \frac{1}{2}\left(1244\,\frac{\text{kg}}{\text{m}^3}\right)\left(1.07\times10^{-1}\,\frac{\text{m}}{\text{s}}\right)^2\left(1.285\right) = 9.15\text{ Pa} \tag{4.64}$$

To account for this, the average value is used, which in this case is 5.14 Pa. A frictional loss occurs between locations 14 and 15 before another simultaneous 90° bend and contraction occur between locations 15 and 17. This time the fluid moves from a circular tube to a rectangular one. The same method employed earlier is used here with the exception that the rectangular area is calculated differently. As this is a much more pronounced contraction, the difference between calculating the 90° bend as occurring before or after the contraction is much more extreme:

90° bend prior to contraction (Circular, D=4.00 mm, K=1.285)

$$u = \frac{4\dot{m}}{\pi\rho D^2} = \frac{4\left(1.675\times10^{-3}\,\frac{\text{kg}}{\text{s}}\right)}{\pi\left(1244\,\frac{\text{kg}}{\text{m}^3}\right)\left(4.00\times10^{-3}\,\text{m}\right)^2} = 1.07\times10^{-2}\,\frac{\text{m}}{\text{s}} \tag{4.65}$$

$$\Delta P_{\min} = \frac{1}{2}\left(1244\,\frac{\text{kg}}{\text{m}^3}\right)\left(1.07\times10^{-1}\,\frac{\text{m}}{\text{s}}\right)^2\left(1.285\right) = 9.15\text{ Pa} \tag{4.66}$$

90° bend after contraction (Rectangular, W=4.00 mm, H= 230 μm, K=1.285)

$$u = \frac{\dot{m}}{\rho A} = \frac{1.675\times10^{-3}\,\frac{\text{kg}}{\text{s}}}{\left(1244\,\frac{\text{kg}}{\text{m}^3}\right)\left(2.30\times10^{-4}\,\text{m}\right)\left(4.00\times10^{-3}\,\text{m}\right)} = 1.46\,\frac{\text{m}}{\text{s}} \tag{4.67}$$

Table 4-9: Average parameters for manifold frictional pressure drop calculation.

	Units	Value
Width	[mm]	5.46
Length	[mm]	12.81
Hydraulic Diameter	[μm]	440
Velocity	[m s^{-1}]	1.17
Reynolds Number	[-]	2898

$$\Delta P_{\min} = \frac{1}{2}\left(1244\frac{\text{kg}}{\text{m}^3}\right)\left(1.46\frac{\text{m}}{\text{s}}\right)^2(1.285) = 1712.86 \text{ Pa} \tag{4.68}$$

The average value in this case is 861.01 Pa.

The inlet manifold, between locations 17 and 18, is also somewhat complicated. A gradual expansion does occur, but correlational calculations show that the expansion is so slight/gradual as to have a negligible impact on pressure loss. Instead, I calculate a frictional pressure loss through this region calculated. This is accomplished by calculating average widths and lengths and converting the geometry to that of a straight section of rectangular duct, as shown in Figure 4-9.

Figure 4-9a shows the original geometry with five individual ribs. This is first converted into the geometry of Figure 4-9b which has a single combined rib. As can be seen, the five individual ribs each have different lengths and are located different distances away from the orifice at location 18. The single, consolidated rib has the total width and average length of the individual ribs and is separated from the orifice at location 18 by an average distance. Figure 4-9c shows that an average length for each individual rib needs to be calculated before an average across all the ribs is taken. The geometry in Figure 4-9b is then converted to the straight, rib-less duct of Figure 4-9d. The average fluid path width and length are calculated as integral averages and applied as the width and length of the straight duct. The frictional loss is then calculated as other frictional

losses, using the Churchill friction factor because flow through the region is turbulent. Integral averaged distances and fluid parameters are given in Table 4-9 for the sample case, yielding a frictional pressure loss of 131.4 Pa.

The goal of this entire procedure is to determine the pressure loss in the orifice, between locations 18 and 19, so this region is skipped in these calculations. The pressure drop through the channels, between locations 19 and 20, is calculated using Equation (4.46), as before, but in this case the flow is highly laminar, with a Reynolds number for the sample case of 497. As such, the friction factor suggested by Shah and London in Equation (4.32) for laminar flow through rectangular ducts is appropriate. The aspect ratio (β) of the channels is 4.44 and the fluid velocity through the channels is 1.20 m s^{-1} giving a friction factor of 0.15 and pressure drop of 9,006 Pa.

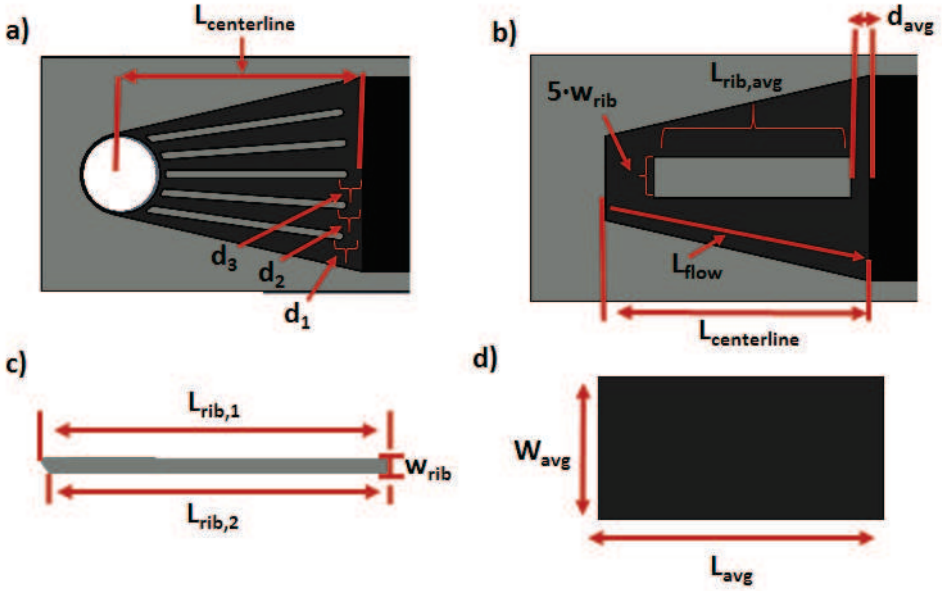

Figure 4-9: Sequential steps for converting inlet/outlet manifolds to straight, rectangular ducts.

Jetting occurs at the channel exit, between locations 20 and 21. To determine pressure loss here, a single channel is examined and the fluid from that channel is assumed to suddenly expand from an area defined by the channel height and width (200 µm × 45µm) to an area defined by the height of the outlet manifold (230 µm) and the width of a combined channel and fin (80 µm). For

the sample case with a maximum fluid velocity of 1.20 m s^{-1} and a minor loss coefficient of 0.381, the pressure loss due to jetting is

$$\Delta P_{\min} = \frac{1}{2}\left(1244\frac{\text{kg}}{\text{m}^3}\right)\left(1.20\frac{\text{m}}{\text{s}}\right)^2(0.381) = 339.3 \text{ Pa} \tag{4.69}$$

The geometry between locations 21 and 38 on the outlet side of the channels is a mirror image of that between locations 1 and 17 on the inlet side of the channels. The only difference from a pressure drop standpoint is that fluid flows in the opposite direction through the geometry. As such, contractions on the inlet side become expansions on the outlet side and vice versa. The pressure drops between the remaining locations are calculated as follows: frictional, 21-22; simultaneous 90° bend and sudden expansion, 22-24; frictional, 24-25; simultaneous 90° bend and sudden expansion, 25-27; frictional, 27-28; gradual expansion, 28-29; frictional, 29-30; sudden expansion, 30-31; frictional, 31-32; sudden contraction, 32-33; frictional, 33-34; sudden contraction, 34-35; frictional, 35-36, sudden expansion, 36-37; and frictional, 37-38.

A summary of the types of losses calculated between each location, along with the values obtained for the sample case, is given in Table 4-10. The total pressure drop upstream and downstream of the orifice is

$$\Delta P_{\text{tot}} = \Delta P_{\text{up}} + \Delta P_{\text{down}} = 1.66 \text{ kPa} + 11.65 \text{ kPa} = 13.31 \text{ kPa} \tag{4.70}$$

The total uncertainty is calculated by combining the uncertainties for each calculation (assumed to be ±50%) as follows:

$$\delta P_{\text{tot}} = \sqrt{\delta P_{1,2}{}^2 + \delta P_{1,2}{}^2 + \ldots + \delta P_{17,18}{}^2 + \delta P_{19,20}{}^2 + \delta P_{21,22}{}^2 \ldots + \delta P_{37,38}{}^2} \tag{4.71}$$

which gives an uncertainty of ± 4.60 kPa for the sample case. Returning to Equation (4.44), the pressure drop through the orifice can now be calculated. For the sample case with a total measured pressure drop of 52.06 ± 0.05 kPa, the orifice pressure drop is

$$\Delta P_{\text{ori}} = (52.06 \pm 0.05 \text{ kPa}) - (13.31 \pm 4.60 \text{ kPa}) = 38.75 \pm 4.60 \text{ kPa} \tag{4.72}$$

Table 4-10: Pressure drop results for sample case.

Location	Description	Pressure Drop (Pa)	Location	Description	Pressure Drop (Pa)
1-2	Frictional Loss	<0.1	19-20	Frictional Loss	9,006.0
2-3	Sudden Contraction	0.2	20-21	Sudden Expansion	339.3
3-4	Frictional Loss	0.2	21-22	Frictional Loss	131.4
4-5	Sudden Expansion	<0.1	22-23	90° Bend	861.0
5-6	Frictional Loss	<0.1	23-24	Sudden Expansion	1,301.0
6-7	Sudden Expansion	2.4	24-25	Frictional Loss	<0.1
7-8	Frictional Loss	<0.1	25-26	90° Bend	5.2
8-9	Sudden Contraction	<0.1	26-27	Sudden Expansion	3.0
9-10	Frictional Loss	<0.1	27-28	Frictional Loss	<0.1
10-11	Gradual Contraction	0.2	28-29	Gradual Expansion	0.3
11-12	Frictional Loss	<0.1	29-30	Frictional Loss	<0.1
12-13	Sudden Contraction	2.3	30-31	Sudden Expansion	<0.1
13-14	90° Bend	5.2	31-32	Frictional Loss	<0.1
14-15	Frictional Loss	<0.1	32-33	Sudden Contraction	1.5
15-16	Sudden Contraction	658.5	33-34	Frictional Loss	<0.1
16-17	90° Bend	861.0	34-35	Sudden Contraction	0.2
17-18	Frictional Loss	131.4	35-36	Frictional Loss	0.2
			36-37	Sudden Expansion	<0.1
18-19	Orifice Region	---	37-38	Frictional Loss	<0.1
	Total 1-18	**1,661.7**		Total 19-38	**11,649.3**
				Combined Total	**13,311.0**

The results for the two additional experimental single-phase datasets are 35.44 ± 4.67 kPa and 35.97 ± 4.40 kPa, giving an average orifice pressure drop for the three single-phase datasets is likewise 36.72 ± 2.63 kPa when calculated as in Equations (4.73) and (4.74) as follows:

$$\Delta P_{\text{ori,avg}} = \frac{1}{3}\left(\Delta P_{\text{ori},1} + \Delta P_{\text{ori},2} + \Delta P_{\text{ori},3}\right) \tag{4.73}$$

$$\delta P_{\text{ori,avg}} = \sqrt{\left(\frac{\delta P_{\text{ori},1}}{3}\right)^2 + \left(\frac{\delta P_{\text{ori},2}}{3}\right)^2 + \left(\frac{\delta P_{\text{ori},3}}{3}\right)^2} \tag{4.74}$$

The pressure drop between the upstream pressure sensor and the channel inlet is what is ultimately desired and has a value of 38.36 ± 2.65 kPa. This value is used along with the upstream pressure measurements from each of the three experimental cases herein examined to determine the corresponding channel inlet pressure for the models. The inlet conditions for the three modeled temperature cases are given in Table 4-11.

The local single-phase pressure as a function of centerline distance between the upstream and downstream pressure taps for the sample case is shown in Figure 4-10. As can be seen, pressure

Table 4-11: Channel inlet conditions for computational models.

Property	Units	Nominal Heater Temperature		
		40 °C	50 °C	60 °C
Mass Flow Rate	[g min^{-1}]	100.8	99.8	99.7
Inlet Pressure	[kPa]	582.9	584.7	595.1
Inlet Temp	[°C]	14.5	14.5	11.5
Applied Heat Flux	[kW m^{-2}]	3640	6980	9930

drop is dominated by the orifice and the channels, where pressure drops from 620.4 kPa to 583.7 kPa and from 583.7 kPa to 574.7 kPa, respectively, with only a small proportion of the total pressure drop occurring upstream of the orifice. During testing, fluid remains single-phase in this upstream region while changing to a two-phase mixture within the channels. This leaves pressure drop unchanged in the upstream region as compared to the purely single-phase data examined in this section while the pressure drop in the channels will increase dramatically. As a result, the

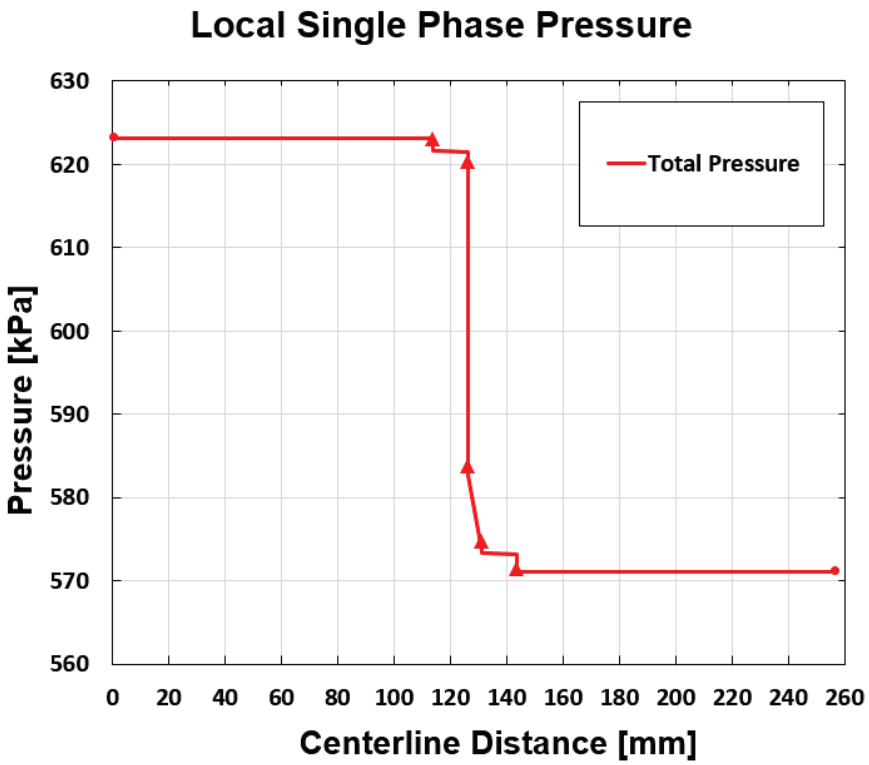

Figure 4-10: Local pressure for sample case as a function of centerline distance between upstream and downstream pressure taps.

proportion of pressure drop occurring in the upstream region decreases even further, yielding a situation in which the exact estimation of this pressure drop value is unnecessary. For this reason, it can safely be assumed that the correlational method used here for estimating this pressure drop is sufficient.

4.4 Meshing

The final step prior to solving is construction of an appropriate mesh, which defines element size, shape and number. The final mesh, shown in Figure 4-11, is produced by applying a mask of quadratic elements on one end of the model and sweeping this mask along the length of the channel. Divisions along the axial direction further subdivide the mesh into finer elements. The goal of any mesh is to provide an adequate number and distribution of elements to achieve accurate solutions without creating excess elements that increase the computation time. For this reason, the channel is split into three sections: the midsection covering the central 1.5 mm of the channel—

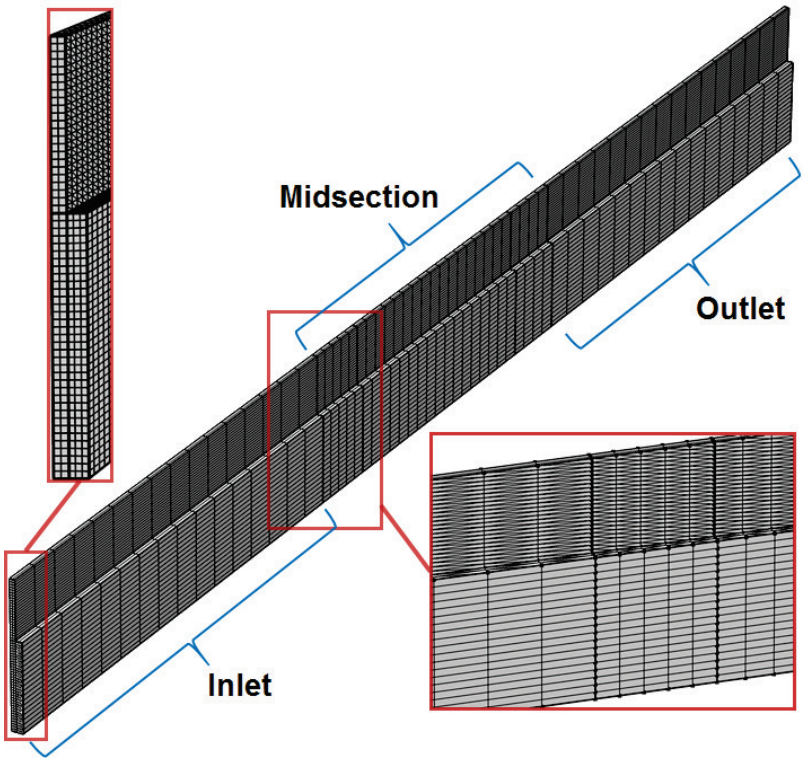

Figure 4-11: COMSOL mesh.

encompassing the region above, and immediately surrounding, the heater—and two identical regions, one inlet and one outlet, on either side of this midsection. A finer mesh is applied in the midsection, where thermal gradients are greatest, to accurately capture heat transfer behavior. A coarser mesh can be applied to the inlet/outlet regions with no loss of accuracy. The quadratic elements on the convective surfaces were then further divided into triangular elements to accommodate requirements of certain built in COMSOL functions. A mesh sensitivity study was performed to ensure solution fidelity and will be detailed further at the end of the chapter.

4.5 Solution Method

The solution procedure for the computational model is shown in the diagram of Figure 4-12. The first steps, such as specifying the geometry, boundary conditions and inlet fluid state have already been described, but one more step must be completed before the model can solve. The discussion of temperature calculations in Section 4.3.1 assumed a pressure distribution is already known. COMSOL reads the pressure distribution from a saved file and uses it to determine the local fluid saturation pressure, and, therefore, the transition location from single- to two-phase heat transfer. If no pressure distribution is available, COMSOL cannot run. Therefore, the model must be primed with an initial pressure distribution generated by the user. Either a constant pressure can be chosen, or some approximation of the expected pressure. Once a pressure file is created, COMSOL can attempt to find a solution. COMSOL iterates until the heat transfer solution has converged to the specified tolerance, which in this case was set to a residual of 0.01. MATLAB then takes this solution and extracts the values of mass flux and hydraulic diameter as well as the necessary distributions for density, viscosity, Reynolds number and vapor quality—for both vapor and liquid where applicable. A new pressure distribution is then calculated as described in Section 4.3.2 and saved. COMSOL then solves the heat transfer problem again. This process continues in

an iterative manner until pressure distribution convergence is reached. After calculating a new distribution, MATLAB compares to this distribution to the previous one, and if the two distributions agree at every location to within ± 50 Pa, the solution is considered to be converged and the loop is exited. Theoretically, the entire process is designed to be automated. Two solvers exist in the COMSOL model so that each initialize with the previous model's solution. Unfortunately, difficulties with convergence in COMSOL forced a manual execution of every step.

When starting with a brand new COMSOL model, heat input had to be stepped up gradually with the above procedure being executed at each subsequent heat input. The ability to converge depended on the size of the increase in a fairly opaque way. Generally, increases had to be fairly "small", but the definition of "small" was inconsistent. Sometimes an increase of 0.05 W was acceptable, and other times an increase of only 0.005 W would work. It was frequently also the case that an increase of, for example, 0.003 W would not work, but an increase of 0.004 W would work. Changes in pressure had to be implemented in the same manner and suffered from the same

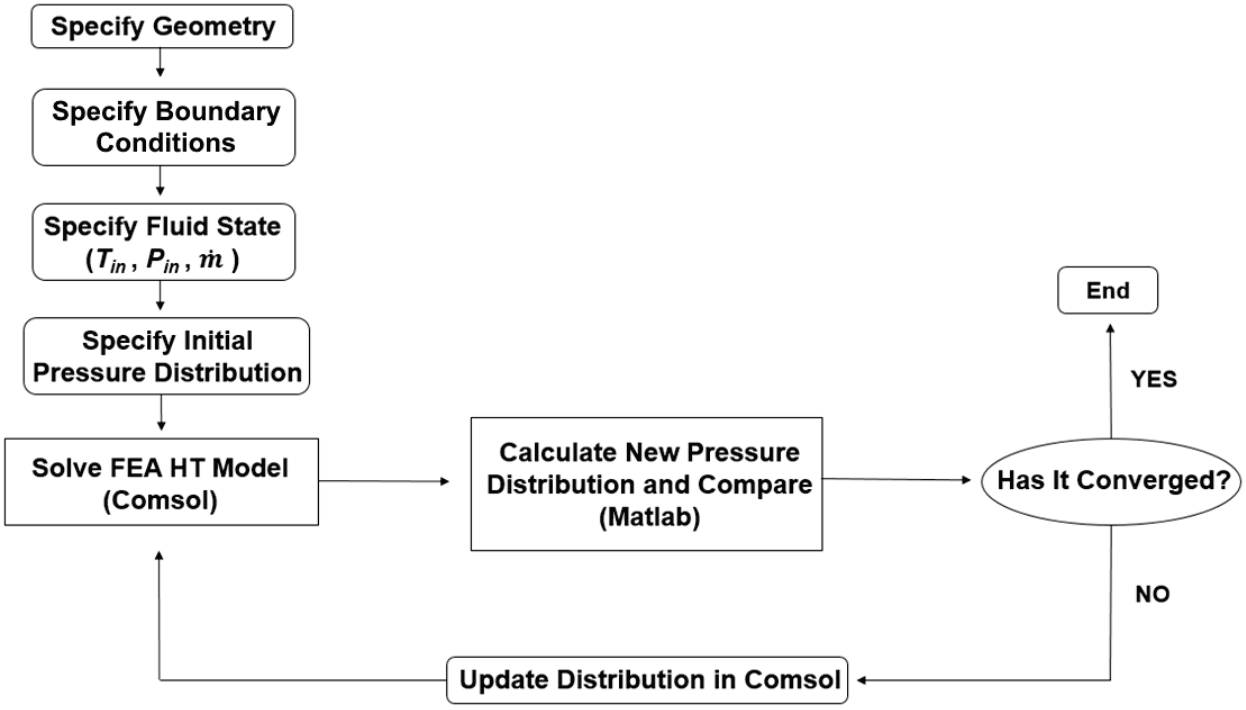

Figure 4-12: Solution procedure for computational model.

inconsistent step size requirements. No clear pattern was observed. Occasionally, COMSOL would not converge with any attempted step-size. When this occurred, it was found that the issue could usually be solved by switching the heat transfer coefficient away from the prescribed correlation and to a predefined distribution taken from the previous, successfully solved solution. A transition from the predefined distribution back to the correlation could then be implemented across a number of subsequent runs by gradually decreasing the weight of the distribution and increasing the weight of the correlation. The step-size for this change in weighting was also found to be highly variable. Given enough manual adjustment, all models were able to be solved completely.

4.6 Validation

To ensure that the model was working correctly a simple situation was modeled, and the results compared to a 2D finite difference method solution. For this comparison, a uniform heat flux of 100 MW cm^{-2} (equivalent to 1 W μm^{-2}) was applied to the base of the model and a uniform heat transfer coefficient of 100 MW cm^{-2} K^{-1} (equivalent to 1 W μm^{-2} K^{-1}) was applied to the convective surfaces of the model. Boundary conditions for this model are given in Table 4-12. For simplicity, the thermal conductivity of the heat sink materials was set to a value of 10 kW cm^{-1} K^{-1} (equivalent to 1 W μm^{-1} K^{-1}) and the ambient temperature was assumed to have a value of 300 K. The grid size chosen for the finite difference calculations was 2.5 μm in both the X- and Z-directions (see Section 4.1.2 for the grid direction). Table 4-13 gives the temperature equations for the corresponding finite difference model nodes shown in Figure 4-13.

Figure 4-14 compares edge temperature profiles for both models. The RMS difference values (as calculated at the location of each finite difference node) for the back, front, wall and floor are 1.7°C, 0.06°C, 0.03°C and 0.04°C, respectively. These equate to less than 0.6 %, 0.1%, 1.3% and 4.1% of the total temperature difference along the respective edges.

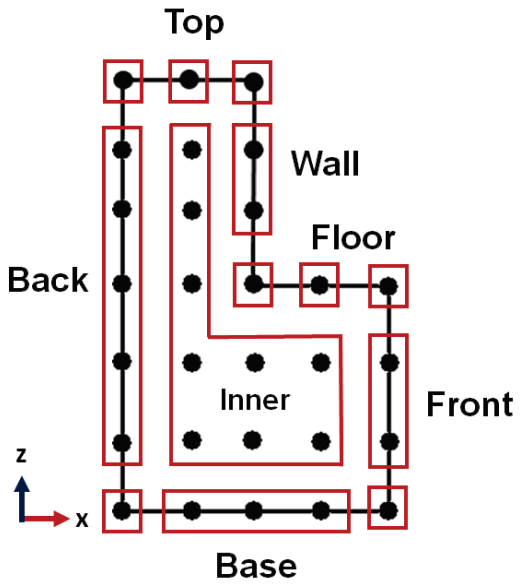

Figure 4-13: 2D finite difference model (not to scale). Groups of related nodes are separated in boxes.

Table 4-12: Boundary conditions for validation model.

Geometry	Boundary Condition
Wall & Floor	Convection (HTC: 100 MW $cm^{-2} K^{-1}$)
Base	Heat Input (100 MW cm^{-2})
Remaining	Adiabatic

Table 4-13: Finite difference model equations corresponding to the nodes shown in Figure 4-13.

Node Location		Temperature Equation
Inner		$\frac{1}{4}(T_A + T_R + T_B + T_L)$
Edges	Top	$\frac{1}{4}(T_R + 2T_B + T_L)$
	Wall	$\frac{1}{2}\left(\frac{k(T_A + T_B + 2T_L) + 2h\Delta x T_{amb}}{2k + h\Delta x}\right)$
	Floor	$\frac{1}{2}\left(\frac{k(T_R + 2T_B + T_L) + 2h\Delta x T_{amb}}{2k + h\Delta x}\right)$
	Front	$\frac{1}{4}(T_A + T_B + 2T_L)$
	Base	$\frac{1}{4}(2T_A + T_R + T_L) + \frac{1}{2}\left(\frac{q''\Delta x}{k}\right)$
	Back	$\frac{1}{4}(T_A + T_B + 2T_R)$
Corners	Top/Wall	$\frac{k(T_B + T_L) + h\Delta x T_{amb}}{2k + h\Delta x}$
	Wall/Floor	$\frac{1}{2}\left(\frac{k(T_A + T_R + 2T_B + 2T_L) + 2h\Delta x T_{amb}}{3k + h\Delta x}\right)$
	Floor/Front	$\frac{k(T_B + T_L) + h\Delta x T_{amb}}{2k + h\Delta x}$
	Front/Base	$\frac{1}{2}\left(T_A + T_L + \frac{q''\Delta x}{k}\right)$
	Base/Back	$\frac{1}{2}\left(T_A + T_R + \frac{q''\Delta x}{k}\right)$
	Back/Top	$\frac{1}{2}(T_B + T_L)$

4.7 Mesh Sensitivity Study

Mesh design has an enormous impact on both computational time and accuracy. An iteration during a COMSOL solution can take anywhere from a couple of seconds to well over an hour, depending on the number of elements. A mesh with very large elements may yield a solution in a matter of seconds but produce very inaccurate results. As the mesh is refined and element size is decreased, accuracy is increased at the expense of computation time. At some point, decreasing element size adds significantly to the computation time without giving any appreciable increase in accuracy. To find this point, a mesh sensitivity study was performed.

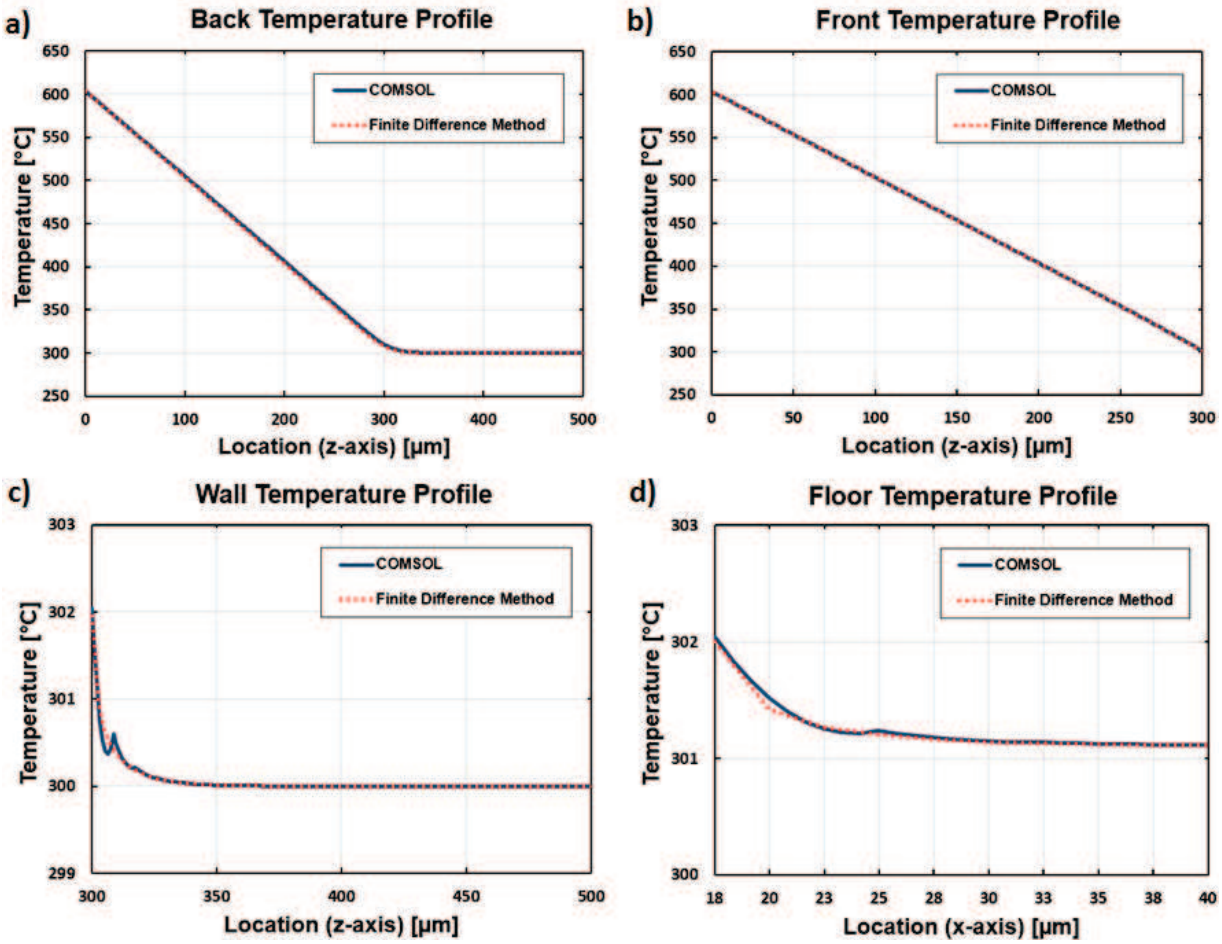

Figure 4-14: Comparisons of COMSOL and finite difference method temperature profiles for the model (a) back, (b) front, (c) wall and (d) floor.

A model using an applied heat flux of 3950 W m^{-2} and employing the Lazarek and Black two-phase correlation was used for this sensitivity study. The number of axial divisions in both the inlet/outlet and midsection regions were varied, and solution results were compared to determine the appropriate mesh to use. Several different combinations of inlet/outlet and midsection element lengths were compared until two consecutive meshes yielded the same pressure drop to within 0.03% and the same average temperatures to within one tenth of one degree Celsius. Convergence was reached between meshes #7 and #8. The number of divisions in each inlet/outlet regions ranged from 4 - 14 (element lengths of 430 µm - 125 µm) and the number of divisions in the

midsection ranged from 7 - 200 (element length of 214 μm - 7.5 μm). Results for individual meshes are shown in Table 4-14.

Though no clear monotonic patterns exist as meshes were refined from mesh #1 to mesh #7, it was ultimately determined that mesh #2 was sufficient. Mesh #2 agreed more closely with meshes #7 and #8 than all intermediate meshes save for mesh #6, which agreed only slightly better. Mesh #2 required significantly less computation time than mesh #6 and so was chosen as the final mesh. Heat transfer coefficient correlations frequently predict data to no better than ± 30% of the true value, so slight inaccuracies due to potential mesh issues caused by this choice are insignificant. Element height and depth were set to a maximum size of $1/4^{th}$ of the fin width. Though larger sizes proved to yield similar results, this was the maximum size that ensured that the fin section of the model was at least 2 elements deep. The result was a floor depth and height of 5 × 35 elements and a fin depth and height of 2 × 23 elements.

Table 4-14: Results of mesh sensitivity study using the Lazarek and Black two-phase correlation and an applied heat flux of 3950 W m^{-2}.

Mesh Characteristics								
Label	**1**	**2**	**3**	**4**	**5**	**6**	**7**	**8**
Inlet/Outlet Divisions	8	14	14	14	28	28	28	28
Midsection Divisions	5	15	21	27	27	51	100	200
Number of Elements	5,291	11,803	14,245	16,687	22,385	32,153	51,689	90,761
Comparison Metrics								
Pressure Drop [kPa]	37.6	37.57	37.61	37.95	37.96	37.59	37.59	37.59
Location [mm]	**Average Temperature [°C]**							
0.5	22.8	22.9	24.6	22.8	22.8	22.9	23.0	23.0
1.0	24.9	25.1	27.2	25.0	25.0	25.1	25.2	25.2
1.5	29.0	29.2	32.1	29.0	29.0	29.2	29.3	29.3
2.0	35.5	35.9	40.2	35.6	35.6	36.0	36.1	36.1
2.5	37.7	38.0	43.0	37.8	37.8	38.1	38.3	38.3
3.0	31.0	31.1	34.1	31.0	31.0	31.2	31.3	31.3
3.5	24.5	24.5	25.3	24.5	24.5	24.5	24.5	24.5
4.0	22.2	22.2	22.5	22.2	22.2	22.2	22.2	22.2
4.5	21.3	21.3	21.4	21.3	21.2	21.3	21.3	21.3

Chapter 5: Results and Discussion

Heat transfer coefficient correlations are typically evaluated by comparison to assumed experimental results. Making the assumption of 1D heat transfer, both the heat flux and heat sink temperature at the channel walls is known and the experimental heat transfer coefficient can be calculated as follows:

$$h_{1D} = \frac{q''}{\left(T_{\text{wall}} - T_{\text{fluid}}\right)} \tag{5.1}$$

The current work analyzes several heat transfer coefficient correlations applied to conjugate heat transfer situations. Therefore, heat transfer coefficients cannot be examined in the typical way. Neither the local heat flux nor the local wall temperature is known. As an alternative, heat sink base temperatures measured during experimentation are compared to model base temperatures at the same locations. Experimental measurements are taken axially at 0.5 mm intervals along the full length of the channels using an infrared pyrometer (see Section 3.3). The pyrometer records the average temperature over a 0.9 mm spot size and thus captures a region encompassing 0.45 mm upstream to 0.45 mm downstream of the measurement location. For accurate comparison, model temperatures are averaged along the same upstream and downstream distance. Experimental measurements are weighted slightly toward the central axial location due to the measured circular region spanning multiple channels, but for simplicity this fact has been ignored in the comparison. This weighting is expecting to have only a very minor effect on the results due to the approximate nature of heat transfer coefficient correlations.

A comparison of full model temperature profiles and experimental measurements for all correlations at each nominal temperature is shown in Figure 5-1. It can be seen that the majority of models predict temperatures within several degrees of the measured temperature and within

several degrees of each other in the region upstream of the heater. Temperature profiles start to separate as transition to two-phase heat transfer occurs and the different heat transfer coefficient correlations begin to dictate heat transfer behavior. The notable exception to this trend is that the Warrier et al. models differ significantly from the other models and drastically overestimate the base temperature everywhere.

As will be discussed later, the Warrier et al. models predict very low two-phase heat transfer coefficients and so exhibit noticeably different heat transfer behavior from the other models. For this reason, the Warrier et al. models will frequently be considered separately from

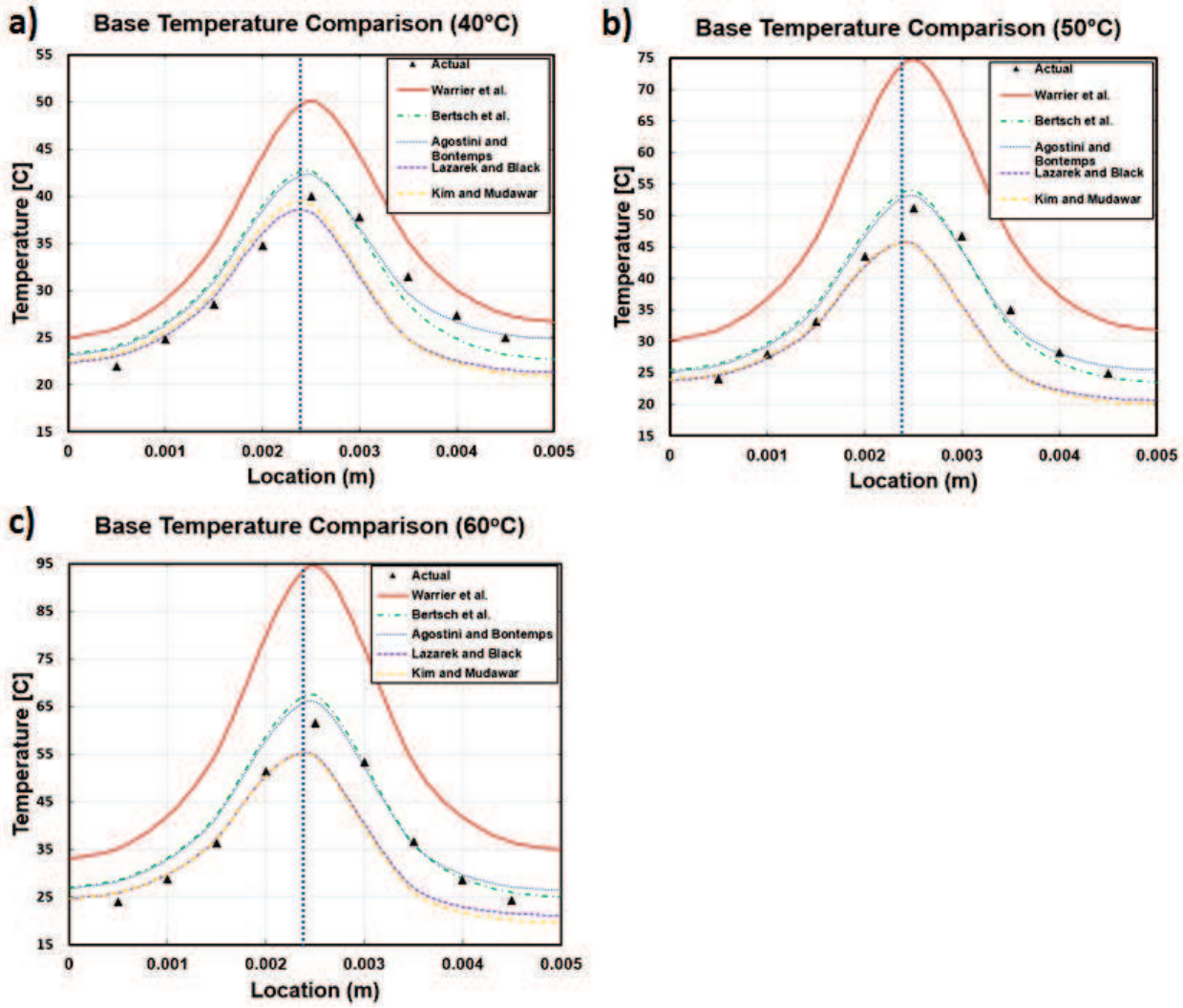

Figure 5-1: Model temperature profiles compared to experimental measurements. Dotted vertical line indicates experimentally determined transition location

the Agostini and Bontemps, Bertsch et al., Kim and Mudawar, and Lazarek and Black models in the discussion that follows.

To quantify the base temperature results, the root mean square (RMS) temperature difference between model and experiment at the experimentally measured locations is calculated. The total RMS values, as well as the single-phase and two-phase values, are shown in Table 5-1. These values were calculated as follows:

$$\Delta T_{\mathrm{RMS}} = \sqrt{\frac{\sum_{i}^{n}\left(T_{\mathrm{model,i}} - T_{\mathrm{experiment,i}}\right)^{2}}{n}} \tag{5.2}$$

If the single- to two-phase transition location coincided with one of the temperature comparison locations, that point was included in the two-phase RMS calculations. It should be noted here that all model transition locations, sans Warrier et al. models, occurred within a range from 2.15 mm to 2.70 mm downstream of the channel inlet, as rounded to the nearest five-hundredths of a millimeter. Experimental transition locations were determined to be between 2.1 mm and 2.5 mm.

Table 5-1: RMS temperature differences.

Correlation	40°C	50°C	60°C	Average
	Total RMS Difference [°C]			
Agostini and Bontemps	2.0	2.0	3.8	2.6
Bertsch et al	2.6	2.5	4.3	3.1
Kim and Mudawar	3.8	6.0	6.9	5.6
Lazarek and Black	3.8	5.8	6.3	5.3
Warrier et al	6.1	14.2	20.3	13.5
	Single Phase RMS Difference [°C]			
Agostini and Bontemps	2.5	2.2	5.0	3.2
Bertsch et al	2.9	2.8	5.7	3.8
Kim and Mudawar	1.3	0.9	1.2	1.1
Lazarek and Black	0.8	1.0	1.2	1.0
Warrier et al	6.4	13.4	19.1	13.0
	Two Phase RMS Difference [°C]			
Agostini and Bontemps	1.5	1.7	2.5	1.9
Bertsch et al	2.4	2.2	2.8	2.5
Kim and Mudawar	5.5	8.0	9.2	7.6
Lazarek and Black	5.5	7.7	8.4	7.2
Warrier et al	5.9	14.9	21.2	14.0

Table 5-2: Model transition locations

Model Transition Locations [mm]			
	Nominal Heater Temp		
	40 °C	50 °C	60 °C
Agostini and Bontemps	2.50	2.20	2.30
Bertsch et al.	2.50	2.15	2.30
Kim and Mudawar	2.70	2.40	2.40
Lazarek and Black	2.65	2.35	2.40
Warrier et al.	2.20	1.65	1.85

The 40°C Kim and Mudawar, and Lazarek and Black models, with transitions locations of 2.70 and 2.65 mm, respectively, were the only two models that fell outside of this experimental range. The Warrier et al. model transition locations ranged from 1.65 mm to 2.20 mm with both the 50°C and 60°C models falling outside of the experimentally determined range. All model transition locations are given in Table 5-2.

The Agostini and Bontemps [72] model and the Bertsch et al. model have the least overall RMS difference values for each nominal heater temperature case, with average RMS values of 2.6°C and 3.1°C respectively. These were followed by the Lazarek and Black [29], the Kim and Mudawar , and finally the Warrier et al. [75] models with RMS values of 5.3°C, 5.6°C and 13.5°C, respectively. Two-phase RMS values followed the same pattern. The Agostini and Bontemps, and Bertsch et al. models had the smallest average RMS values of 1.9°C and 2.5°C, respectively, followed by the Lazarek and Black, the Kim and Mudawar, and the Warrier et al. models with values of 7.2°C, 7.6°C and 14.0°C, respectively. The best single-phase agreement, on the other hand, was obtained by the Lazarek and Black, and Kim and Mudawar models with average RMS difference values of 1.0°C and 1.1°C, respectively. These were followed by the Agostini and Bontemps, Bertsch et al. and Warrier et al. models with RMS values of 3.2°C, 3.8°C and 13.0°C.

In general, RMS difference values tended to increase as nominal heater temperature (and thus applied heat flux) increased. This suggests that differences may continue to grow with even further increases in heat flux, a fact warranting further research.

An important aspect of heat exchanger design for electronics is the ability to accurately predict device temperature. Even temperature differences of a few degrees Celsius can have noticeable impacts on performance. As an example, laser diode temperature resulting from the correlations used in the present study are examined here. As mentioned in Chapter 3, the heater on the experimental test section was designed to mimic a single laser diode bar. Although multiple bars are stacked together to create laser diode arrays, it is assumed that the relative changes in performance will remain the same between single bars and arrays.

The most useful metrics for laser diode arrays are light output power (E_{light}) and heat output (E_{heat}). Light output power and heat output are both functions of the efficiency (η) of the array and the total power supplied (E_{tot}) to the array according to equations (5.3) and (5.4).

$$E_{\text{light}} = \eta E_{\text{tot}} \tag{5.3}$$

$$E_{\text{heat}} = (1-\eta) E_{\text{tot}} \tag{5.4}$$

The work in this thesis considers the temperature and heat output (E_{heat}) of a diode bar so it is convenient to combine the above equations to arrive at equation (5.5).

$$E_{\text{light}} = \left(\frac{\eta}{1-\eta} \right) E_{\text{heat}} \tag{5.5}$$

Efficiency changes with both temperature and input current. The change in efficiency due to changes in temperature are easily calculated via equation (5.6):

$$\eta = \eta_{\text{ref}} \exp\left(\Delta T / T_{\text{ref}} \right) \tag{5.6}$$

where η_{ref} is the efficiency at a given reference temperature, T_{ref}, and ΔT is the difference between the actual and reference diode temperatures. Efficiency changes due to changes in current must be

empirically determined for the diode array in question. As a representative example, the Northrup Grumman MCS051 six-bar array is considered here, and a target diode temperature of 60°C is used to determine the differences in performance metrics. The primary different is between what is expected for a properly operating MCS051 array and those that would be achieved if the operating conditions were established by each of the five correlational models.

First, the expected peak performance of an MCS051 array is at 60°C is determined. The reference efficiency for the MCS051 is 0.577 at a reference temperature of 25°C. If the diode temperature is 60°C instead of 25°C, the expected efficiency (η_{exp}) changes to 0.513 as shown in equations (5.7) and (5.8).

$$\eta_{\text{exp}} = \eta_{\text{ref}} \exp\left(-\left(333\text{ K} - 298\text{ K}\right) \Big/ 298\text{ K} \right) \tag{5.7}$$

$$\eta_{\text{exp}} = 0.889\eta_{\text{ref}} = 0.513 \tag{5.8}$$

The expected light output power for the MCS051 at peak stable performance is 600 W. Thus, The expected heat output at temperatures different that the reference is calculated as follows:

$$E_{\text{heat}} = \left(\frac{1-\eta}{\eta} \right) E_{\text{light}} \tag{5.9}$$

$$E_{\text{heat}} = \left(\frac{1-0.513}{0.513} \right) \left(600\text{ W}\right) = 569.6\text{ W} \tag{5.10}$$

Thus, the expected performance metrics for the MCS051 at 60°C are a light output of 600 W and a heat output of 569.6 W.

This method is used to determine how the heat and light output change due to predictions by each of the five correlational models. The results consider only temperature and heat flux, so the goal is to determine the fractional change (the absolute change in the case of temperature) in these values at a target temperature of 60°C. To do this, the expected heat flux at heater temperature of 60°C is determined first, which allows the heat flux to be predicted by each of the models.

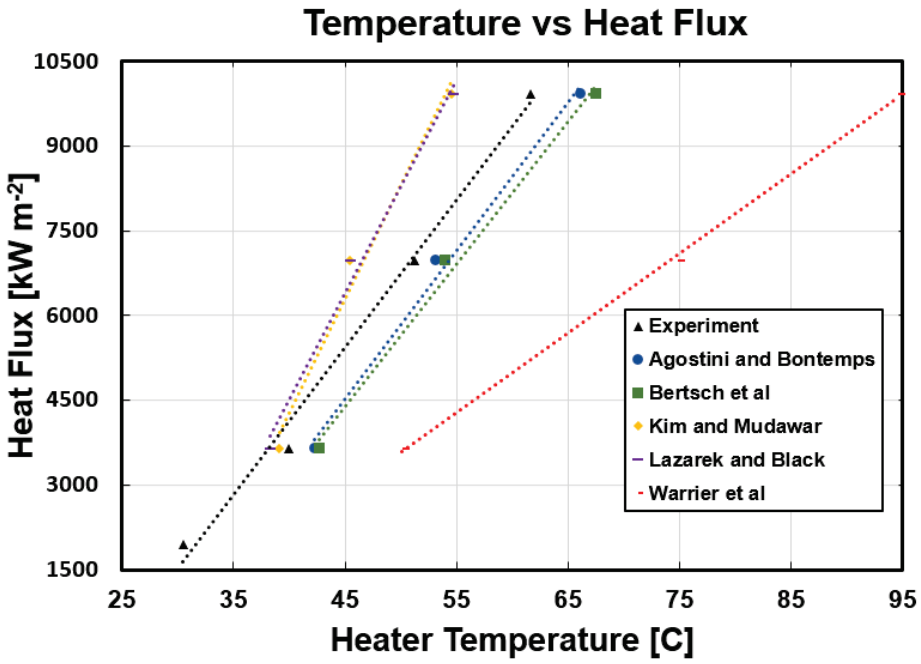

Figure 5-2: Heat flux versus temperature data for experiment and computational models. Linear regressions are shown with dotted lines.

Figure 5-2 shows the heat flux versus temperature data obtained from experiments and models. Linear regression of this data shown in Table 5-3 demonstrate that the results are highly linear. At a temperature of 60°C, the heat fluxes predicted by the expected value, respectively. Since heat flux and heat output are directly proportional, these same fractional changes apply to predicted heat outputs. These ratios are classified as power modification factors (Ω) for use in further calculations. Agostini and Bontemps, Bertsch et al., Kim and Mudawar, Lazarek and Black, and Warrier et al. are 8465 kW m^{-2}, 8180 kW m^{-2}, 12350 kW m^{-2}, 12069 kW m^{-2} and 4992 kW m^{-2},

Table 5-3: Linear regression values for experimental and model data.

	Experiment	Agostini and Bontemps	Bertsch et al	Kim and Mudawar	Lazarek and Black	Warrier et al
Slope [kW m^{-2} °C^{-1}]	261.02	263.21	252.50	402.47	378.17	141.1
y-intercept [kW m^{-2}]	-6321.55	-7328.09	-6970.26	-11797.96	-10621.34	-3473.80
R^2 Value	0.991	0.993	0.993	0.980	0.988	0.999

respectively. The experimental value (9339 kW m^{-2}) is what is expected at 60°C. Thus, in fractional terms, the predicted heat fluxes for each of the five models are 0.906×, 0.876×, 1.322×, 1.292× and 0.535×

To determine the discrepancy in predicted temperature, the heat flux values predicted by each correlation are input into the experimental regression. This provides the predicted temperatures given the error in heat fluxes, which is shown in Table 5-4.. The predicted temperatures for the five models in alphabetical order are 56.6°C, 55.6°C, 71.5°C, 70.5°C and 43.3, respectively, compared to an expected temperature of 60°C.

Using the heat and light output for the model predictions, the effects of altered device temperatures on efficiencies can be calculated. Assuming the diodes at the temperatures predicted in Table 5-4, the efficiencies from equation (5.6) are, in the same alphabetical order, are 0.519, 0.521, 0.494, 0.495 and 0.543, respectively. However, the actual heat fluxes need to be calculated iteratively due to the effect of current on heat generated. The first guess for the heat outputs with each correlations are calculated as follows:

$$E_{\text{heat}} = \Omega\left(\frac{1-\eta}{\eta}\right)E_{\text{light,exp}} \tag{5.11}$$

where $E_{\text{light,exp}}$ is the expected light output of 600 W. Heat outputs for the model predictions, in alphabetical order, are 503.8 W, 483.4 W, 813.3 W, 789.6 W and 270.1 W, respectively.

Table 5-4: Predicted heat fluxes and temperatures for experiment and each correlational model. Power modification factors relate predicted heat fluxes to expected heat flux.

	Expected	Agostini and Bontemps	Bertsch et al	Kim and Mudawar	Lazarek and Black	Warrier et al
Predicted Heat Flux [kW m^{-2}]	9339	8465	8180	12350	12069	4992
Power Modification Factor (Ω)	1.000	0.906	0.876	1.322	1.292	0.535
Temperature Based on Predicted Heat Flux [°C]	60.0	56.6	55.6	71.5	70.5	43.3

Corresponding light output powers from equation (5.5) are 543.8 W, 525.5 W, 793.4 W, 775.4 W and 320.7 W, respectively. These are initial heat and light power output estimations because the current on efficiency. Once the current-altered efficiencies ($\eta_{current}$) are determined, this is combined with the temperature-altered efficiencies (η_{temp}) to determine an overall efficiency (η_{tot}) as follows:

$$\eta_{tot} = \left(\frac{\eta_{temp}}{\eta_{ref}} \right) \eta_{current} \tag{5.12}$$

To calculate the current-altered efficiencies, the MCS051 performance graphs shown in Figure 5-3 are used. Using the initial light power outputs, the associated currents from Figure 5-3a for the five models, in alphabetical order, are 93.3 A, 90.8, 127.9, 125.4 A and 62.4 A, respectively. From Figure 5-3b, the efficiencies at these current levels are 0.572, 0.570, 0.590, 0.589 and 0.520, respectively. Using the Agostini and Bontemps prediction as an example, the overall efficiency using equation (5.12) is as follows:

$$\eta_{tot} = \left(\frac{0.519}{0.577} \right) 0.572 = 0.515 \tag{5.13}$$

Overall efficiencies for the Bertsch et al, Kim and Mudawar, Lazarek and Black, and Warrier et al. predictions are 0.514, 0.505, 0.505 and 0.489, respectively. Unfortunately, these values are not

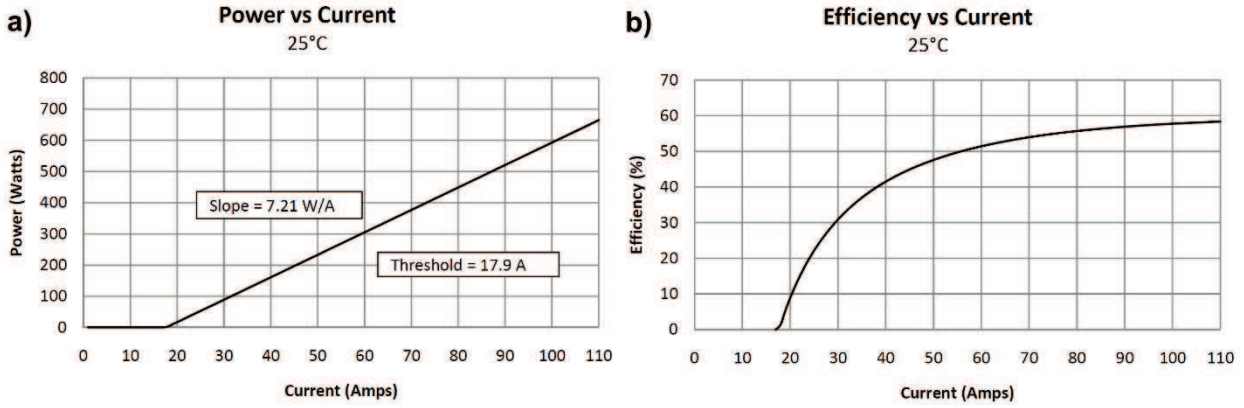

Figure 5-3: MCS051 performance curves shown a) power vs current and b) efficiency vs current at a temperature of 25°C. Peak performance occurs at a light output power of 600 W, a current of 101.1 A and an efficiency equal to the reference efficiency of 0.577.

the same as the initial guess due to the impact of current on the efficiency. A second iteration yields corresponding light output powers from equation (5.5) of 543.8 W, 525.5 W, 793.4 W, 775.4 W and 320.7 W, respectively, which are the same values as the initial guess.

The updated efficiency values only affect the heat output associated with the predicted light output power levels. Using the Agostini and Bontemps, Bertsch et al, Kim and Mudawar, Lazarek and Black, and Warrier et al. predictions would result in light power outputs of 90.6%, 87.6%, 132.2%, 129.2% and 53.5% of the expected value of 600 W. Heat outputs would be 90.1%, 87.3%, 136.9%, 133.4% and 58.8% of the expected value of 569.6 W. Total power outputs would be 90.3%, 87.4%, 134.4%, 131.2% and 56.0%. Diode temperatures would differ by the values shown previously in Table 5-4. These results are summarized in Table 5-5.

The importance of these variations would depend on the application, but it is easy to imagine that producing nearly 37% more heat than expected could cause problems. With systems operating at maximum thermal limits, results such as these could be catastrophic. It is also clear

Table 5-5: Final comparison of performance characteristics for MCS051 array using predictions from each of the five correlational models.

	Expected	Agostini and Bontemps	Bertsch et al	Kim and Mudawar	Lazarek and Black	Warrier et al
Temperature [°C]	60.0	56.6	55.6	71.5	70.5	43.3
Overall Efficiency	0.513	0.515	0.514	0.505	0.505	0.489
Heat Output [W]	569.6	512.9	496.9	778.7	759.3	334.7
Percent of Expected Heat Output [%]	-----	90.1	87.3	136.9	133.4	58.8
Light Output [W]	600	543.8	525.5	793.4	775.4	320.7
Percent of Expected Light Output [%]	-----	90.6	87.6	132.2	129.2	53.5
Total Power Use [W]	1169.6	1056.7	1022.4	1572.1	1534.7	655.4
Percent of Expected Power Use [W]	-----	90.3	87.4	134.4	131.2	56.0

that even a relatively small error in predicted diode temperature could result in a measurable performance decrease, as the Agostini and Bontemps model predicted a temperature just 3.4°C below the true value of 60°C and the light output power decreased by nearly 10%. Discrepancies such as these must be resolved (or at least mitigated) with better correlations before the computational model in this work can act as a guide in maximum performance applications.

Though average base temperatures are the only way to compare the computational models to experimental values, the models may be examined further to gain other insights. Firstly, since peak device temperature is a key concern in many applications, the extent to which the pyrometer averaging masks the true maximum temperature can be determined. Since the Agostini and Bontemps models have the smallest total RMS difference values, these models will be featured in the following discussion. Figure 5-4 compares the local model base temperature (averaged across all elements at the same axial location) to the model base temperature when averaged both upstream and downstream as is done by the pyrometer. The "true" peak base temperature appears to occur slightly upstream of, and is several degrees higher than, the peak suggested by the fully averaged profile. The peak temperature differences for the 40°C, 50°C and 60°C cases shown are 1.7°C, 2.1°C and 3.3°C. Since the underlying physics of heat conduction is well understood, it can be safely assumed that these differences are very similar to those present in the physical device during experimentation.

The model also allows for visualization of 2D/3D local heat transfer coefficient, local heat flux and local temperature profiles. Figure 5-5 shows these profiles for the Agostini and Bontemps models. For reference, the applied experimental and model values can be seen in Table 3-2 and Table 4-2. It is clear from the variation present in local heat flux profiles that the assumption of

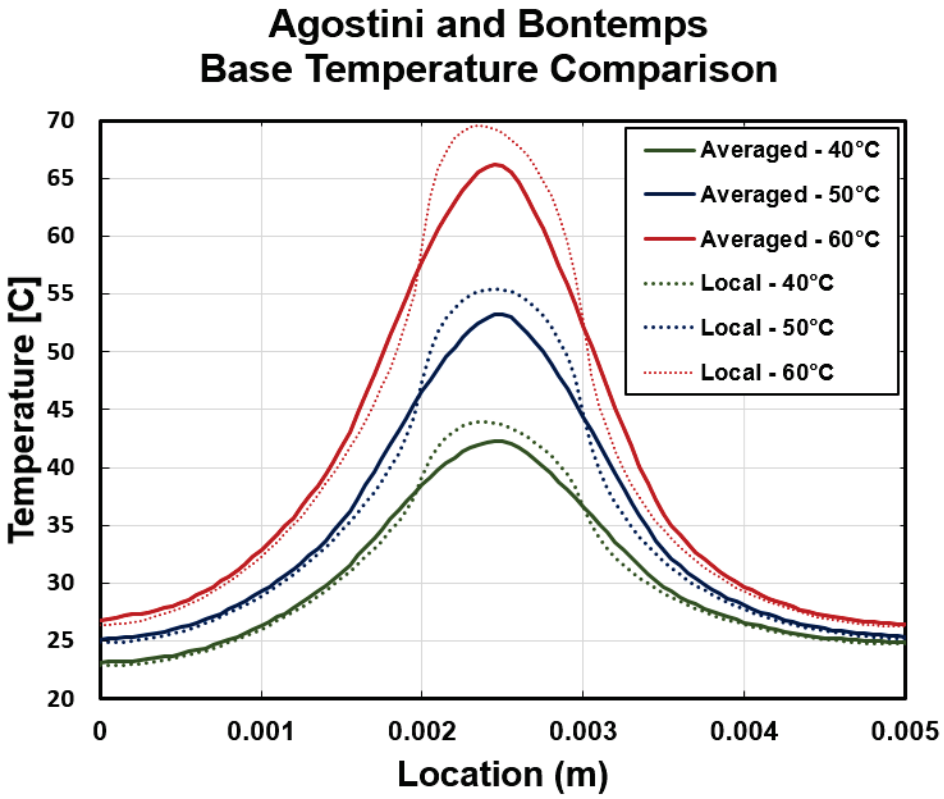

Figure 5-4: Model base temperatures when averaged upstream and downstream to compare to pyrometer measurements (solid) and without averaging (dotted). Peak averaged/non-averaged temperatures for the nominal 40°C, 50°C and 60°C cases are 42.3°C/44.0°C, 53.2°C/55.4°C and 66.2°C/69.5°C, respectively.

1D conduction is invalid. Indeed, this is further demonstrated by the fact that peak channel heat fluxes are significantly lower than the applied heat fluxes. For the 60°C case shown, the peak heat flux of ~ 6030 W m^{-2}, which occurs along the channel floor near the transition location, is roughly 67 % of the applied heat flux of 9950 W m^{-2}. Moving downstream from this axial location but remaining in the region directly over the heater it is also obvious that heat flux along the floor drops below 2800 W m^{-2}, which is less than half the peak floor value. Heat flux also varies greatly even for a given axial location. The peak wall heat flux of ~3080 W m^{-2} for the 60°C case occurs at roughly the same axial location as the peak floor flux and is approximately half the magnitude.

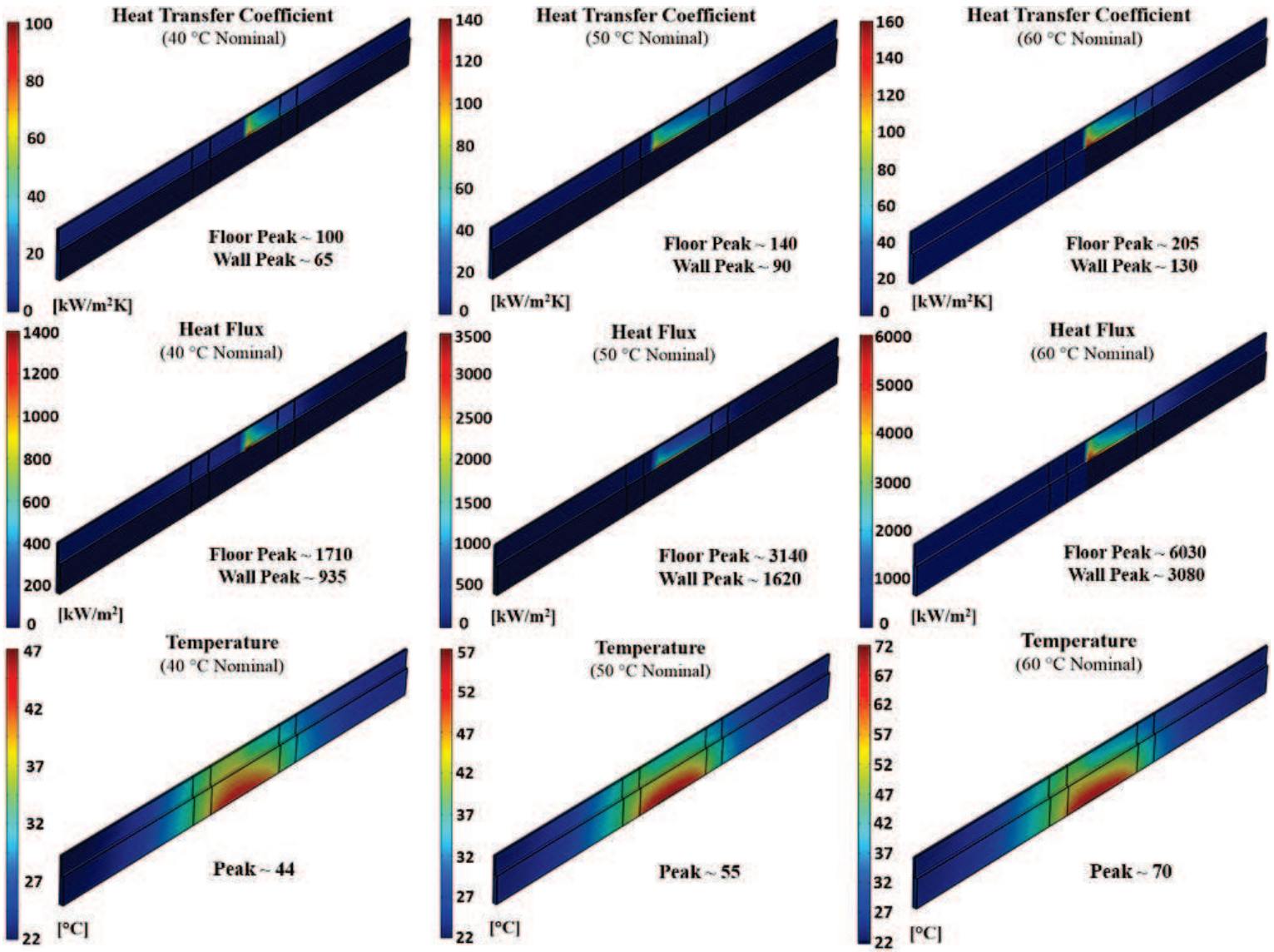

Figure 5-5: Local heat transfer coefficient (top), heat flux (middle) and temperature (bottom) for the Agostini and Bontemps 40°C (left), 50°C (middle) and 60°C (right) models. Peak values are listed. Note that unit scales are different for each figure and that scales have sometimes been adjusted to show greater detail, resulting in peak values lying outside the scale range.

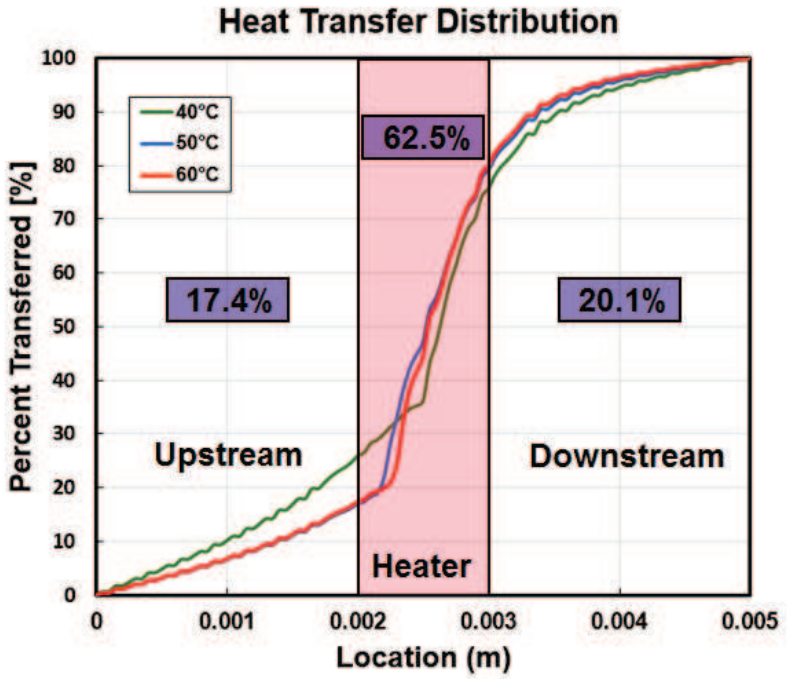

Figure 5-6: Distribution of heat transfer for Agostini and Bontemps models. The percentage of heat transferred in the regions upstream of, directly above, and downstream of the heater are listed. The percentages for the 60°C case are listed.

Local heat transfer coefficient varies similarly due to its strong dependence on heat flux. The peak local coefficient for the 60°C case is 205 kW m^{-2} K^{-1}, compared to other locations in the heater region with local heat transfer coefficients of less than 40 kW m^{-2} K^{-1}. Combining these observations suggests that even using average or bulk heat flux values to determine heat transfer coefficient would fail to accurately characterize heat transfer behavior. The needs to consider conjugate heat transfer and to determine accurate local heat transfer coefficient correlations are clear.

Surface integration of these heat flux profiles allows us to determine where the heat is transferred and to develop a metric for quantifying heat spreading. Figure 5-6 shows the percentage of heat transferred plotted as a function of the axial location for the Agostini and Bontemps models. The amount of heat transferred upstream, directly above and downstream of the heater is 17.4%, 62.5% and 20.1% of the total for the 60°C case. More than one third of the heat spreads away from

the region directly above the heater, again confirming the necessity of considering conjugate heat transfer. The percentage of heat transferred in each of these three regions is given for all models in Table 5-6.

As applied heat flux increases from the 40°C case to the 50°C case, the proportion of total heat transfer occurring above the heater increases, while the proportion occurring both the upstream and downstream regions decreases. The average amount of heat transferred in the region above the heater increases from 47.1% to 59.8% of the total, while the average amounts in the upstream and downstream regions decreased from 26.4% to 18.6% and 26.5% to 21.6%, respectively. The decrease in the upstream, single-phase percentage is to be expected as the sensible heat loss in this region is determined by the amount of inlet subcooling, which remains constant. While the total amount of heat transfer in both the heater and downstream regions

Table 5-6: Percentage of heat transferred in the upstream, heater, and downstream regions.

Model	Upstream	Heater	Downstream
		40 °C Heater	
Agostini and Bontemps	26.0	49.7	24.3
Bertsch et al	26.5	45.6	27.9
Kim and Mudawar	24.0	50.7	25.2
Lazarek and Black	23.3	53.3	23.5
Warrier et al	32.4	35.9	31.7
Average	26.4	47.1	26.5
		50 °C Heater	
Agostini and Bontemps	17.1	62.1	20.9
Bertsch et al	17.5	60.0	22.4
Kim and Mudawar	15.0	67.0	18.0
Lazarek and Black	13.8	69.1	17.2
Warrier et al	29.6	40.8	29.6
Average	18.6	59.8	21.6
		60 °C Heater	
Agostini and Bontemps	17.4	62.5	20.1
Bertsch et al	17.7	61.2	21.1
Kim and Mudawar	14.8	68.2	17.0
Lazarek and Black	14.8	68.6	16.6
Warrier et al	27.0	44.9	28.2
Average	18.3	61.1	20.6

increases, the increase in the heater region is much greater. This is due to the heat transfer coefficient dependence on heat flux resulting in much higher heat transfer coefficients in the heater region than in the downstream region. This trend continues as applied flux continues to increase from the 50°C case to the 60°C case, though the results are muted somewhat by the increase in inlet subcooling and subsequently larger upstream sensible heat loss. Total heat transfer above the heater increases from 59.8% to 61.1% and total downstream heat transfer decreases from 21.6% to 20.6%. Upstream heat transfer actually increases slightly in some individual cases due to the increased subcooling, but the average decreases from 18.6% to 18.3%. It should be noted that the Warrier et al. models were included in the averages since this metric considers proportions as opposed to actual numbers. A greater percentage of heat transfer does occur in the upstream and downstream regions of the Warrier et al. models as compared to the other models, but the trends with in increasing heat flux remain the same.

The easiest way to quantitatively compare heat transfer coefficients is to examine the perimeter averaged heat transfer coefficient for each model. Figure 5-7 shows a plot of perimeter averaged heat transfer coefficient versus axial location for the 60°C models for all correlations. Single-phase heat transfer coefficients are nearly constant around 8300 kW m^{-2} K^{-1} and vary by no more than 1.1% across all models at any given axial location, an expected result since the same single-phase correlation was used for all models. Two-phase coefficients, on the other hand, have extreme variations. As can be seen, the peak average heat transfer coefficient values for the Kim and Mudawar and the Lazarek and Black models are roughly 3× that of the peak for the Agostini and Bontemps model, roughly 4× that of the peak for the Bertsch et al. model, and roughly 18× that of the peak for the Warrier et al. model. This plot also shows the variance in predicted single-phase to two-phase transition locations across the models with the core four model transitions

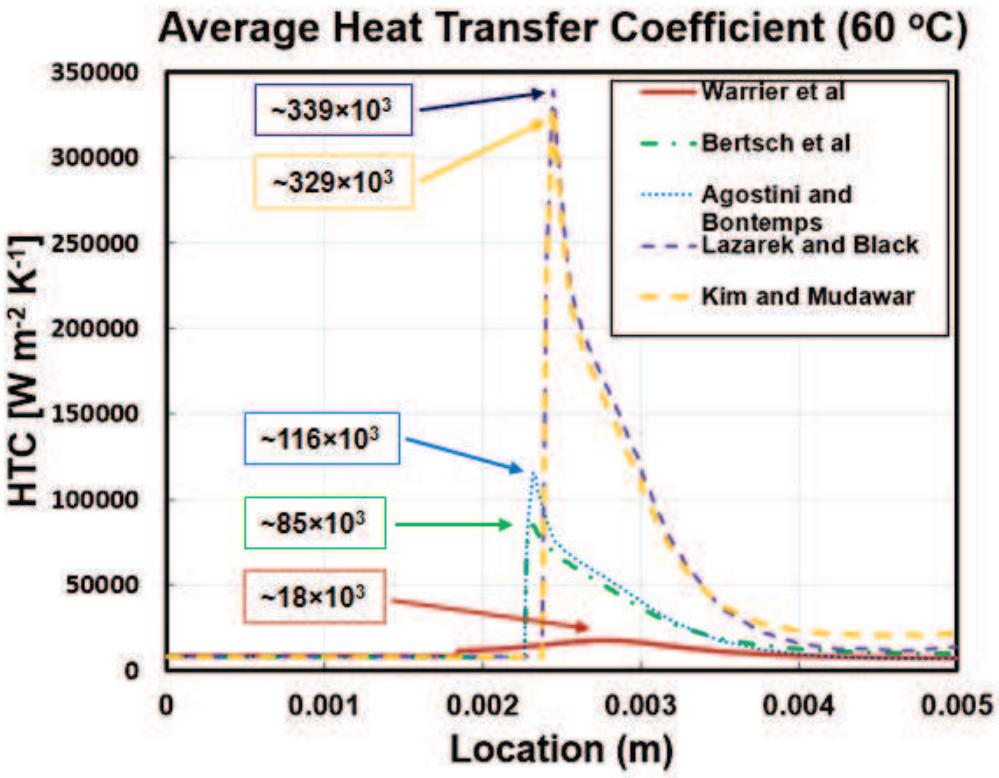

Figure 5-7: Perimeter averaged heater transfer coefficient. Maximum values are listed.

located relatively close together and the Warrier et al. model transition located noticeably farther upstream. Combining Figure 5-7 with the information in Table 5-6 shows that higher peak average heat transfer coefficients correspond to a greater proportion of heat transfer occurring in the two-phase region and, relatedly, later single- to two-phase transition locations. These shifts in heat spreading are relatively minor due to the extremely high two-phase heat transfer coefficients which result in low convective thermal resistances, but the shifts are present nevertheless. This figure also shows that the location of peak average heat transfer coefficient varies between the models. Peak coefficients occur very soon after transition to two-phase flow for the Agostini and Bontemps, Bertsch et al., Kim and Mudawar, and Lazarek and Black models, while the peak value for the Warrier et al. model occurs nearly 1 mm farther downstream. This delayed peak heat transfer coefficient in the Warrier et al. model is likely due both to the transition location occurring

outside the region of applied heat and to the somewhat complex relationship between heat flux and heat transfer coefficient in the Warrier et al. correlation.

The interplay between temperature, heat spreading and heat transfer coefficient makes it difficult to draw specific conclusions as to how heat transfer coefficient correlations might be altered to achieve better temperature agreement with the experiment. Careful comparison of the previously discussed results does, however, suggest one possible adjustment to the present set of correlations. The best single-phase agreement, as evidenced by the RMS difference values, is obtained with the Lazarek and Black, and Kim and Mudawar models. This is clearly visible in Figure 5-1. It is also the case that these two models have the highest two-phase heat transfer coefficients. Despite minor changes in transition location—and thus transition saturation temperature—the sensible heat loss for all models at a given nominal heater temperature condition may be considered roughly constant. The large two-phase heat transfer coefficients predicted by the Lazarek and Black, and Kim and Mudawar correlations result in less upstream heat spreading, later transition locations and thus a greater overall surface area over which the sensible heat may be dissipated. Given that single-phase heat transfer coefficients are roughly constant, according to Newton's law of cooling (Equation (5.3)), a larger area over which to dissipate the same amount of heat would suggest lower necessary driving temperatures.

$$q = hA\left(T_{\text{wall}} - T_{\text{fluid}}\right) \tag{5.14}$$

Indeed, this is what is seen in Figure 5-1. The Lazarek and Black and the Kim and Mudawar models have lower silicon temperatures. The average two-phase heat transfer coefficients for these two models are clearly too high based on the poor two-phase agreement. Thus, the single-phase area available to dissipate the sensible heat is too great. An alternative solution is that the single-phase heat transfer be increased as a means of improving the single-phase temperature agreement.

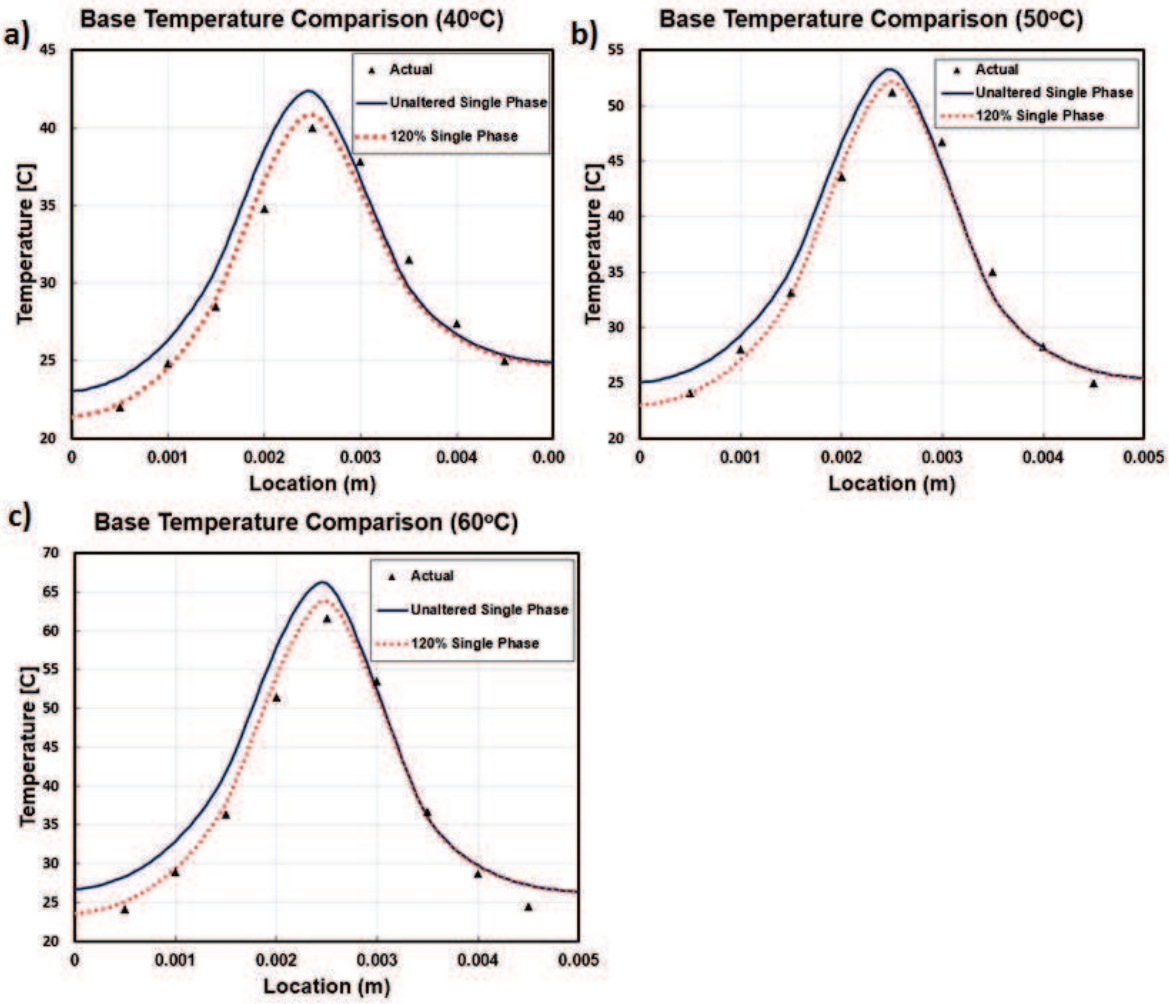

Figure 5-8:Averaged base temperatures using Agostini and Bontemps two phase correlation with unaltered and altered versions of the Kim and Mudawar single phase correlations for (a) 40°C, (b) 50°C and (c) 60°C nominal heater temperature cases.

Figure 5-8 compares the results of the Agostini and Bontemps models discussed previously to the same models when the single-phase heat transfer coefficient from Kim and Mudawar is simply multiplied by a factor of 1.2 as shown in Equation (5.4), below:

$$Nu = 1.2\left\{\left[1.54\left(\frac{L_{sp}}{\mathrm{Re}_{sp}\,\mathrm{Pr}_l\,D_h}\right)^{-0.33}\right]^4 + Nu_3{}^4\right\}^{1/4} \tag{5.15}$$

Table 5-7 shows the new RMS temperature difference values. As anticipated, this change increases the agreement in the single-phase region with the average single-phase RMS difference decreasing from 3.3°C to 1.6°C. Interestingly, the two-phase region agreement improved as well, with the

Table 5-7: RMS difference values for Agostini and Bontemps models with single-phase heat transfer coefficient multiplied by factor of 1.2.

Heater Temp [°C]	Single-phase RMS [°C]	Two-phase RMS [°C]	Overall RMS [°C]
Unaltered Single-Phase Correlation			
40	2.5	1.5	2.0
50	2.2	1.7	2.0
60	5.0	2.5	3.8
Average	3.2	1.9	2.6
Altered Single-Phase Correlation			
40	1.3	1.3	1.3
50	0.7	1.7	1.3
60	2.7	2.1	2.3
Average	1.6	1.7	1.6

RMS difference decreasing slightly from 1.9°C to 1.7°C. The average overall RMS difference decreased from 2.6°C to 1.6°C. This result lends credibility to the idea that single-phase heat transfer coefficient should be higher than that predicted by the Kim and Mudawar correlation, but more extensive research is necessary before this can be determined with certainty. It should be noted that single-phase flow is assumed to be in the thermally developing laminar flow region as the total single-phase length of <2.5 mm is much less than the thermally developing laminar entrance length of ~6 mm as given by the following equation from Bergman et al. [164]:

$$L_{\mathrm{fd,th}} = 0.05 ReD_{\mathrm{h}} Pr \tag{5.16}$$

However, it is possible that some fluid jetting may occur as fluid enters the channel, potentially increasing the local single-phase heat transfer coefficient.

Another interesting result is the determination of the relative contributions of both nucleate and convective boiling to the total heat transfer amount. Both the Bertsch et al. and the Kim and Mudawar correlations divide the total two-phase heat transfer coefficient into nucleate and

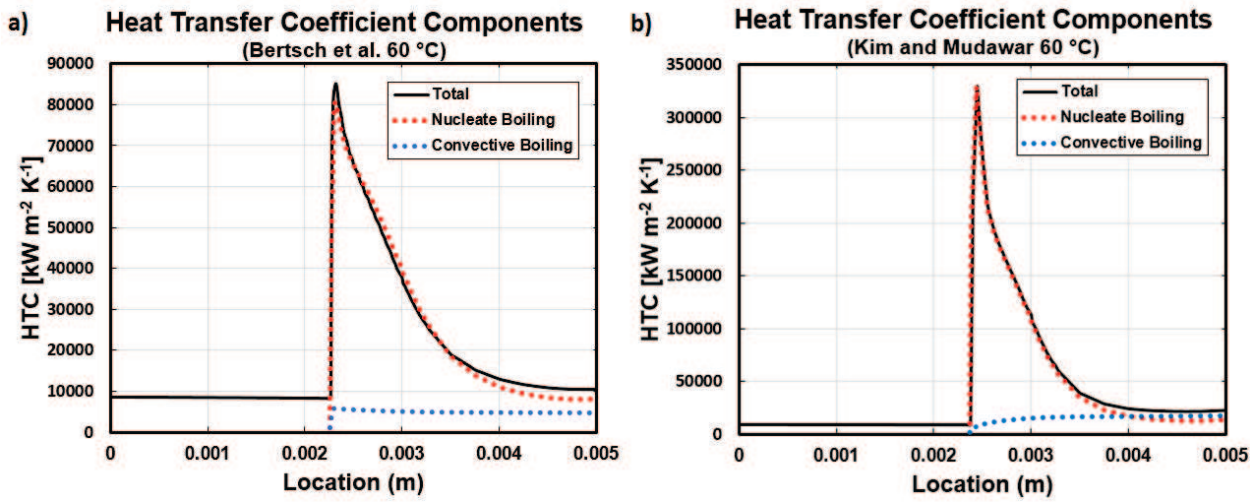

Figure 5-9: Comparison of nucleate and convective boiling contributions to total heat transfer coefficient for the Kim and Mudawar 60°C nominal temperature model.

convective terms. Figure 5-9 shows the nucleate and convective terms as compared to the total heat transfer coefficient. The terms are adjusted slightly in each correlation before being combined to calculate the total heat transfer coefficient, but it is easily seen that the nucleate contribution dominates. This is what one would expect with the high dependence on heat flux and relatively low vapor qualities suggesting mainly slug flow. This also agrees with other observations from the experiments that showed a relatively weak heat transfer coefficient dependence on mass flux as compared to heat flux.

Lastly, Table 5-8 shows pressure drop results for all models. All pressure drops for each nominal temperature case and were consistent with the total measured pressure drops through the system. Total measured pressure drop increases with increasing heat input, as well as increasing exit quality. Estimated channel pressure drop increases as well, but not as rapidly. For the 40°C case, the average channel pressure drop is 37.8 kPa and the total measured pressure drop is 85.9 kPa. For the 50°C case, average channel and total measured pressure drop rise to 58.7 kPa and 142.2 kPa, respectively. This results in an increase of 20.9 kPa through the channels compared an increase of 56.3 kPa overall. Since the single-phase pressure drop should remain constant, this

implies a pressure drop increase of 35.4 kPa downstream of the channels. For the 60°C case, average channel and total measured pressure drop rise to 66.1 kPa and 201.1 kPa, respectively. This results in further channel and total pressure drop increases of 7.4 kPa and 58.9 kPa, respectively, and a downstream pressure drop increase of 51.5 kPa. It is surmised that the smaller than expected pressure drop increase attributable to the channels is due the increased amount of subcooling, and therefore increased sensible heat loss, for the 60°C case. It is clear, however, that downstream pressure drop increases at a greater rate than channel pressure drop. Two-phase pressure losses downstream of the test section should be minimal due to the relatively low fluid velocities and relatively large hydraulic diameters. As such, it can be inferred that significant two-

Table 5-8: Model pressure drop through the channels and total experimentally measured pressure drop.

	Nominal Heater Temp		
	40 °C	**50 °C**	**60 °C**
Estimated Inlet Drop [kPa]	38.4		
Total Measured Drop [kPa]	85.9	142.2	201.1
Channel Pressure Drops [kPa]			
Agostini and Bontemps	38.1	58.2	66.1
Bertsch et al.	37.8	57.8	65.8
Kim and Mudawar	36.4	56.4	65.3
Lazarek and Black	37.0	59.4	65.5
Warrier et al.	39.5	61.5	68.0
Average	37.8 ± 1.1	58.7 ± 1.7	66.1 ± 1.0
Upstream Pressure Drop [kPa]			
	38.4 ± 2.6	38.4 ± 2.6	38.4 ± 2.6
Downstream Pressure Drop [kPa]			
	9.7 ± 2.0	45.1 ± 2.2	96.6 ± 2.0

phase jetting occurs at the channel exits, accounting for much of this pressure loss, a topic that should be explored further in future research.

Chapter 6: Conclusions and Recommendations

The current work has used finite element analysis (FEA)—utilizing COMSOL Multiphysics and MATLAB—to explore conjugate heat transfer during microchannel flow boiling and determine the validity of several published heat transfer coefficient correlations. It is the first of its kind to model completely local heat transfer coefficients, a necessary requirement for the prediction of heat transfer performance of thermal management systems for the next generation of extremely high heat flux electronic components. This work clearly demonstrates the need to consider heat spreading and conjugate heat transfer, as well as demonstrating the ability of FEA to aid in future heat exchanger design.

Pressure drop correlations from Lee and Garimella [159] were used along with a single-phase heat transfer coefficient correlation from Kim and Mudawar [156] to evaluate two-phase heat transfer correlations presented by Agostini and Bontemps [72], Bertsch et al. [21], Kim and Mudawar [20], Lazarek and Black [29] and Warrier et al. [75]. The results are summarized below.

- The best overall agreement was achieved by the Agostini and Bontemps model with average total RMS temperature differences of 2.6°C. The Agostini and Bontemps model also yielded the best two-phase region agreement with an average RMS difference of 1.9°C, while the best single-phase region agreement was obtained by the Lazarek and Black, and Kim and Mudawar models with RMS differences of 1.0°C and 1.1° C, respectively.
- Using the five correlational models to estimate laser diode performance at 60°C resulted in light output powers of 53.5% - 132.2% of the expected value and heat outputs of 58.8% - 136.9% of the expected value. Even small differences in predicted peak temperatures

(<5°C) can have measurable impacts on device performance (≥~10% of predicted light output, heat output and total power consumption).

- The upstream and downstream pyrometer temperature averaging masks the true peak base temperatures by only several degrees; however, this difference increases with increased applied heat flux.
- For the 40°C, 50°C and 60°C nominal heater temperature cases, with applied heat fluxes of 3650 W m^{-2}, 6975 W m^{-2} and 9950 W m^{-2}, the peak predicted channel local heat fluxes are, respectively, ~1710 W m^{-2}, ~3140 W m^{-2} and ~6030 W m^{-2} for the most accurate results (Agostini and Bontemps models). This shows that heat spreading is a significant factor and, that even though peak channel heat fluxes are substantially lower than the applied values, they are still higher than those for which any current heat transfer correlations are designed. The peak local heat transfer coefficients for these models are ~100 kW m^{-2} K^{-1}, ~140 kW m^{-2} K^{-1} and ~205 kW m^{-2} K^{-1}.
- Between 31.4% and 64.1% of input heat was dissipated outside of the region immediately above the applied heat flux for all models. Regions upstream of the heater (axial locations of 0.0 mm – 2.0 mm), directly above the heater (axial locations of 2.0 mm – 3.0 mm) and downstream of the heater (axial locations of 3.0 mm – 5.0 mm) accounted for 14.8% - 29.6%, 35.9% - 69.1% and 16.6% - 31.7% of total heat transfer.
- For the 60°C nominal heater temperature case, peak predicted perimeter averaged heat transfer coefficients ranged in magnitude from ~18 kW m^{-2} K^{-1} to ~ 339 kW m^{-2} K^{-1}. The peak Warrier et al. model value is ~0.2× that of the next lowest model, the Bertsch et al. model. Combined with its very poor RMS agreement, the Warrier et al. correlation likely predicts unrealistically low heat transfer coefficients. The Kim and Mudawar, and Lazarek

and Black models' peak values are ~3× higher than that predicted by the next highest model, the Agostini and Bontemps model. Combined with their relatively poor total RMS agreement, these correlations likely predict unrealistically high heat transfer coefficients. The perimeter-averaged single-phase heat transfer coefficients are nearly constant with a value of ~8,200 W m^{-2} K^{-1}.

- Uniformly increasing the single-phase heat transfer coefficient by a factor of 1.2 increased both single-phase and two-phase agreement for the Agostini and Bontemps model.
- The major mechanism of heat transfer in the presently modeled channels is nucleate boiling.
- Average predicted channel pressure drop for the 40°C, 50°C and 60°C nominal heater temperature cases were 37.8 ± 1.1 kPa, 58.7 ± 1.7 kPa and 66.1 ± 1.0 kPa, respectively. Total measured pressure drop increases at a faster rate than channel pressure drop, a fact attributed to a large pressure loss experienced during jetting of two-phase fluid from the channel exits.

The results of the current work show great promise that the design of future thermal managements systems can be aided by FEA and conjugate two-phase heat transfer modeling. Despite wide variations in predicted heat transfer coefficient, the predicted heat sink base temperature had good agreement with experimental results. This suggests that exact heat transfer coefficient values are relatively unimportant. While the current correlations may not be satisfactory for commercial implementation, the Agostini and Bontemps and the Bertsch et al. correlations, in particular, may be adequate for research purposes and initial heat exchanger design. It must be noted that the current work has evaluated a small sample size. Further comparison should be made with channels using different geometries, fluids and heat fluxes. Further experimental research

should be done with regards to both heat transfer and pressure drop in very small microchannels under the extreme heat fluxes and localized hotspots that are expected in future electronic components. As improved correlations are obtained, the current FEA model will be better able to examine a wide range of systems and save time and expense in the design of future thermal management systems.

References

[1] Karayiannis, T. G., and Mahmoud, M. M., 2017, "Flow Boiling in Microchannels: Fundamentals and Applications," Appl. Therm. Eng., **115**, pp. 1372–1397.

[2] Tuckerman, D. B., and Pease, R. F. W., 1981, "High-Performance Heat Sinking for VLSI," IEEE Electron Device Lett., **2**(5), pp. 126–129.

[3] Kandlikar, S. G., 2012, "History, Advances, and Challenges in Liquid Flow and Flow Boiling Heat Transfer in Microchannels: A Critical Review," J. Heat Transfer, **134**(3).

[4] Bandhauer, T. M., and Bevis, T. A., 2017, "High Heat Flux Boiling Heat Transfer For Laser Diode Arrays," *Proc. of ASME 2016 14th Int'l Conf. on Nanochannels, Microchannels, and Minichannels*, ASME, Washington, DC.

[5] Pais, M. R., Chow, L. C., and E.T., M., 1992, "Surface Roughness and Its Effects on the Heat Transfer Mechanism in Spray Cooling," J. Heat Transfer, **114**(1).

[6] Yan, Z., Zhao, R., Duan, F., Wong, T. N., Toh, K. C., Choo, K. F., Chan, P. K., and Chua, Y. S., 2011, "Spray Cooling," *Two Phase Flow, Phase Change and Numerical Modeling*, pp. 285–310.

[7] Bevis, T. A., 2016, "High Heat Flux Phase Change Thermal Management of Laser Diode Arrays," Colorado State University.

[8] Skidmore, J. A., Freitas, B. L., Crawford, J., Satariano, J., Utterback, E., DiMercurio, L., Cutter, K., and Sutton, S., 2000, "Silicon Monolithic Microchannel-Cooled Laser Diode Array," Appl. Phys. Lett., **77**(1), p. 10.

[9] Agostini, B., Fabbri, M., Park, J. E., Wojtan, L., Thome, J. R., and Michel, B., 2007, "State of the Art of High Heat Flux Cooling Technologies," Heat Transf. Eng., **28**(4), pp. 258–281.

[10] Hannemann, R., Joseph, M., and Pitasi, M., 2004, "Pumped Liquid Multiphase Cooling," *IMECE 2004*, pp. 3–7.

[11] Marcinichen, J. B., and Thome, J. R., 2010, "New Novel Green Computer Two-Phase Cooling Cycle: A Model for Its Steady-State Simulation," Proc. 23rd Int. Conf. Effic. Cost, Optim. Simulation, Environ. Impact Energy Syst. ECOS 2010, **3**(January).

[12] Pan, Z., Weibel, J. A., and Garimella, S. V, 2015, "A Cost-Effective Modeling Approach for Simulating Phase Change and Flow Boiling in Microchannels," *Proc. of ASME 2015 Int'l Technical Conf. and Exhibition on Packaging and Integration of Electronic and Photonic Microsystems*, San Francisco, CA, pp. 1–9.

[13] Mudawar, I., 2001, "Assessment of High-Heat-Flux Thermal Management Schemes," Components Packag. Technol. IEEE Trans., **24**(2), pp. 122–141.

[14] Tran, T. N., Wambsganss, M. W., and France, D. M., 1996, "Small Circular and Rectangular Channel Boiling with Two Refrigerants," Int. J. Multiph. Flow, **22**, pp. 485–498.

[15] Willingham, T. C., and Mudawar, I., 1992, "Forced-Convection Boiling and Critical Heat Flux from a Linear Array of Discrete Heat Sources," Int. J. Heat Mass Transf., **35**(11), pp. 2879–2890.

[16] Agostini, B., Thome, J. R., Fabbri, M., and Michel, B., 2008, "High Heat Flux Two-Phase Cooling in Silicon Multimicrochannels," IEEE Trans. Components Packag. Technol., **31**(3), pp. 691–701.

[17] Garimella, S. V, Yeh, L., and Persoons, T., 2012, "Thermal Management Challenges in Telecommunication Systems and Data Centers," Ieee Trans. Components, **2**(8), pp. 1307–

1316.
[18] Garimella, S. V, Persoons, T., Weibel, J., and Yeh, L. T., 2013, "Technological Drivers in Data Centers and Telecom Systems: Multiscale Thermal, Electrical, and Energy Management," Appl. Energy, **107**, pp. 66–80.
[19] Delforge, P., and Whitney, J., 2014, "Data Center Efficiency Assessment," Nat. Resour. Def. Counc., (August).
[20] Kim, S. M., and Mudawar, I., 2014, "Review of Databases and Predictive Methods for Heat Transfer in Condensing and Boiling Mini/Micro-Channel Flows," Int. J. Heat Mass Transf., **77**, pp. 627–652.
[21] Bertsch, S. S., Groll, E. A., and Garimella, S. V, 2009, "A Composite Heat Transfer Correlation for Saturated Flow Boiling in Small Channels," Int. J. Heat Mass Transf., **52**(7–8), pp. 2110–2118.
[22] Li, W., and Wu, Z., 2010, "A General Correlation for Evaporative Heat Transfer in Micro/Mini-Channels," Int. J. Heat Mass Transf., **53**(9–10), pp. 1778–1787.
[23] Thome, J. R., 2006, "State-of-the-Art Overview of Boiling and Two-Phase Flows in Microchannels," Heat Transf. Eng., **27**(9), pp. 4–19.
[24] Mishima, K., and Hibiki, T., 1996, "Some Characteristics of Air-Water Two-Phase Flow in Small Diameter Vertical Tubes," Int. J. Multiph. Flow, **22**(4), pp. 703–712.
[25] Triplett, K. A., Ghiaasiaan, S. M., Abdel-Khalik, S. I., and Sadowski, D. L., 1999, "Gas–liquid Two-Phase Flow in Microchannels Part I: Two-Phase Flow Patterns," Int. J. Multiph. Flow, **25**(3), pp. 377–394.
[26] Kew, P. A., and Cornwell, K., 1997, "Correlations for the Prediction of Boiling Heat Transfer in Small Diameter Channels," Appl. Therm. Eng., **17**, pp. 705–715.
[27] Kandlikar, S. G., and Grande, W. J., 2003, "Evolution of Microchannel Flow Passages - Thermohydraulic Performance and Fabrication Technology," Heat Transf. Eng., **24**(1), pp. 3–17.
[28] Mehendale, S. S., Jacobi, M. A., and Shah, R. K., 2000, "Fluid Flow and Heat Transfer at Micro- and Meso-Scales with Application to Heat Exchanger Design," Appl. Mech. Rev., **53**(7), pp. 175–193.
[29] Lazarek, G. M., and Black, S. H., 1982, "Evaporative Heat Transfer, Pressure Drop and Critical Heat Flux in a Small Vertical Tube with R-113," Int. J. Heat Mass Transf., **25**(7), pp. 945–960.
[30] Cooper, M. G., 1984, "Saturated Nucleate Pool Boiling – a Simple Correlation," *Proc. of the 1st UK National Heat Transfer Conference, IChemE Symposium*, pp. 785–793.
[31] Cooper, M. G., 1989, "Flow Boiling-the 'apparently Nucleate' Regime," Int. J. Heat Mass Transf., **32**(3), pp. 459–464.
[32] Liu, Z., and Winterton, R. H. S., 1991, "A General Correlation for Saturated and Subcooled Flow Boiling in Tubes and Annuli, Based on a Nucleate Pool Boiling Equation," Int. J. Heat Mass Transf., **34**(11), pp. 2759–2766.
[33] Kuznetsov, V. V., Shamirzaev, A. S., Kozulin, I. a., and Kozlov, S. P., 2013, "Correlation of the Flow Pattern and Flow Boiling Heat Transfer in Microchannels," Heat Transf. Eng., **34**(2–3), pp. 235–245.
[34] Cheng, P., Wu, H.-Y., and Hong, F.-J., 2007, "Phase-Change Heat Transfer in Microsystems," J. Heat Transfer, **129**(2), p. 101.
[35] Harirchian, T., and Garimella, S. V, 2010, "A Comprehensive Flow Regime Map for Microchannel Flow Boiling With Quantitative Transition Criteria," Int. J. Heat Mass

Transf., **53**, pp. 2694–2702.
[36] Harirchian, T., and Garimella, S. V, 2009, "The Critical Role of Channel Cross-Sectional Area in Microchannel Flow Boiling Heat Transfer," Int. J. Multiph. Flow, **35**, pp. 904–913.
[37] Harirchian, T., and Garimella, S. V, 2009, "Effects of Channel Dimension, Heat Flux, and Mass Flux on Flow Boiling Regimes in Microchannels," Int. J. Multiph. Flow, **35**(4), pp. 349–362.
[38] Thome, J. R., Bar-Cohen, A., Revellin, R., and Zun, I., 2013, "Unified Mechanistic Multiscale Mapping of Two-Phase Flow Patterns in Microchannels," Exp. Therm. Fluid Sci., **44**, pp. 1–22.
[39] Taitel, Y., 1990, "Flow Pattern Transitions in Two Phase Flow," *Proc. of the 9th International Heat Transfer Conference*.
[40] Rahim, E., Revellin, R., Thome, J., and Bar-Cohen, A., 2011, "Characterization and Prediction of Two-Phase Flow Regimes in Miniature Tubes," Int. J. Multiph. Flow, **37**(1), pp. 12–23.
[41] Akbar, M. K., Plummer, D. A., and Ghiaasiaan, S. M., 2003, "On Gas-Liquid Two-Phase Flow Regimes in Microchannels," Int. J. Multiph. Flow, **29**(5), pp. 855–865.
[42] Garimella, S. V, Coleman, J. W., and Killion, J. D., 2002, "An Experimental Validated Model for Two-Phase Pressure Drop in the Intermittent Flow Regime for Circular Channel," J. Fluids Eng., **124**, pp. 205–214.
[43] Harirchian, T., and Garimella, S. V, 2011, "Boiling Heat Transfer and Flow Regimes in Microchannels—A Comprehensive Understanding," J. Electron. Packag., **133**(1).
[44] Kim, S. M., and Mudawar, I., 2013, "Universal Approach to Predicting Saturated Flow Boiling Heat Transfer in Mini/Micro-Channels - Part I. Dryout Incipience Quality," Int. J. Heat Mass Transf., **64**, pp. 1226–1238.
[45] Kim, S. M., and Mudawar, I., 2013, "Universal Approach to Predicting Saturated Flow Boiling Heat Transfer in Mini/Micro-Channels - Part II. Two-Phase Heat Transfer Coefficient," Int. J. Heat Mass Transf., **64**, pp. 1239–1256.
[46] Wambsganss, M. W., France, D. M., Jendrzejczyk, J. A., and Tran, T. N., 1993, "Boiling Heat Transfer in a Horizontal Small-Diameter Tube," ASME J. Heat Transf., **115**, pp. 963–972.
[47] Tran, T. N., 1998, "Pressure Drop and Heat Transfer Study of Two-Phase Flow in Small Channels," Texas Tech University.
[48] Bao, Z. Y., Fletcher, D. F., and Haynes, B. S., 2000, "Flow Boiling Heat Transfer of Freon R11 and HCFC123 in Narrow Passages," Int. J. Heat Mass Transf., **43**, pp. 3347–3358.
[49] Bertsch, S. S., Groll, E. A., and Garimella, S. V, 2009, "Effects of Heat Flux, Mass Flux, Vapor Quality, and Saturation Temperature on Flow Boiling Heat Transfer in Microchannels," Int. J. Multiph. Flow, **35**(2), pp. 142–154.
[50] Wang, L., Chen, M., and Groll, M., 2009, "Flow Boiling Heat Transfer Characteristics of R134a in a Horizontal Mini Tube †," J. Chem. Eng. Data, **54**, pp. 2638–2645.
[51] Hamdar, M., Zoughaib, A., and Clodic, D., 2010, "Flow Boiling Heat Transfer and Pressure Drop of Pure HFC-152a in a Horizontal Mini-Channel ´ Bullition En e ´ Coulement et Transfert de Chaleur Lors de l ' e Chute de Pression Du HFC-152a Pur Dans Un Micro-Canal Horizontal," Int. J. Refrig., **33**(3), pp. 566–577.
[52] Mahmoud, M. M., Karayiannis, T. G., and Kenning, D. B. R., 2011, "Surface Effects in Flow Boiling of R134a in Microtubes," Int. J. Heat Mass Transf., **54**(15–16), pp. 3334–3346.

[53] Karayiannis, T. G., Mahmoud, M. M., and Kenning, D. B. R., 2012, "A Study of Discrepancies in Flow Boiling Results in Small to Microdiameter Metallic Tubes," Exp. Therm. Fluid Sci., **36**, pp. 126–142.
[54] Ali, R., Palm, B., and Maqbool, M. H., 2011, "Flow Boiling Heat Transfer Characteristics of a Minichannel up to Dryout Conditions," ASME J. Heat Transf., **133**.
[55] Huo, X., Chen, L., Tian, Y. S., and Karayiannis, T. G., 2004, "Flow Boiling and Flow Regimes in Small Diameter Tubes," Appl. Therm. Eng., **24**, pp. 1225–1239.
[56] Yun, R., Kim, Y., Soo, M., and Choi, Y., 2003, "Boiling Heat Transfer and Dryout Phenomenon of CO 2 in a Horizontal Smooth Tube," Int. J. Heat Mass Transf., **46**, pp. 2353–2361.
[57] Yun, R., Kim, Y., and Kim, M. S., 2005, "Convective Boiling Heat Transfer Characteristics of CO2 in Microchannels," Int. J. Heat Mass Transf., **48**, pp. 235–242.
[58] Agostini, B., Richard, J., Fabbri, M., Michel, B., Calmi, D., and Kloter, U., 2008, "High Heat Flux Flow Boiling in Silicon Multi-Microchannels – Part I : Heat Transfer Characteristics of Refrigerant R236fa," Int. J. Heat Mass Transf., **51**, pp. 5400–5414.
[59] Mastrullo, R., Mauro, A. W., Rosato, A., and Vanoli, G. P., 2009, "Carbon Dioxide Local Heat Transfer Coefficients during Flow Boiling in a Horizontal Circular Smooth Tube," Int. J. Heat Mass Transf., **52**(19–20), pp. 4184–4194.
[60] Sumith, B., Kaminaga, F., and Matsumura, K., 2003, "Saturated Flow Boiling of Water in a Vertical Small Diameter Tube," Exp. Therm. Fluid Sci., **27**(7), pp. 789–801.
[61] Qu, W., and Mudawar, I., 2003, "Flow Boiling Heat Transfer in Two-Phase Micro-Channel Heat Sinks—I. Experimental Investigation and Assessment of Correlation Methods," Int. J. Heat Mass Transf., **46**(15), pp. 2755–2771.
[62] Oh, H. K., and Son, C. H., 2011, "Evaporation Flow Pattern and Heat Transfer of R-22 and R-134a in Small Diameter Tubes," Heat Mass Transf. und Stoffuebertragung, **47**(6), pp. 703–717.
[63] Bang, K. H., Kim, K. K., Lee, S. K., and Lee, B. W., 2011, "Pressure Effect on Flow Boiling Heat Transfer of Water in Minichannels," Int. J. Therm. Sci., **50**(3), pp. 280–286.
[64] Yan, Y., and Lin, T., 1998, "Evaporation Heat Transfer and Pressure Drop of Refrigerant R-134a in a Small Pipe," Int. J. Heat Mass Transf., **41**, pp. 4183–4194.
[65] Lee, J., and Mudawar, I., 2005, "Two-Phase Flow in High-Heat-Flux Micro-Channel Heat Sink for Refrigeration Cooling Applications: Part I—pressure Drop Characteristics," Int. J. Heat Mass Transf., **48**(5), pp. 928–940.
[66] Saitoh, S., Daiguji, H., and Hihara, E., 2005, "Effect of Tube Diameter on Boiling Heat Transfer of R-134a in Horizontal Small-Diameter Tubes," Int. J. Heat Mass Transf., **48**, pp. 4473–4984.
[67] Wang, C.-C., Chiang, C.-S., and Yu, J.-G., 1998, "An Experimental Study of In-Tube Evaporation of R-22 inside a 6 . 5-Mm Smooth Tube," Int. J. Heat Fluid Flow, **19**, pp. 259–269.
[68] Greco, A., 2008, "Convective Boiling of Pure and Mixed Refrigerants : An Experimental Study of the Major Parameters Affecting Heat Transfer," Int. J. Heat Mass Transf., **51**, pp. 896–909.
[69] In, S., and Jeong, S., 2009, "Flow Boiling Heat Transfer Characteristics of R123 and R134a in a Micro-Channel," Int. J. Multiph. Flow, **35**(11), pp. 987–1000.
[70] Wu, J., Koettig, T., Franke, C., Helmer, D., Eisel, T., Haug, F., and Bremer, J., 2011, "Investigation of Heat Transfer and Pressure Drop of CO 2 Two-Phase Flow in a Horizontal

Minichannel," Int. J. Heat Mass Transf., **54**, pp. 2154–2162.
[71] Tibiriçá, C. B., Ribatski, G., and Thome, J. R., 2012, "Flow Boiling Characteristics for R1234ze(E) in 1.0 and 2.2 Mm Circular Channels," J. Heat Transfer, **134**.
[72] Agostini, B., and Bontemps, A., 2005, "Vertical Flow Boiling of Refrigerant R134a in Small Channels," Int. J. Heat Fluid Flow, **26**(2), pp. 296–306.
[73] Yu, W., France, D. M., Wambsganss, M. W., and Hull, J. R., 2002, "Two-Phase Pressure Drop, Boiling Heat Transfer, and Critical Heat Flux to Water in a Small-Diameter Horizontal Tube," Int. J. Multiph. Flow, **28**(6), pp. 927–941.
[74] Ducoulombier, M., Colasson, S., Bonjour, J., and Haberschill, P., 2011, "Carbon Dioxide Flow Boiling in a Single Microchannel - Part II: Heat Transfer," Exp. Therm. Fluid Sci., **35**(4), pp. 597–611.
[75] Warrier, G. R., Dhir, V. K., and Momoda, L. A., 2002, "Heat Transfer and Pressure Drop in Narrow Rectangular Channels," Exp. Therm. Fluid Sci., **26**(1), pp. 53–64.
[76] Owhaib, W., Martín-Callizo, C., and Palm, B., 2004, "Evaporative Heat Transfer in Vertical Circular Microchannels," Appl. Therm. Eng., **24**(8–9), pp. 1241–1253.
[77] Kim, S. M., and Mudawar, I., 2014, "Review of Databases and Predictive Methods for Pressure Drop in Adiabatic, Condensing and Boiling Mini/Micro-Channel Flows," Int. J. Heat Mass Transf., **77**, pp. 74–97.
[78] Zivi, S. M., 1964, "Estimation of Steady-State Steam Void-Fraction by Means of the Principle of Minimum Entropy Production," J. Heat Transfer, **86**(2), pp. 247–251.
[79] McAdams, W. H., Woods, W. K., and Heroman, L. C., 1942, "Vaporization inside Horizontal Tubes – II: Benzene–oil Mixture," Trans. ASME, **64**(3), pp. 193–200.
[80] Akers, W. W., Deans, H. A., and Crosser, O. K., 1958, "Condensing Heat Transfer within Horizontal Tubes," Chem. Eng. Prog., **54**(10), pp. 89–90.
[81] Cicchitti, A., Lombardi, C., Silvestri, M., Soldaini, G., and Zavalluilli, R., 1960, "Two-Phase Cooling Experiments-Pressure Drop, Heat Transfer and Burnout Measurements," Energ. Nucl., **7**, pp. 407–425.
[82] Dukler, A. E., Wicks, M., and Cleaveland, R. G., 1964, "Pressure Drop and Hold up in Two Phase Flow," AlChE J., **10**, pp. 38–51.
[83] Lin, S., Kwok, C. C. K., Li, R. Y., Chen, Z. H., and Chen, Z. Y., 1991, "Local Frictional Pressure Drop during Vaporization of R-12 through Capillary Tubes," Int. J. Multiph. Flow, **17**, pp. 95–102.
[84] Yang, C. Y., and Webb, R. ., 1996, "Friction Pressure Drop of R-12 in Small Hydraulic Diameter Extruded Aluminum Tubes with and without Micro-Fins," Int. J. Heat Mass Transf., **39**, pp. 801–809.
[85] Zhang, W., Hibiki, T., and Mishima, K., 2010, "Correlations of Two-Phase Frictional Pressure Drop and Void Fraction in Mini-Channel," Int. J. Heat Mass Transf., **53**, pp. 453–465.
[86] Tran, T. N., Chyu, M. C., Wambsganss, M. W., and France, D. M., 2000, "Two-Phase Pressure Drop of Refrigerants during Flow Boiling in Small Channels: An Experimental Investigation and Correlation Development," Int. J. Multiph. Flow2, **26**, pp. 1739–1754.
[87] Sun, L., and Mishima, K., 2009, "Evaluation Analysis of Prediction Methods for Two-Phase Flow Pressure Drop in Mini-Channels," Int. J. Multiph. Flow, **35**(1), pp. 47–54.
[88] Lockhart, R. W., and R.C. Martinelli, 1949, "Proposed Correlation of Data for Isothermal Two-Phase, Two-Component Flow in Pipes," Chem. Eng. Prog., (45), pp. 39–48.
[89] Kim, S. M., and Mudawar, I., 2013, "Universal Approach to Predicting Two-Phase

Frictional Pressure Drop for Mini/Micro-Channel Saturated Flow Boiling," Int. J. Heat Mass Transf., **58**(1–2), pp. 718–734.
[90] Yadigaroglu, G., 1981, "Two-Phase Flow Instabilities and Propagation Phenomena," *Thermohydraulics of Two-Phase Systems for Industrial Design and Nuclear Engineering*, J.M. Delhaye, M. Giot, and M.L. Riethmuller, eds., Hemispher, Washington, pp. 353–403.
[91] Bergles, A. E., 1977, "Review of Instability in Two-Phase Systems," *Two-Phase Flows and Heat Transfer*, S. Kakac, and F. Mayinger, eds., Hemisphere, Washington, pp. 383–422.
[92] Bergles, A. E., and Boure, J. A., 1973, "Review of Two-Phase Flow Instability," Nucl. Eng. Des., **25**, pp. 165–192.
[93] Mudawar, I., 2011, "Two-Phase Microchannel Heat Sinks: Theory, Applications, and Limitations," J. Electron. Packag., **133**(4), pp. 041002-1-041002-31.
[94] Peles, Y., Kuo, C.-J. J., and Peles, Y., 2008, "Flow Boiling Instabilities in Microchannels and Means for Mitigation by Reentrant Cavities," J. Heat Transfer, **130**(7), p. 72402.
[95] Hetsroni, G., Mosyak, A., Pogrebnyak, E., and Segal, Z., 2005, "Explosive Boiling of Water in Parallel Micro-Channels," Int. J. Multiph. Flow, **31**(4), pp. 371–392.
[96] Kandlikar, S. G., 2002, "Fundamental Issues Related to Flow Boiling in Minichannels and Microchannels," Exp. Therm. Fluid Sci., **26**(2–4), pp. 389–407.
[97] Saha, S. K., and Celata, G. P., 2015, *Critical Heat Flux in Flow Boiling in Microchannels*, Springer.
[98] Revellin, R., and Thome, J. R., 2008, "A Theoretical Model for the Prediction of the Critical Heat Flux in Heated Microchannels," Int. J. Heat Mass Transf., **51**(5–6), pp. 1216–1225.
[99] Riofrío, M. C., Caney, N., and Gruss, J.-A., 2016, "State of the Art of Efficient Pumped Two-Phase Flow Cooling Technologies," Appl. Therm. Eng., **104**, pp. 333–343.
[100] Bergles, A. E., and Kandlikar, S. G., 2005, "On the Nature of Critical Heat Flux in Microchannels," J. Heat Transfer, **127**, pp. 101–107.
[101] Kos¸ar, A., Kuo, C.-J. J., Peles, Y., Koşar, A., Kuo, C.-J. J., and Peles, Y., 2006, "Suppression of Boiling Flow Oscillations in Parallel Microchannels With Inlet Restrictors," ASME J. Heat Transf., **128**(3), pp. 251–260.
[102] Kandlikar, S. G., Kuan, W. K., Willistein, D. a., and Borrelli, J., 2006, "Stabilization of Flow Boiling in Microchannels Using Pressure Drop Elements and Fabricated Nucleation Sites," J. Heat Transfer, **128**(4), p. 389.
[103] Costa-Patry, E., Olivier, J., Michel, B., and Thome, J. R., 2011, "Two-Phase Flow of Refrigerants in 85 Mm-Wide Multi-Microchannels: Part II – Heat Transfer with 35 Local Heaters," Int. J. Heat Fluid Flow, **32**(2), pp. 464–476.
[104] Hamann, H. F., Weger, A., Lacey, J. A., Hu, Z., Cohen, E., and Wakil, J., 2007, "Hotspot-Limited Microprocessors: Direct Temperature and Power Distribution Measurements," IEEE J. Solid-State Circuits, **42**(1), pp. 56–65.
[105] Mahajan, R., Chiu, C. P., and Chrysler, G., 2006, "Cooling a Microprocessor Chip," Proc. IEEE, **94**(8), pp. 1476–1485.
[106] Costa-Patry, E., Nebuloni, S., Olivier, J., and Thome, J. R., 2012, "On-Chip Two-Phase Cooling with Refrigerant 85 Mm-Wide Multi-Microchannel Evaporator under Hot-Spot Conditions," IEEE Trans. Components, Packag. Manuf. Technol., **2**(2), pp. 311–320.
[107] Szczukiewicz, S., Magnini, M., and Thome, J. R., 2014, "Proposed Models, Ongoing Experiments, and Latest Numerical Simulations of Microchannel Two-Phase Flow Boiling," Int. J. Multiph. Flow, **59**, pp. 84–101.
[108] Hirt, C. W., and Nichols, B. D., 1981, "Volume of Fluid (VOF) Method for the Dynamics

of Free Boundaries," J. Comput. Physics1, **39**(1), pp. 201–225.
[109] Osher, S., and Fedkiw, R. P., 2001, "Level Set Methods: An Overview of Some Recent Results," J. Comput. Phys., **169**(2), pp. 463–502.
[110] Li, D., and Dhir, V. K., 2007, "Numerical Study of Single Bubble Dynamics During Flow Boiling," J. Heat Transfer, **129**(7), p. 864.
[111] Mukherjee, A., and Kandlikar, S. G., 2005, "Numerical Simulation of Growth of a Vapor Bubble during Flow Boiling of Water in a Microchannel," Microfluid. Nanofluidics, **1**(2), pp. 137–145.
[112] Zhuan, R., and Wang, W., 2012, "Flow Pattern of Boiling in Micro-Channel by Numerical Simulation," Int. J. Heat Mass Transf., **55**(5–6), pp. 1741–1753.
[113] Magnini, M., Pulvirenti, B., and Thome, J. R., 2013, "Numerical Investigation of Hydrodynamics and Heat Transfer of Elongated Bubbles during Flow Boiling in a Microchannel," Int. J. Heat Mass Transf., **59**(1), pp. 451–471.
[114] Magnini, M., Pulvirenti, B., and Thome, J. R., 2013, "Numerical Investigation of the Influence of Leading and Sequential Bubbles on Slug Flow Boiling within a Microchannel," Int. J. Therm. Sci., **71**, pp. 36–52.
[115] Zhang, P., and Jia, H. W., 2016, "Evolution of Flow Patterns and the Associated Heat and Mass Transfer Characteristics during Flow Boiling in Mini-/Micro-Channels," Chem. Eng. J., **306**, pp. 978–991.
[116] Mukherjee, A., Kandlikar, S. G., and Edel, Z. J., 2011, "Numerical Study of Bubble Growth and Wall Heat Transfer during Flow Boiling in a Microchannel," Int. J. Heat Mass Transf., **54**(15–16), pp. 3702–3718.
[117] Tibiriçá, C. B., and Ribatski, G., 2014, "Flow Patterns and Bubble Departure Fundamental Characteristics during Flow Boiling in Microscale Channels," Exp. Therm. Fluid Sci., **59**, pp. 152–165.
[118] Wu, H. L., Peng, X. F., Ye, P., and Gong, Y. E., 2007, "Simulation of Refrigerant Flow Boiling in Serpentine Tubes," Int. J. Heat Mass Transf., **50**, pp. 1186–1195.
[119] Fang, C., David, M., Rogacs, A., and Goodson, K., 2010, "Volume of Fluid Simulation of Boiling Two-Phase Flow in a Vapor-Venting Microchannel," Frotiers Heat Mass Transf.
[120] Sun, D., Xu, J., and Chen, Q., 2014, "Modeling of the Evaporation and Condensation Phase-Change Problems with FLUENT," Numer. Heat Transf. B, **66**, pp. 326–342.
[121] Kunkelmann, C., and Stephan, P., 2009, "CFD Simulation of Boiling Flows Using the Volume-of-Fluid Method within OpenFOAM," Numer. Heat Transf. A, **56**, pp. 631–346.
[122] Kunkelmann, C., Ibrahem, K., Schweizer, N., Herbert, S., Stephan, P., and Gambaryan-Roisman, T., 2012, "The Effect of Three-Phase Contact Line Speed on Local Evaporative Heat Transfer: Experimental and Numerical Investigations," Int. J. Heat Mass Transf., **55**, pp. 1896–1904.
[123] Ganapathy, H., Shooshtari, A., Choo, K., Dessiatoun, S., Alshehhi, M., and Ohadi, M., 2013, "Volume of Fluid-Based Numerical Modeling of Condensation Heat Transfer and Fluid Flow Characteristics in Microchannels," Int. J. Heat Mass Transf., **65**(62–72).
[124] Hardt, S., and Wondra, F., 2008, "Evaporation Model for Interfacial Flows Based on a Continuum-Field Representation of Source Terms," J. Comput. Phys., **227**, pp. 5871–5895.
[125] Knupp, D. C., Naviera Cotta, C. P., and Cotta, R. M., 2012, "Conjugated Heat Transfer in Micro-Channels with a Single Domain Formulation and Integral Transforms," *Proc. of ASME 2012 3rd Micro/Nanoscale Heat and Mass Transfer Conference*, Atlanta, GA.
[126] Knupp, D. C., Cotta, R. M., and Naveira Cotta, C. P., 2013, "Conjugated Heat Transfer in

Heat Spreaders with Micro-Channels," *Proc. of ASME 2013 Heat Transfer Summer Conference*.
[127] Tiwari, N., Moharana, M. K., and Sarangi, S. K., 2016, "Conjugate Heat Transfer in Single-Phase Wavy Microchannel," Proc. ASME 2016 5th Int'l Conf. Micro/Nanoscale Heat Mass Transf., pp. 1–8.
[128] Nunes, J. S., Cotta, R. M., Avelino, M. R., and Kakac, S., 2010, "Conjugated Heat Transfer in Microchannels," *Microfluidics Based Microsystems: Fundamentals and Applications*, pp. 61–82.
[129] Pellicone, D., Ortega, A., del Valle, M., and Schon, S., 2011, "Simulation of Two-Phase Flow and Heat Transfer in Mini-and Micro-Channels for Concentrating Photovoltaics Cooling," *ASME 2011 5th International Conference on Energy Sustainability*, pp. 1957–1965.
[130] Tillner-Roth, R., and Baehr, H. D., 1994, "An International Standard Formulation for the Thermodynamic Properties of 1,1,1,2-Tetrafluoroethane (HFC-134a) for Temperatures from 170 K to 455 K and Pressures up to 70 MPa," J. Phys. Chem., **23**(5).
[131] Chen, J. C., 1966, "Correlation for Boiling Heat Transfer to Saturated Fluids in Convective Flow," I&EC Process Des. Dev., **5**(3), pp. 322–329.
[132] Hausen, H., 1943, "Darstellung Des Wärmeüberganges in Rohren Durch Verallgemeinerte Potenzbeziehungen," Z. VDI Beih. Verfahrenstechnik, **4**, pp. 91–102.
[133] Agostini, B., Bontemps, A., Watel, B., and Thonon, B., 2003, "Boiling Heat Transfer in Mini-Channels: Influence of the Hydraulic Diameter," *Proceedings of the International Congress of Refrigeration*.
[134] Agostini, B., Thome, J. R., Fabbri, M., Michel, B., Calmi, D., and Kloter, U., 2008, "High Heat Flux Flow Boiling in Silicon Multi-Microchannels: Part II. Heat Transfer Characteristics of Refrigerant R245fa," Int. J. Heat Mass Transf., **51**, pp. 5415–5425.
[135] Bertsch, S. S., Groll, E. A., and Garimella, S. V, 2008, "Refrigerant Flow Boiling Heat Transfer in Parallel Microchannels as a Function of Local Vapor Quality," Int. J. Heat Mass Transf., **51**(19–20), pp. 4775–4787.
[136] Chen, T., and Garimella, S. V, 2006, "Measurements and High-Speed Visualizations of Flow Boiling of a Dielectric Fluid in a Silicon Microchannel Heat Sink," Int. J. Multiph. Flow, **32**, pp. 957–971.
[137] Harirchian, T., and Garimella, S. V, 2008, "Microchannel Size Effects on Local Flow Boiling Heat Transfer to a Dielectric Fluid," Int. J. Heat Mass Transf., **51**, pp. 3724–3735.
[138] Lee, H. J., and Lee, S. Y., 2001, "Heat Transfer Correlation for Boiling Flows in Small Rectangular Horizontal Channels with Low Aspect Ratios," Int. J. Multiph. Flow, **27**, pp. 2043–2062.
[139] Lin, S., Kew, P. A., and Cornwell, K., 2001, "Two-Phase Heat Transfer to a Refrigerant in a 1mm Diameter Tube," Int. J. Refrig., **24**, pp. 51–56.
[140] Qi, S. L., Zhang, P., Wang, R. Z., and Xu, L. X., 2007, "Flow Boiling of Liquid Nitrogen in Micro-Tubes: Part II. Heat Transfer Characteristics and Critical Heat Flux," Int. J. Heat Mass Transf., **50**, pp. 5017–5030.
[141] Tran, T. N., Wambsganss, M. W., and France, D. M., 1996, "Small Circular- and Rectangular-Channel Boiling with Two Refrigerants," Int. J. Multiph. Flow, **22**(3), pp. 485–498.
[142] Yun, R., Heo, J. H., and Kim, Y., 2006, "Evaporative Heat Transfer and Pressure Drop ofR410A in Microchannels," Int. J. Refrig., **29**, pp. 92–100.

[143] Schrock, V. ., and Grossman, L. ., 1962, "Forced Convection Boiling in Tubes," Nucl. Sci. Eng., **12**(4), pp. 474–482.
[144] Yan, Y. Y., and Lin, T. F., 1998, "Evaporation Heat Transfer and Pressure Drop of Refrigerant R-134a in a Small Pipe," Int. J. Heat Mass Transf., **41**, pp. 4183–4194.
[145] Muwanga, R., and Hassan, I., 2007, "A Flow Boiling Heat Transfer Investigation of FC-72 in a Microtube Using Liquid Crystal ThermographyNo Title," J. Heat Transfer, **129**, pp. 977–987.
[146] Zhao, X., and Bansal, P. K., 2007, "Flow Boiling Heat Transfer Characteristics," Int. J. Refrig., **30**, pp. 937–945.
[147] Consolini, L., 2008, "Convective Boiling Heat Transfer in a Single Micro-Channel," École Polytechnique Fédérale De Lausanne.
[148] Ohta, H., Inoue, K., Ando, M., and Watanabe, K., 2009, "Experimental Investigation on Observed Scattering in Heat Transfer Characteristics for Flow Boiling in a Small Diameter Tube," Heat Transf. Eng., **30**, pp. 19–27.
[149] Ducoulombier, M., 2010, "Ébullition Convective Du Dioxyde de Carbone – Étude Expérimentale En Micro-Canal," nstitut National des Sciences Appliquées (INSA) de Lyon.
[150] Martín-Callizo, C., "Flow Boiling Heat Transfer in a Single Vertical Channel of Small Diameter."
[151] Ong, C. L., 2010, "Macro-to-Microchannel Transition in Two-Phase Flow and Evaporation," École Polytechnique Fédérale De Lausanne.
[152] Tibiriçá, C. B., and Ribatski, G., 2010, "Flow Boiling Heat Transfer of R134a and R245fa in a 2.3 Mm Tube," Int. J. Heat Mass Transf., **53**, pp. 2459–2468.
[153] Copetti, J. B., Macagnan, M. H., Zinani, F., and Kunsler, N. L. F., 2011, "Flow Boiling Heat Transfer and Pressure Drop of R-134a in a Mini Tube: An Experimental Investigation," Exp. Therm. Fluid Sci., **35**, pp. 636–644.
[154] Oh, H. K., and Son, C. H., 2011, "Flow Boiling Heat Transfer and Pressure Drop Characterisitics of CO2 in Horizontal Tube of 4.57-Mm Inner Diameter," Appl. Therm. Eng., **31**, pp. 163–172.
[155] Li, M., Dang, C., and Hihara, E., 2012, "Flow Boiling Heat Transfer of HFO12234yf and R32 Refrigerant Mixtures in a Smooth Horizontal Tube: Par I. Experimental Investigation," Int. J. Heat Mass Transf., **55**, pp. 3437–3446.
[156] Kim, S. M., and Mudawar, I., 2012, "Consolidated Method to Predicting Pressure Drop and Heat Transfer Coefficient for Both Subcooled and Saturated Flow Boiling in Micro-Channel Heat Sinks," Int. J. Heat Mass Transf., **55**(13–14), pp. 3720–3731.
[157] Copeland, D., 1995, "Manifold Microchannel Heat Sinks: Analysis and Optimization," *ASME/JSME Thermal Engeering*, pp. 169–174.
[158] Shah, R. K., and London, A. L., 1978, *Laminar Flow Forced Convection in Ducts*, Academic Press.
[159] Lee, P.-S., and Garimella, S. V, 2008, "Saturated Flow Boiling Heat Transfer and Pressure Drop in Silicon Microchannel Arrays," Int. J. Heat Mass Transf., **51**(3–4), pp. 789–806.
[160] Shah, R., and London, A., 2014, *Laminar Flow Forced Convection in Ducts: A Source Book for Compact Heat Exchanger Analytical Data*, Academic Press, New York, NY.
[161] Churchill, S. W., 1977, *Friction-Factor Equation Spans All Fluid Flow Regimes*.
[162] Crane Co, 1979, "Flow of Fluids through Valves, Fittings and Pipes."
[163] 1962, *Pipe Friction Manual*, Hydraulic Institute, New York, NY.
[164] Bergman, T. L., Lavine, A. S., Incropera, F. P., and DeWitt, D. P., 2011, *Fundamentals of*

Heat and Mass Transfer, John Wiley & Sons.
[165] Dittus, F. W., and Boelter, L. M. K., 1985, "Heat Transfer in Automobile Radiators of the Tubular Type," Int. Commun. Heat Mass Transf., **12**(1), pp. 3–22.
[166] Incropera, F. P., Dewitt, D. P., Bergman, T. L., and Lavine, A. S., 2007, *Fundamentals of Heat Mass Transfer*, John Wiley & Sons.

Appendix A: Experiment Energy Balance

An energy balance between the inlet and outlet temperature sensors has been performed to quantify heat transfer to and from the surroundings. This section of the test loop is divided into seven regions for the purposes of these calculations and is modeled in Figure A-1 from Bevis [7]. Regions 1 and 7 consist of PTFE tube encased in a stainless-steel braid and further insulated by a layer of Buna-N foam rubber. Regions 2 and 6 are sight tubes made of a Teflon/PTFE blend. Regions 3 and 5 are inside the PEEK interface block and Region 4 is the actual test section.

Figure A-2a shows a cross-section of Regions 1 and 7. Since the thickness of the PTFE tubing is not known, it is lumped in with stainless-steel. Because stainless-steel has a higher thermal conductivity, this simplification that will overpredict heat transfer and yield a conservative estimate. The inner and outer stainless-steel diameters, D_1 and D_2, are 6.4 mm and 9.5 mm, respectively. The outer diameter of the Buna-N insulation, D_3, is 47.6 mm. A thermal resistance network for the setup is shown in Figure A-2b. The thermal resistances that must be considered are the convection from the fluid to the stainless-steel tubing (R_{fluid}), conduction through the stainless-steel (R_{ss}), conduction through the Buna-N insulation (R_{ins}), and both convection and

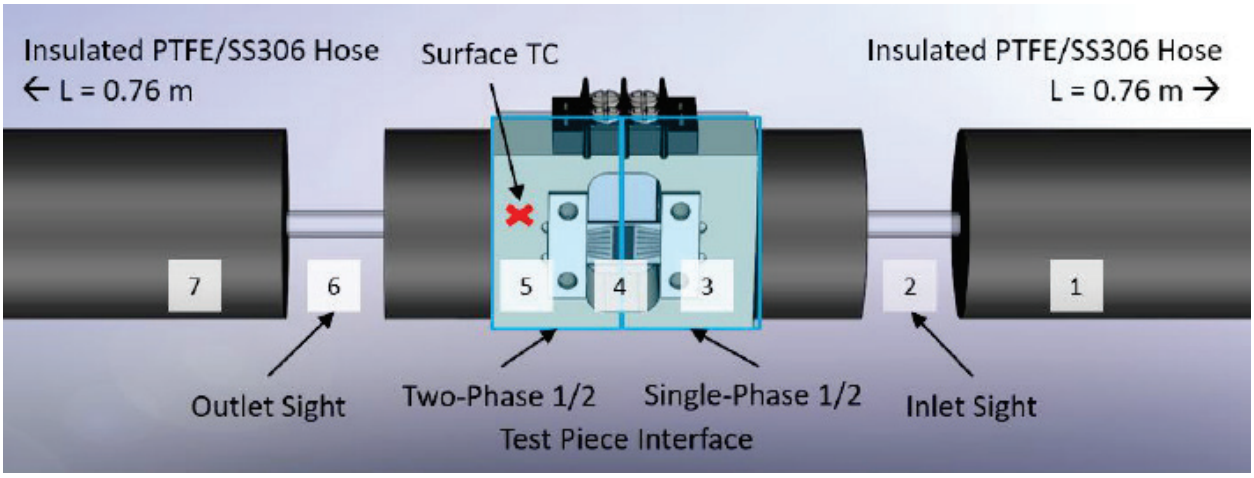

Figure A-1: Schematic use for energy balance [7]. Fluid travels from left to right.

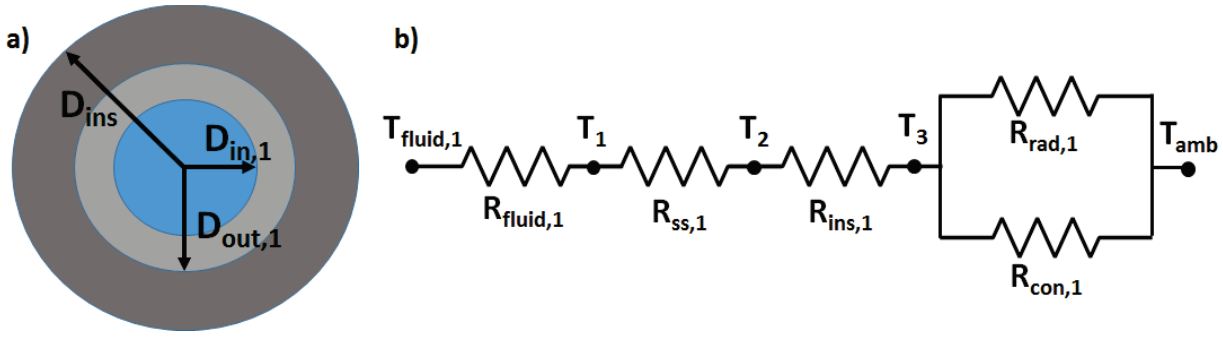

Figure A-2: (a) Cross-section of Regions 1 and 7 show the fluid (blue), stainless-steel (light grey) and Buna-N insulation (dark grey) and (b) representative thermal resistance network.

radiation between the insulation and the ambient air ($R_{a,con}$, $R_{a,rad}$). Once the individual resistances are found, the equivalent resistance can be calculated as follows:

$$R_{eq,1} = R_{fluid,1} + R_{ss} + R_{ins} + \frac{R_{con,1}R_{rad,1}}{R_{con,1} + R_{rad,1}} \tag{F.1}$$

Convection resistance between the fluid and stainless-steel tube is calculated as follows:

$$R_{fluid,1} = \frac{1}{h_{fluid,1}A_{s,1}} \tag{F.2}$$

where the heat transfer coefficient can be calculated using the Dittus-Boelter [165] equation:

$$h = \left(\frac{k}{D}\right)0.023Re^{4/5}Pr^{2/5} \tag{F.3}$$

It is assumed that the fluid temperature remains at the inlet temperature, which for the sample case is 284.7 K. The fluid inlet pressure is 633 kPa. The thermal conductivity of R-134a at this temperature and pressure is 0.0897 W m^{-1} K^{-1}, the Prandtl number is 3.53 and the fluid density is 1257 kg m^{-3}. For the given mass flow rate of 0.0997 kg min^{-1}, the fluid velocity can be found as follows:

$$u = \frac{4\dot{m}}{\pi\rho D^2} \tag{F.4}$$

$$u_1 = \frac{4\left(0.0997\ \frac{\text{kg}}{\text{min}}\right)\left(\frac{1\text{min}}{60\ \text{s}}\right)}{\pi\left(1257\ \frac{\text{kg}}{\text{m}^3}\right)\left(0.00635\ \text{m}\right)^2} = 0.042\ \frac{\text{m}}{\text{s}} \tag{F.5}$$

The Reynolds number is

$$\mathrm{Re}_1 = \frac{\rho u D}{\mu} = \frac{\left(1257\,\frac{\mathrm{kg}}{\mathrm{m}^3}\right)\left(0.042\,\frac{\mathrm{m}}{\mathrm{s}}\right)\left(0.00635\ m\right)}{0.000234\,\frac{kg}{m\cdot s}} = 1446 \tag{F.6}$$

and from Equation (F.3) I find

$$h_{\mathrm{fluid},1} = \left(\frac{0.0897\,\frac{W}{m\cdot K}}{.00635\ m}\right)0.023\left(1446\right)^{4/5}\left(3.53\right)^{2/5} = 181.5\,\frac{W}{m^2 K} \tag{F.7}$$

The length of this section is 0.76 m, giving a surface area of

$$A_{\mathrm{s},1} = \pi D L = \pi\left(0.00635\ m\right)\left(0.76\ m\right) = 0.0152\ m^2 \tag{F.8}$$

so the convection thermal resistance from Equation (F.2) is

$$R_{\mathrm{fluid},1} = \frac{1}{\left(181.5\,\frac{W}{m^2 K}\right)\left(0.0152\ m^2\right)} = 0.362\,\frac{K}{W} \tag{F.9}$$

The next resistance in the thermal circuit is the conduction resistance through the stainless-steel wall which can be found using

$$R = \frac{\ln\left(D_{\mathrm{out}} \big/ D_{\mathrm{in}}\right)}{2\pi\left(D_{\mathrm{out}} - D_{\mathrm{in}}\right)k} \tag{F.10}$$

We assume that the stainless-steel is at the fluid temperature and so has a thermal conductivity of 13.2 W m^{-1} K^{-1}. Equation (F.10) then gives .

$$R_{\mathrm{ss},1} = \frac{\ln\left(0.00953 \big/ 0.00635\right)}{2\pi\left(0.00953\ m - 0.00635\ m\right)\left(13.2\,\frac{W}{mK}\right)} = 1.54\,\frac{K}{W} \tag{F.11}$$

The thermal resistance of the insulation can be determined in a similar manner. The thermal conductivity of the Buna-N is 0.036 W m^{-1} K^{-1} and the diameters involve are $D_{\mathrm{in},1}$ and $D_{\mathrm{out},1,}$ giving a thermal resistance of $R_{\mathrm{ins},1}$ = 186.7 K W^{-1}. The convective thermal resistance between the insulation and the ambient air using the following heat transfer coefficient correlation for natural convection around a horizontal cylinder [166]:

$$h = \left(\frac{k}{D}\right)\left[0.6 + \frac{0.387 Ra^{1/6}}{\left(1+\left(\frac{0.559}{Pr}\right)^{9/16}\right)^{8/27}}\right]^2 \tag{F.12}$$

The Prandtl number for the ambient air at a temperature of 295.4 K and atmospheric pressure is 0.71 and the Rayleigh number is given by

$$Ra = \frac{g\beta D^3 \left|T - T_{\text{amb}}\right|}{\nu\alpha} \tag{F.13}$$

where β is the inverse of the film temperature. Since T_3 is unknown, I make an initial guess of 294.6 K, which gives a film temperature of 295 K. Once the total rate of heat transfer is found, T_3 can be recalculated and the process can be repeated if necessary. At the assumed film temperature and atmospheric pressure, the kinematic viscosity of air is 1.63×10^{-5} m^2 s^{-1}, the thermal diffusivity is 2.31×10^{-5} m^2 s^{-1} and the thermal conductivity is 0.026 W m^{-1} K^{-1}. From Equation (F.13) the Rayleigh number is 9,060:

$$Ra = \frac{\left(9.81\frac{m}{s^2}\right)\left(\frac{1}{295\ K}\right)\left(.0476\ m\right)^3\left|294.6\ K - 295.4\ K\right|}{\left(1.63\times10^{-5}\frac{m^2}{s}\right)\left(2.31\times10^{-5}\frac{m^2}{s}\right)} = 9{,}060 \tag{F.14}$$

Plugging all of these values into Equation (F.12) then yields a heat transfer coefficient of 2.33 W m^{-2} K^{-1}:

$$h = \left(\frac{0.026\frac{W^2}{mK}}{0.0476\ m}\right)\left[0.6 + \frac{0.387\left(9060\right)^{1/6}}{\left(1+\left(\frac{0.559}{0.71}\right)^{9/16}\right)^{8/27}}\right]^2 = 2.33\frac{W}{m^2K} \tag{F.15}$$

The outer surface area of the insulation is 0.114 m^2, giving a convective thermal resistance of $R_{\text{con},1}$ = 3.77 K W^{-1}.

The radiation resistance is also calculated by guessing a surface temperature. The radiative heat transfer coefficient is given by

$$h = \varepsilon\sigma\left(T + T_{\text{amb}}\right)\left(T^2 + T_{\text{amb}}{}^2\right) \tag{F.16}$$

where the emissivity (ε) is taken to be 1 and the Stefan-Boltzmann constant (σ) is 5.67×10^{-8} W m^{-2} K^{-4}. This gives a heat transfer coefficient of 5.73 W m^{-2} K^{-1} and a radiation thermal resistance of 1.51 K W^{-1}. Returning to Equation (F.1), the equivalent thermal resistance is

$$R_{\text{eq},1} = 0.362\,\tfrac{K}{W} + 1.54\,\tfrac{K}{W} + 186.7\,\tfrac{K}{W} + \frac{\left(3.77\,\tfrac{K}{W}\right)\left(1.51\,\tfrac{K}{W}\right)}{3.77\,\tfrac{K}{W} + 1.51\,\tfrac{K}{W}} = 189.7\,\tfrac{K}{W} \tag{F.17}$$

With the equivalent thermal resistance, the total heat transfer in Region 1 can be determined as follows:

$$q_1 = \frac{T_{amb} - T_{\text{fluid}}}{\text{R}_{\text{eq}}} = \frac{\left(295.4 - 284.7\right)[K]}{189.7\,\tfrac{K}{W}} = 0.06\ W \tag{F.18}$$

Now that I have q_1, I can reevaluate the value of the T_3. The equivalent convective resistance between the insulation and ambient air is 1.09 K W^{-1}, which gives an insulation surface temperature of T_3 = 295.3 K. Iterating through the process again, the heat transfer rate is still found to be 0.06 W. The heat transfer rate in Region 7 is calculated similarly, except the fluid and stainless-steel temperatures are assumed to be at the measured outlet fluid temperature of 285.2 K and the fluid pressure is the outlet pressure of 596.1 kPa yielding a heat transfer rate of q_7 = 0.05 W.

The next regions to be evaluated are Regions 2 and 6. The thermal resistance network for Region 2 is shown in Figure A-3. As in Region 1, I consider convection between the fluid and the tube wall and conduction through the tube wall—which in this case is PTFE. Since there is no extra layer of insulation, I then just consider convection and radiation between the outer tube wall and the ambient air. The small amount of heat absorbed in Region 1 raises has a negligible effect on fluid temperature, so I again assume the fluid is at the inlet temperature of 284.7 K. The tube

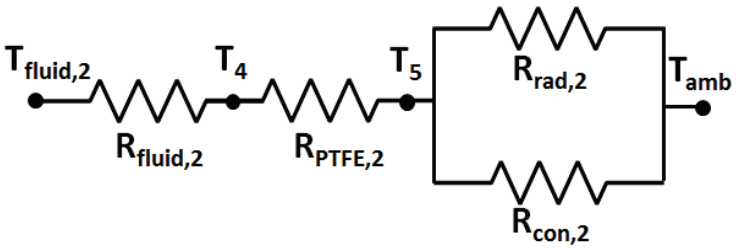

Figure A-3:Thermal resistance network for Region 2.

in this section has an inner diameter of 3.97 mm, an outer diameter of 6.35 mm and a length of 0.076 m. This yields a fluid velocity of 0.107 m s-1, a Reynolds number of 2277, and via Equation (F.3), a convective heat transfer coefficient of 417.6 W m^{-2} K^{-1}. With an inner surface area of 9.5 × 10^{-4} m^2, the inner convective thermal resistance is 2.5 K W^{-1}.

The conduction thermal resistance through the PTFE tube wall is found Equation (F.10). The thermal conductivity of PTFE is 0.25 W m^{-1} K^{-1}, giving a conductive thermal resistance of 125.6 K W^{-1}. For the natural convection thermal resistance, I initially assume the PTFE outer surface temperature is 293 K, which gives a film temperature of 294.3 K. Equation (F.12) then yields a heat transfer coefficient of 6.35 W m^{-2} K^{-1} and the convective thermal resistance is calculated from Equation (F.2) as 103.9 K W^{-1}. I calculate the radiation heat transfer coefficient using the same method as before and find a value of 5.78 W m^{-2} K^{-1}, yielding a thermal resistance of 114.1 K W^{-1}. The equivalent thermal resistance for Region 2 is

$$R_{eq,2} = 2.5\frac{K}{W} + 125.6\frac{K}{W} + \frac{\left(103.9\frac{K}{W}\right)\left(114.1\frac{K}{W}\right)}{103.9\frac{K}{W} + 114.1\frac{K}{W}} = 182.5\frac{K}{W} \quad \text{(F.19)}$$

The associated heat transfer rate, q_2, is 0.06 W. The outer surface temperature of the PTFE is recalculated to be 292.3 K. The heat transfer rate is then recalculated using this value and found to still be 0.06 W. The heat transfer rate for Region 6 is calculated in the same manner, though the PTFE is assumed to be at the outlet fluid temperature. Because PTFE thermal conductivity is fairly insensitive to temperature, the heat transfer rate for Region 6 is also q_6 = 0.06 W.

Due to the complex geometry of the PEEK interface block, it is difficult to determine the heat transfer rate for Regions 3 and 5 by constructing a thermal resistance network from the fluid to the ambient air. Instead, a surface thermocouple measured the PEEK temperature to be 288.1 K at the location of the red 'x' in Figure A-1. I assume that the entire PEEK block surface is at this temperature and consider convective and radiative heat transfer from both the vertically and horizontally oriented surfaces. Making this assumption, I can combine Regions 3 and 5 into one. The thermal resistance network for the combined section is shown in Figure A-4.

The natural convective heat transfer coefficient for the vertical portion can be determined using [166]:

$$h = \left(\frac{k}{L}\right)\left[0.68 + \frac{0.670 Ra^{1/4}}{\left(1+\left(\frac{0.492}{Pr^{9/16}}\right)\right)^{4/9}}\right] \tag{F.20}$$

where the characteristic length is the height of the PEEK block and has a value of L = 0.05 m. For the film temperature of 291.9 K, the Rayleigh number is 97,977, the Prandtl number is 0.71 and the thermal conductivity is 0.026 W m^{-1} K^{-1}. This gives a heat transfer coefficient of 5.31 W m^{-2} K^{-1} and, for the total vertical surface area of 7.66 × 10^{-3} m^2, a thermal resistance of 24.6 K W^{-1}. The radiative heat transfer rate for the vertical portion is calculated as before, yielding a heat transfer coefficient of 5.64 W m^{-2} K^{-1} and a thermal resistance of 23.2 K W^{-1}.

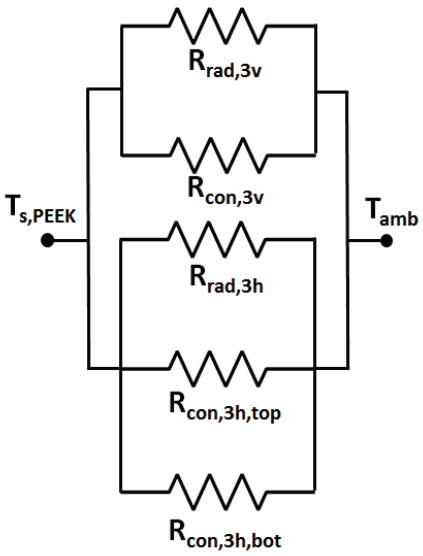

Figure A-4: Thermal resistance network for Regions 3 and 5.

Natural convection for the horizontal surfaces must be calculated separately for the top and bottom of the PEEK.

The heat transfer coefficients for the upper and lower surfaces can be found using Equations (F.21) and (F.22), respectively [166].

$$h = \left(\frac{k}{L}\right)\left(0.27Ra^{1/4}\right) \tag{F.21}$$

$$h = \left(\frac{k}{L}\right)\left(0.54Ra^{1/4}\right) \tag{F.22}$$

For the characteristic length of L = 0.05 m and the film temperature of 291.9 K, the Rayleigh number is 97,977 and the heat transfer coefficients for the upper and lower surfaces are 2.46 W m^{-2} K^{-1} and 4.93 W m^{-2} K^{-1}, respectively. Each surface has a surface area of 7.84 × 10^{-4} m^2 which gives thermal resistances of 517.9 K W^{-1} and 259.0 K W^{-1}, respectively. Radiation heat transfer rates are calculated as before giving a radiation heat transfer coefficient and thermal resistance for the combined vertical surfaces of 5.64 W m^{-2} K^{-1} and 113.1 K W^{-1}, respectively. The total equivalent thermal resistance for heat transfer to the PEEK block is found from the following equation:

$$R_{\text{eq},1} = \left(\frac{1}{R_{\text{rad,3v}}} + \frac{1}{R_{\text{con,3v}}} + \frac{1}{R_{\text{rad,3h}}} + \frac{1}{R_{\text{con,3h,top}}} + \frac{1}{R_{\text{con,3h,bot}}}\right)^{-1} = 6.7\frac{K}{W} \tag{F.23}$$

The overall total heat transfer rate is 1.12 W.

The last region through which heat transfer with the environment can occur is in Region 4, the portion of the test section not in contact with the PEEK interface block. In reality, the ceramic electrical harness insulates much of this region, but this insulation is ignored to calculate a conservative heat loss through the region. An argument for negligible heat transfer through the glass surface of the test section is presented in Section 4.1.4. Additionally, the majority of the test section is at the ambient temperature, a fact established by pyrometer temperature measurements at the channel extremes. The exception to this is region immediately surrounding the heater. To account for this, I assume the entire channel backside region is at an average temperature. Based

on an estimate using the Agostini and Bontemps model for the sample case, an average temperature of 312.9 K is used. The total surface area for the channel backside region is 5.0×10^{-5} m^2 (5 mm × 10 mm). I must consider both convective and radiative heat transfer. The convective heat transfer coefficient can be calculated using Equation (F.20). For the film temperature of 304.3 K and the characteristic length of 0.01 m, the thermal conductivity of air is 0.027 W m^{-1} K^{-1}, the Rayleigh number is 1506, the heat transfer coefficient is 10.86 W m^{-2} K^{-1} and the thermal resistance is 1841.0 K W^{-1}. The radiative heat transfer coefficient and thermal resistance are calculated in the usual way giving values of 6.39 W m^{-2} K^{-1} and 3129.3 K W^{-1}, respectively. This equates to a total equivalent resistance of 1159.1 K W^{-1} and a heat transfer rate -0.01 W, where the negative sign indicates heat loss to the environment.

Table A-1: Summary results for energy balance.

Section 1		Section 2		Sections 3 & 5		Section 4	
$T_{fluid,1}$ [C]	11.5	$T_{fluid,2}$ [C]	11.5	$T_{s,PEEK}$ [C]	14.9	$T_{backside,4}$ [C]	39.7
T_1 [C]	11.5	T_4 [C]	11.7	T_{amb} [C]	22.4	T_{amb} [C]	22.4
T_2 [C]	11.6	T_5 [C]	19.2	$R_{rad,3v}$ [K W^{-1}]	14.9	$R_{rad,4}$ [K W^{-1}]	3129.3
T_3 [C]	22.2	T_{amb} [C]	22.4	$R_{con,3v}$ [K W^{-1}]	14.8	$R_{con,4}$ [K W^{-1}]	1841.0
T_{amb} [C]	22.4	$R_{fluid,2}$ [K W^{-1}]	2.5	$R_{rad,3h}$ [K W^{-1}]	113.1	$R_{eq,4}$ [K W^{-1}]	1159.1
$R_{fluid,1}$ [K W^{-1}]	0.4	$R_{PTFE,2}$ [K W^{-1}]	125.6	$R_{con,3h,top}$ [K W^{-1}]	517.9	q_4 [W]	-0.01
$R_{ss,1}$ [K W^{-1}]	1.5	$R_{rad,1}$ [K W^{-1}]	114.1	$R_{con,3h,bot}$ [K W^{-1}]	259.0		
$R_{ins,1}$ [K W^{-1}]	186.7	$R_{con,1}$ [K W^{-1}]	103.9	$q_{3/5}$ [W]	1.12		
$R_{rad,1}$ [K W^{-1}]	1.5	$R_{eq,1}$ [K W^{-1}]	182.5				
$R_{con,1}$ [K W^{-1}]	3.8	q_2 [W]	0.06				
$R_{eq,1}$ [K W^{-1}]	189.7						
q_1 [W]	0.06						

Section 6		Section 7	
$T_{fluid,6}$ [C]	12.0	$T_{fluid,7}$ [C]	12.0
$T_{4(6)}$ [C]	12.2	$T_{1(7)}$ [C]	12.0
$T_{5(6)}$ [C]	19.3	$T_{2(7)}$ [C]	12.1
T_{amb} [C]	22.4	$T_{3(7)}$ [C]	22.3
$R_{fluid,6}$ [K W^{-1}]	2.5	T_{amb} [C]	22.4
$R_{PTFE,6}$ [K W^{-1}]	125.6	$R_{fluid,7}$	0.4
$R_{rad,6}$ [K W^{-1}]	114.1	$R_{ss,7}$	1.5
$R_{con,6}$ [K W^{-1}]	103.9	$R_{ins,7}$ [K W^{-1}]	186.7
$R_{eq,6}$ [K W^{-1}]	182.5	$R_{rad,7}$ [K W^{-1}]	1.5
q_6 [W]	0.06	$R_{con,7}$ [K W^{-1}]	2.7
		$R_{eq,7}$ [K W^{-1}]	189.6
		q_7 [W]	0.05

A summary of all results is shown in Table A-1. A conservative estimate of the total heat transfer rate with the environment is 1.34 W, approximately 1.3% of the total input heater power, though the actual value is probably much lower than this.

Appendix B: COMSOL Details

B.1 COMSOL Parameters, Variables and Functions

Parameters in COMSOL are constant values that are available globally throughout the model. The parameters used in the current work are shown in Figure B-1. The first eight parameters (W_ch, W_fin, H_ch, H_floor, H_cell, L_ch, W_unit and W_hcell) are all used in defining the model geometry discussed in Section 4.1.2. The channel cross-sectional area (A_ch), hydraulic diameter (D_h), aspect ratio (beta) and mass flux (m_flux) are all used in various heat transfer and pressure drop equations discussed later. Inlet temperature (T_in), inlet pressure (P_in) and mass flow rate (m_dot) are all user inputs that correspond to the experiment. The number of channels (N_ch) is also specified, as is the value of gravity (g).

Variables are similar to parameters but need not be constants. Since many of the COMSOL variables use built-in COMSOL functions, these functions (shown in Figure B-2) will be described first. Different function types are denoted by different symbols that are defined in Figure B-3. The

Parameters

Name	Expression	Value	Description
W_ch	45 [um]	4.5000E-5 m	Channel Width
W_fin	35 [um]	3.5000E-5 m	Fin Width
H_ch	200 [um]	2.0000E-4 m	Fin/Channel Height
H_floor	300 [um]	3.0000E-4 m	Floor Thickness
H_cell	H_ch + H_floor	5.0000E-4 m	Wafer Thickness
L_ch	5 [mm]	0.0050000 m	Channel Length
W_unit	W_ch + W_fin	8.0000E-5 m	Unit Cell Width
W_hcell	W_unit/2	4.0000E-5 m	Half Cell Width
A_ch	W_ch * H_ch	9.0000E-9 m^2	Channel Cross Section Area
D_h	4*A_ch/(2*(H_ch+W_ch))	7.3469E-5 m	Hydraulic Diameter
beta	W_ch/H_ch	0.22500	Aspect Ratio
T_in	284.65 [K]	284.65 K	Inlet Fluid Temperature
m_dot	(.0997 / (N_ch*60)) [kg/s]	1.3293E-5 kg/s	Mass Flow Rate for Channel
N_ch	125	125.00	Number of Channels
m_flux	m_dot/A_ch	1477.0 kg/(m^2·s)	Mass Flux for Channel
g	9.81 [m/s^2]	9.8100 m/s^2	Gravitational Constant
P_in	595.1 [kPa]	5.9510E5 Pa	Inlet Pressure

Figure B-1: COMSOL parameters.

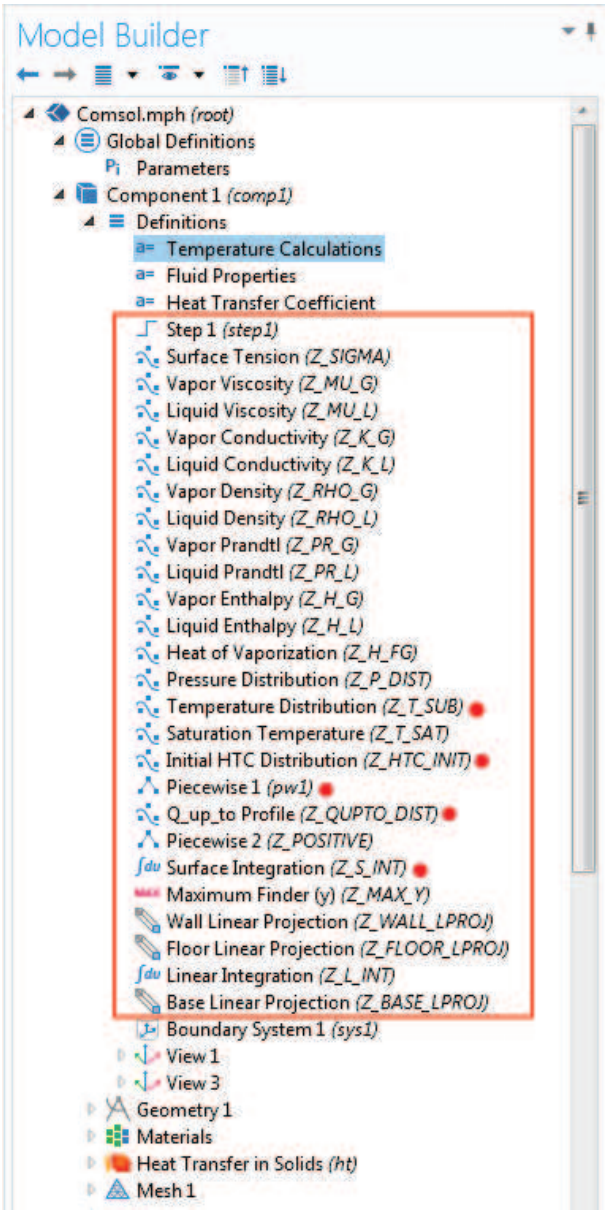

Figure B-2: COMSOL functions. Functions denoted by red dots were only used during troubleshooting.

function label includes a brief description of the function content followed by the function name in parentheses. The first function, step1, is a step function that returns a value of one if the argument is positive and returns a value of zero otherwise. This is used to apply separate correlations in the single- and two-phase regions. The following twelve interpolation functions are

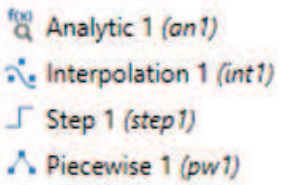

Figure B-3: Function type legend.

used to determine fluid properties for the working fluid (R134a). These interpolation functions import data from files containing the respective fluid properties at a range of temperatures between 0°C and 100°C. These fluid properties were found to vary little across the pressure ranges encountered in this study so, when necessary, an average pressure has been assumed and all pressure dependencies have been ignored. The interpolation function that determines saturation temperature, *Z_T_SAT*, depends purely on pressure.

The various other functions are used to perform integrations, locate peak values and circumvent potential numerical problems. The function *Z_P_DIST* is used to import the pressure distribution calculated in MATLAB. *Z_POSITIVE* is a piecewise continuous function that ensures that COMSOL uses non-negative guesses for physically non-negative terms. Three linear projection functions serve to perform line integrals for the given argument across the specified feature at a certain axial location. The integrated value is then mapped to a separate line—in this case the channel midline. For example, *Z_L_INT* is a linear integration function that is used to integrate different values along the channel midline. Used in conjunction with the linear projections, this allows for the integration of a given argument up to any axial location in question. The remaining functions (denoted in the figure by red dots) are used purely in troubleshooting procedures.

Variables in the current model have been loosely divided into three sections: those involving fluid properties, those involving temperature calculations and those involving heat transfer coefficient calculations. The fluid property variables are shown in Figure B-4. These call

Name	Expression	Unit	Description
C_p	1.395 [kJ/(kg*K)]	J/(kg·K)	Average Specific Heat
sigma	Z_SIGMA(T_fluid)	N/m	Surface Tension at Fluid T...
mu_g	Z_MU_G(T_fluid)	kg/(m·s)	Vapor Viscosity at Fluid Te...
mu_l	Z_MU_L(T_fluid)	kg/(m·s)	Liquid Viscoisty at Fluid T...
k_g	Z_K_G(T_fluid)	W/(m·K)	Vapor Conductivity at Flu...
k_l	Z_K_L(T_fluid)	W/(m·K)	Liquid Conductivity at Fl...
rho_g	Z_RHO_G(T_fluid)	kg/m³	Vapor Density at Fluid Te...
rho_l	Z_RHO_L(T_fluid)	kg/m³	Liquid Density at Fluid Te...
Pr_g	Z_PR_G(T_fluid)		Vapor Prandtl Number at...
Pr_l	Z_PR_L(T_fluid)		Liquid Prandtl Number at...
h_g	Z_H_G(T_fluid)	J/kg	Vapor Enthalpy at Fluid T...
h_l	Z_H_L(T_fluid)	J/kg	Liquid Enthalpy at Fluid T...
h_fg	Z_H_FG(T_fluid)	J/kg	Enthalpy of Vaporization
h_fluid_in	Z_H_L(T_in)	J/kg	Initial Fluid Enthalpy
h_fluid	h_fluid_in + Q_up_to/(m_dot/2)	J/kg	Enthalpy at Location
M	102 [kg/kmol]	kg/mol	Molar Mass
x_q	pw1(step1((h_fluid - h_l)/h_fg)*(h_fluid - h_l)/h_fg)		Vapor Quality at Location
P_fluid	Z_P_DIST(y)	Pa	Fluid Pressure Distribution
P_crit	4059 [kPa]	Pa	Critical Pressure
P_r	P_fluid/P_crit		Reduced Pressure
We_l	m_flux^2*D_h/(rho_l*sigma)		

Figure B-4: Fluid property variables.

the appropriate interpolation function, which assigns the value to the variable name specified. Many of these variables are actually functions of other things such as fluid temperature or axial location.

B.2 Temperature Calculation

The temperature calculation variables are shown in Figure B-5. As described in Subsection 4.3.1, the fluid temperature must be calculated differently in the single- and two-phase regions. To do this, two different fluid temperature profiles are calculated and the correct one is referenced for

Name	Expression	Unit	Description
q_at_y	Z_WALL_LPROJ(ht.ntflux) + Z_FLOOR_LPROJ(ht.ntflux)	W/m	
o_Q_up_to	Z_S_INT(ht.ntflux*(y<=dest(y)))	W	Heat Input up to Location
q_bar_flux	pw1(q_at_y/(H_ch+W_ch/2)/1 [W/m^2])*1 [W/m^2]	W/m²	
q_flux	pw1(ht.ntflux/1[W/m^2])*1[W/m^2]	W/m²	
T_fluid_my...	T_in + Q_up_to/((m_dot/2)*C_p)	K	Temperature of Mythical...
T_sat_a	(320 - 192180*(y/1[m])^1.6) [K]	K	Saturation Temperature P...
T_fluid	T_fluid_myth*step1((T_sat-T_fluid_myth)/1[K]) + T_sat*(1-step1((T_sat-T_fluid_myth)/1[K]))	K	Fluid Temperature
T_sat	Z_T_SAT(P_fluid)	K	
Q_up_to	Z_L_INT(q_at_y*(y<=dest(y)))	W	
Q_up_to_d	Z_QUPTO_DIST(y)	W	
T_bar_base	Z_BASE_LPROJ(T)/W_hcell	K	
T_sub	Z_T_SUB(y)	K	

Figure B-5: Temperature calculation variables. Variables denoted by red dots were only used during troubleshooting.

a particular location. A variable named *T_fluid_myth* calculates the single-phase fluid temperature as if phase changed never occurred. A second variable named *T_sat* simply uses the saturation temperature interpolation function and the fluid pressure—obtained from the imported data—to determine the two-phase temperature. The actual fluid temperature at each axial location is then determined using the on/off step function, *step1*, operating on these two other temperature variables to create the actual fluid temperature profile, *T_fluid*. If the saturation temperature at a given location is higher than that of the mythical fluid, the real fluid must be in the liquid single-phase region and *T_fluid_myth* is the actual temperature. If *T_fluid_myth* is higher than the saturation temperature, the real fluid must be in the two-phase region and *T_sat* is the actual fluid temperature.

The variable *q_at_y* determines the linear heat density at any given axial location by integrating the local heat flux using the wall and floor linear projection functions. This variable is then integrated again, using the channel midline linear integration function, to determine the total amount heat transferred between the channel inlet and any given axial location. The profile is assigned to *Q_up_to*. The variables denoted by red dots were used only for troubleshooting purposes, and the remaining variables determine the local heat flux (*q_flux*), the linear average heat flux (*q_bar_flux*), and the average axial base temperature (*T_bar_base*) for use in other calculations.

An example of the variables used for Kim and Mudawar two-phase heat transfer coefficient calculations is given in Figure B-6. These variables are different for each correlation. The heat transfer coefficient is calculated in this section, and all non-dimensional numbers and other terms necessary for the particular correlation are defined here. The basic method of calculating the heat transfer coefficient is similar to the calculation of fluid temperature. Both single-phase and two-

phase heat transfer coefficient profiles are calculated for the entire channel and the correct profile is applied in each region using *step1*, the on/off step function.

Name	Expression	Unit	Description
htc_sp	Nu_sp_km*k_l/D_h	W/(m²·K)	
htc_tp	28*(q_flux*1[m^2/W])^(2/3)*(m_flux*1[m^2*s/kg])^(-0.26)*x_q^(-0.1)*1[W/(m^2*K)]	W/(m²·K)	
htc_current	htc_sp*step1(T_sat/1[K] - T_fluid_myth/1[K]) + htc_tp*(1-step1(T_sat/1[K] - T_fluid_my...	W/(m²·K)	
htc_init	Z_HTC_INIT(x,y,z)	W/(m²·K)	
htc_applied	htc_current	W/(m²·K)	Applied HTC
Nu_sp_km	((1.54*(L_sp/(Re_sp*Pr_l*D_h))^-.33)^4+Nu_3_km^4)^(1/4)		Single-Phase Kim and Mu...
Re_sp	m_flux*D_h/mu_l		Liquid Reynolds Number
Re_g	m_flux*D_h/mu_g		Vapor Reynolds Number
Co	(sigma/(g*(rho_l-rho_g)*D_h^2))^(1/2)		
Nu_3_km	8.235*(1-1.833*beta+3.767*beta^2-5.814*beta^3+5.361*beta^4-2*beta^5)		Term for SP Kim and Mud...
L_sp	Z_MAX_Y(T_fluid,y)	m	
htc_con	(5.2*(Bo*P_heat/P_wet)^0.08*We_l^-0.54+3.5*((1/X_tt)^0.94)*(rho_g/rho_l)^0.25)*(htc_...	W/(m²·K)	
test_htc	20000 + (1+x_q)*1000 [W/(m^2*K)]	W/(m²·K)	
htc_nuc	(2345*(Bo*P_heat/P_wet)^0.7*P_r^0.38*(1-x_q)^-.51)*(htc_db)	W/(m²·K)	
htc_db	0.023*(k_l/D_h)*Re_sp^0.8*Pr_l^0.4	W/(m²·K)	
Bo	q_flux/(m_flux*h_fg)		
P_heat	2*H_ch + W_ch	m	
P_wet	2*(H_ch+W_ch)	m	
X_tt	Z_POSITIVE(((1-x_q)/x_q)^0.9*(rho_g/rho_l)^0.5*(mu_l/mu_g)^0.1)		

Figure B-6: Variables for Kim and Mudawar heat transfer coefficient calculations

B.3 Heat Transfer Coefficient Calculations

Hand calculations were performed for all heat transfer coefficient correlations to verify correct implementation in COMSOL. Calculations for each two-phase correlation were performed for the location of peak heat flux in each of the corresponding 60°C models. The single-phase correlation was evaluated at an arbitrarily chosen axial location of 0.015 mm downstream of the channel inlet for the 60°C Agostini and Bontemps model. These calculations are shown in Table B-1. Necessary fluid property and parameter inputs were extracted from the COMSOL models.

Table B-1: Hand calculations for heat transfer coefficient correlations.

Parameter	Equation	COMSOL Value	Hand Calculation Value	Units
Bertsch et al.				
Inputs	$D_h=73.4\ \mu m$ $G=1477.0\ kg\ m^{-2}\ s^{-1}$ $k_l=0.0851\ Wm^{-1}K^{-1}$ $k_v=0.01421\ Wm^{-1}K^{-1}$ $L_{ch}=5.0\ mm$ $M=102\ kg\ kmol^{-1}$ $u_l=20.41\times10^{-5}\ kg\ m^{-1}\ s^{-1}$ $u_v=11.77\times10^{-6}\ kg\ m^{-1}\ s^{-1}$ $P_R=0.146$ $Pr_l=3.378$ $Pr_v=0.838$ $q''=4.443\times10^{6}\ W\ m^{-2}$ $R_P=1$* $\rho_l=1221.5\ kg\ m^{-3}$ $\rho_v=28.7\ kg\ m^{-3}$ $\sigma = 8.55\times10^{-3}\ N\ m^{-1}$ $x=0.016$ * *assumed value of one if unknown*			
Co	$\frac{1}{D_h}\sqrt{\frac{\sigma}{g(\rho_l-\rho_v)}}$	11.6	11.6	-
Re_l	$\frac{GD_h}{\mu_l}$	531.7	531.2	-
Re_v	$\frac{GD_h}{\mu_v}$	9218.1	9210.9	-

Table B-1 Continued…

Parameter	Equation	COMSOL Value	Hand Calculation Value	Units
$h_{\text{conv,l}}$	$\left(3.66+\frac{0.0668\frac{D_\text{h}}{L_\text{ch}}\text{Re}_\text{l}\,\text{Pr}_\text{l}}{1+0.04\left(\frac{D_\text{h}}{L_\text{ch}}\text{Re}_\text{l}\,\text{Pr}_\text{l}\right)^{2/3}}\right)\frac{k_\text{l}}{D_\text{h}}$	5746.7	5750.0	kW m^{-2}
$h_{\text{conv,v}}$	$\left(3.66+\frac{0.0668\frac{D_\text{h}}{L_\text{ch}}\text{Re}_\text{v}\,\text{Pr}_\text{v}}{1+0.04\left(\frac{D_\text{h}}{L_\text{ch}}\text{Re}_\text{v}\,\text{Pr}_\text{v}\right)^{2/3}}\right)\frac{k_\text{v}}{D_\text{h}}$	1460.3	1465.2	kW m^{-2}
h_{cb}	$(1-x)h_{\text{conv,l}}+xh_{\text{conv,v}}$	5677.4	5681.4	kW m^{-2}
h_{nb}	$55P_\text{R}^{(0.12-log_{10}(R_\text{P}))}(-log_{10}P_\text{R})^{-0.55}M^{-0.5}q''^{0.67}$	1.355 $\times 10^5$	1.357 $\times 10^5$	kW m^{-2}
h_{tp}	$(1-x)h_{\text{nb}}+[1+80(x^2-x^6)e^{(-0.6\cdot Co)}]h_{\text{cb}}$	1.338 $\times 10^5$	1.336 $\times 10^5$	kW m^{-2}
Kim and Mudawar				
Inputs	D_h=73.4 μm G=1477.0 kg m^{-2} s^{-1} h_fg=1.81×10^5 J kg^{-1} k_l=0.0851 W m^{-1} K^{-1} P_H=435 μm P_F=470 μm P_R=0.145 Pr_l = 3.372 ρ_l =1221.6 kg m^{-2} s^{-1} ρ_v =28.7 kg m^{-2} s^{-1} q'' =1.18×10^7 W m^{-2} σ = 8.55×10^{-3} N m^{-1} u_l = 20.42×10^{-5} kg m^{-1} s^{-1} u_v = 11.77×10^{-6} kg m^{-1} s^{-1} x = 0.024			
Bl	$\frac{q''}{Gh_\text{fg}}$	0.043	0.043	-

Table B-1 Continued…

Parameter	Equation	COMSOL Value	Hand Calculation Value	Units
Re_{sp}	$\frac{G(1-x)D_h}{\mu_l}$	521.4	518.2	-
We_l	$\frac{G^2 D_h}{\rho_l \sigma}$	15.34	15.33	-
X_{tt}	$\left(\frac{\mu_l}{\mu_v}\right)^{0.1}\left(\frac{1-x}{x}\right)^{0.9}\left(\frac{\rho_v}{\rho_l}\right)^{0.5}$	5.74	5.72	-
h_{db}	$\left(0.023\,\mathrm{Re}_{sp}^{4/5}\,\mathrm{Pr}_l^{0.4}\right)\frac{k_l}{D_h}$	6457.0	6437.5	kW m^{-2}
h_{cb}	$\left[5.2\left(BlP_H/P_F\right)^{0.08} We_l^{-0.54} + 3.5\left(\frac{1}{X_{tt}}\right)^{0.94}\left(\frac{\rho_v}{\rho_l}\right)^{0.25}\right]h_{db}$	7615.0	7634.9	kW m^{-2}
h_{nb}	$\left[2345\left(BlP_H/P_F\right)^{0.70} P_R^{0.38}(1-x)^{-0.51}\right]h_{db}$	7.72×10^5	7.62×10^5	kW m^{-2}
h_{tp}	$(h_{nb}^2 + h_{cb}^2)^{1/2}$	7.72×10^5	6.62×10^5	kW m^{-2}
Lazarek and Black				
Inputs	D_h=73.4 μm G=1477.0 kg m^{-2} s^{-1} h_{fg}=1.81×10^5 J kg^{-1} k_l=0.0851 W m^{-1} K^{-1} u_l=20.42×10^{-5} kg m^{-1} s^{-1} q''=1.21×10^7 W m^{-2}			
Bl	$\frac{q''}{Gh_{fg}}$	0.045	0.045	-
Re_l	$\frac{GD_h}{\mu_l}$	531.5	530.9	-

Table B-1 Continued…

Parameter	Equation	COMSOL Value	Hand Calculation Value	Units
h_{tp}	$\left(30\,\mathrm{Re}_l^{0.857}\,Bl^{0.714}\right)\frac{k_l}{D_h}$	8.27×10^5	8.22×10^5	kW m^{-2}
Warrier et al.				
Inputs	D_h=73.4 μm G=1477.0 kg m^{-2} s^{-1} h_{fg}=1.819×10^5 J kg^{-1} k_l=0.085 W m^{-1} K^{-1} Pr_l=3.381 u_l=20.65×10^{-5} kg m^{-1} s^{-1} q''=1.80×10^6 W m^{-2} x=0.135			
Bl	$\frac{q''}{Gh_{fg}}$	0.0067	0.0067	-
Re_l	$\frac{GD_h}{\mu_l}$	528.1	525.0	-
$h_{sp,fd}$	$\left(0.00805\,\mathrm{Re}_l^{0.8}\,\mathrm{Pr}_l^{0.4}\right)\frac{k_l}{D_h}$	2295.5	2276.5	kW m^{-2}
h_{tp}	$\left(1+6.0Bl^{1/16}-5.3\left(1-855Bl\right)x^{0.65}\right)h_{sp,fd}$	2.79×10^4	2.78×10^4	kW m^{-2}
Agostini and Bontemps				
Inputs	D_h=73.4 μm G=1477.0 kg m^{-2} s^{-1} q''=6.03×10^6 W m^{-2} x=0.02			
h_{tp}	$28q''^{2/3}G^{-0.26}x^{-0.1}$	2.06×10^5	2.06×10^5	kW m^{-2}
Single-phase Kim and Mudawar				
Inputs	D_h=73.4 μm G=1477.0 kg m^{-2} s^{-1} H=200.0 μm k_l=.088 W m^{-1} K^{-1} L_{sp}=2.28 mm u_l=20.13×10^{-5} kg m^{-1} s^{-1} Pr_l=3.484 W=45.0 μm			
β	$\frac{W}{H}$	0.225	0.225	-

Table B-1 Continued…

Parameter	Equation	COMSOL Value	Hand Calculation Value	Units
Re_l	$\frac{GD_h}{\mu_l}$	489.9	489.9	-
Nu_3	$8.235\left(1-1.833\beta+3.767\beta^2-5.814\beta^3+5.361\beta^4-2.0\beta^5\right)$	5.967	5.967	-
h_{sp}	$\left\{\left[1.54\left(\frac{L_{sp}}{\mathrm{Re}_l\,\mathrm{Pr}_l\,D_h}\right)^{-0.33}\right]^4+Nu_3{}^4\right\}^{1/4}\left(\frac{k_l}{D_h}\right)$	8390.5	8375.3	kW m^{-2}